First-Principles Modeling of Thermal Stability and Morphology Control of Cathode Materials in Li-ion Batteries

by

Lei Wang

B.S. Materials Science and Engineering, Tsinghua University (2004)

Submitted to the Department of Materials Science and Engineering
in partial fulfillment of the requirements for the degree of

Doctor of Philosophy in Materials Science and Engineering

at the

MASSACHUSETTS INSTITUTE OF TECHNOLOGY

October 2009 [February 2010]

Author .....

Department of Materials Science and Engineering

October 19, 2009

Certified by .....

Gerbrand Ceder

R. P. Simmons Professor of Materials Science

Thesis Supervisor

Accepted by .....

Christine Ortiz

Associate Professor of Materials Science and Engineering

Chairman, Department Committee on Graduate Students

First-principles Modeling of Thermal Stability and Morphology Control of Cathode Materials in Li-ion Batteries

by

Lei Wang

Submitted to the Department of Materials Science and Engineering

on Oct 19, 2009, in partial fulfillment of the requirements for the degree of

Doctor of Philosophy in Materials Science and Engineering

Abstract:

We compute the energy of a large number of oxidation reactions of 3*d* transition metal oxides using the generalized gradient approximation (GGA) to density functional theory and GGA+*U* method. Two substantial contributions to the error in GGA oxidation energies are identified. The first contribution originates from the overbinding of GGA in the O_2 molecule and is only present when the oxidant is O_2. The second error occurs in all oxidation reactions and is related to the correlation error in 3*d* orbitals in GGA. The constant error in the oxidation energy from the O_2 binding error can be corrected by fitting the formation enthalpy of simple non-transition metal oxides. Removal of the O_2 binding error makes it possible to address the correlation effects in 3*d* transition metal oxides with the GGA+*U* method.

Building on the previous success of obtaining accurate oxidation energies from first-principles calculations, we present a new method for predicting the thermodynamics of thermal degradation of charged cathode materials for rechargeable Li batteries and demonstrate it on three cathode materials, Li_xNiO_2, Li_xCoO_2, and $Li_xMn_2O_4$. The calculated decomposition heat for the three systems is in good agreement with experiments. The electrolyte can act as a sink for the oxygen released from the cathode. Although oxygen release from the cathode is generally endothermic, its combustion with the electrolyte leads to a highly exothermic reaction, which is the main source of safety problems with lithium batteries.

This thesis also studies surface properties and morphology control of olivine structure $LiMPO_4$ (M=Fe, Mn). The calculated surface energies and surface redox potentials are very anisotropic. With the calculated surface energies, we provide the thermodynamic equilibrium shape of a $LiMPO_4$ crystal under vacuum. We furthermore establish an *ab initio* approach to study surface adsorption and Li dissolution in aqueous solutions. We demonstrate for $LiFePO_4$ that *ab initio* calculations can be used effectively to investigate the crystal shape dependency on practical solution parameters, such as electric potential *E* and solution *pH*. Our first-principles work is helpful in finding a synthesis condition that

favors the production of platelet shape $LiFePO_4$ with large area of reaction active (010) surface.

Thesis Supervisor: Gerbrand Ceder

Title: R. P. Simmons Professor of Materials Science

Acknowledgements

I would like to thank:

- My thesis advisor, Professor Ceder, for his guidance and constant motivations over the past five years.
- The members of my thesis committee, Professor Marzari and Professor Schuh, for their kind suggestions on my thesis.
- The Ceder group members, friends in Boston and somewhere else, for creating a friendly environment.
- My parents and parents in-law, who have always been supportive on my studies and everything else.
- My wife, Jie, for her support, encouragements, and optimistic attitude towards life.

Table of Contents

Chapter 1

Introductions

In this chapter, we first introduce Li-ion batteries and density functional theory calculations, especially the DFT+U method that we use extensively throughout this thesis. We discuss some unsolved challenges related to the performances of cathode materials in Li-ion batteries, which will be investigated in this thesis using first-principles modeling.

1.1 Li-ion batteries

Since the first commercialization of lithium ion rechargeable battery by Sony [1] in 1989, lithium ion battery research has received extensive attention from both fundamental and practical levels. A state-of-art lithium ion battery consists of a cathode, an anode, and an electrolyte. The voltage of the battery is proportional to the difference in chemical potentials of lithium for the cathode and anode. Typical anode and cathode materials are both intercalation compounds, with the cathode material having a higher voltage with respect to metallic lithium than the anode material. When the battery is discharged, lithium ions leave the anode in ionized form and migrate through the electrolyte to the cathode, and an equal amount of electrons travel via the external electric circuit where the battery performs the work. This results in the lowering of the chemical potential for lithium ions and the reduction of cathode. Upon charging the battery, lithium ions are forced to return to the anode by an externally applied voltage, and the cathode compound is oxidized. The electrolyte, which is typically a salt dissolved in an organic solvent or a polymer, serves as a medium for rapid lithium ion diffusion and blocks the internal

transportation of electron inside the battery cell. Graphite is commonly employed as anode material while different lithium inserted transition metal oxides can serve as cathode. Popular lithiated transition metal oxides possess layered, spinel, or olivine crystal structure.[2-4] In this thesis, we focus on cathode materials that exhibit a variety of interesting thermodynamic and kinetic material properties.

1.2 Density functional theory calculations

1.2.1 Self-interaction error in transition metal oxides

All results in this thesis are calculated using a first-principles method, which requires only nuclear charges and number of electrons as inputs. Currently, all *ab initio* methods use a series of approximations in calculating physical quantities. First-principles calculations employing density functional theory (DFT) have been proved powerful in understanding the electronic, structural, and thermodynamic properties of a vast class of materials.[5-7] The density functional is usually modeled within the local density approximation (LDA) or generalized gradient approximation (GGA). For many systems, LDA or GGA gives remarkably good agreement with experiments, promoting density functional theory calculations as a valuable tool to predict material properties.

A fundamental problem with LDA or GGA is the exchange-correlation energy functional $E_{xc}^{LDA}[n]$ or $E_{xc}^{GGA}[n, \nabla n]$, which is defined either solely as a function of local electron density *n(r)*, or as a function of both the electron density and its gradient corrections $\nabla n(r)$ [8, 9]. Consequently, the variational derivative $\delta E_{xc}^{LDA/GGA}[n]/\delta n(r)$, the exchange-correlation potential, is a continuous function of electron density *n(r)*. This is in contradiction to the exact density functional, whose derivative exhibits a discontinuity at

integral number of electrons.[10] Therefore, any attempts to improve LDA or GGA as an approximation to exact density functional theory should be able to reproduce this discontinuity.

The lack of discontinuity in LDA or GGA is related to the fact that the energy functional is defined in such a way as to treat electron interactions based on a homogeneous electron gas. When strong localization of the electrons occurs, the errors in LDA electron interactions are particularly pronounced. A well known example is the strongly correlated transition metal oxides, in which LDA fails to capture the Coulomb repulsions between electrons localized at the same site.[11, 12] This leads to the false prediction of many insulating transition metal oxides as conductors, as well as the underestimation of magnetization on transition metal ions.[13]

1.2.1 DFT+*U* method

The DFT+*U* method was first developed in the early 1990s to deal with strong electron correlations.[14, 15] Depending on whether local density approximation or generalized gradient approximation is used in practice, the name of LDA+*U* or GGA+*U* is referred in literature. As a leading correction to LDA and GGA, the DFT+*U* method has been proved to be successful in transition metal oxides.[13] The key concept of DFT+*U* is to address the on-site Coulomb interactions in the localized *d* or *f* orbitals with an additional Hubbard-type term. At the GGA+*U* level, the total energy can be summarized in the following form:

$$E_{GGA+U}[\rho, \hat{n}] = E_{GGA}[\rho] + E_{hubbard}[\hat{n}] - E_{dc}[\hat{n}] \equiv E_{GGA}[\rho] + E_{U}[\hat{n}] \qquad (1\text{-}1)$$

where ρ refers to the electron density and $\hat{n}$ is the on-site occupation matrix for d or f orbitals. The Hatree-Fock like term $E_{hubbard}[\hat{n}]$ is derived from the Hubbard model and the double-counting term $E_{dc}[\hat{n}]$ addresses on-site interactions for d or f electrons in LDA. The combination of the two terms is generally referred to the U correction $E_U[\hat{n}]$ to LDA or GGA.

Different approaches of DFT+U exist in the literature depending on the detailed implementation of the double counting term $E_{dc}[\hat{n}]$. Here we mention two common approaches[16] that are relevant to this thesis work. The rotationally invariant form was first proposed by Liechtenstein et al. [17] and was also called the "full localized limit (FLL)",

$$E_{dc}^{FLL}[\hat{n}] = \frac{U-J}{2} Tr(\hat{n})[Tr(\hat{n}) - 1] = \frac{U'}{2} Tr(\hat{n})[Tr(\hat{n}) - 1] \tag{1-2}$$

$$E_{U}^{FLL}[\hat{n}] = \frac{U-J}{2} Tr(\hat{n}(1-\hat{n})) = \frac{U'}{2} Tr(\hat{n}(1-\hat{n})) \tag{1-3}$$

where we have defined $U' = U - J$. The exchange parameter J is of the order of 1 eV for most late transition metal oxides[18]. Dudarev et al. further expressed the above double-counting scheme in a spherically averaged version[19]. The FLL scheme is preferred for strongly correlated materials where electrons are more localized. There is another double counting implementation called the "around mean field (AMF)" scheme [15, 16]. Its simplified spherical average version is given by,

$$E_{dc}^{AMF}[\hat{n}] = \frac{U-J}{2} Tr(\hat{n} \cdot \hat{n}) = \frac{U'}{2} Tr(\hat{n} \cdot \hat{n}) \tag{1-4}$$

$$E_{U}^{AMF}[\hat{n}] = -\frac{U-J}{2} Tr(\hat{n} \cdot \hat{n}) = -\frac{U'}{2} Tr(\hat{n} \cdot \hat{n}) \tag{1-5}$$

The "around mean field" double counting scheme is meant to work for materials with weakly or moderately correlated electrons, such as transition metal or its alloys, e.g. Fe_3Al [21], and FeAl [22]. The implementations of those schemes within a projector augmented wave (PAW) framework were developed by Bengone et al.[20]. In this thesis, we use the FLL GGA+*U* because we deal with transition metal oxides based cathode materials.

1.3 Motivations

In this thesis, we would like to use first-principles calculations to deal with two interesting problems for cathode materials of Li-ion batteries: First, thermal stability of cathode materials; Second, surface properties and equilibrium morphology of olivine structure $LiMPO_4$ (M = Fe and Mn).

The thermal stability problem of cathode materials is an integral part of the safety issues for Li-ion batteries. Before the development of our first-principles model, much of previous experimental works focused on measuring of weight loss and heat generation during the thermal degradation of cathode material.[23] The reaction mechanism is pinpointed later by combining the experimental observations together. However, the thermodynamics of cathode decomposition is always coupled with the reaction kinetics in experimental measurements, leading to a vague understanding of the underlying thermal degradation mechanism. On the contrary, first-principles calculations are able to provide accurate thermodynamic data for reactions among solid phases. In chapter two, we present the first-principles model developed in this thesis to study the thermodynamics of cathode degradations. This modeling work can compliment the vast existing experimental

measurements and observations of decomposition reactions for lithium transition metal oxides.

The second part of the thesis focuses on surface properties and morphology control for olivine structure $LiMPO_4$. Recent success of particle size control has stimulated heated discussions about the performance difference between nano and macron size $LiFePO_4$.[24-30] Using first-principles calculations of surface properties for $LiMPO_4$, we would like to determine whether at the nano size level any fundamental change has been introduced to the thermodynamics and/or kinetics. On the other hand, our morphology study is largely due to the belief that lithium diffusion inside the olivine structure is one-dimensional.[31, 32] We would like to predict the equilibrium particle shape for $LiFePO_4$ under both vacuum and aqueous environment. These *ab initio* results are useful to find some synthesis condition where thin-plate particle shape is thermodynamically favored and the reaction active (010) surface can be exposed to a large extent.

References:

[1] J. O. Besenhard, *Handbook of battery materials* (Wiley-VCH, Weinheim, Germany, 1999).

[2] C. Delmas, C. Fouassier, and P. Hagenmuller, Physica **99B**, 81 (1980).

[3] M. M. Thackeray, P. J. Johnson, L. A. de Picciotto, P. G. Bruce, and J. B. Goodenough, Mater. Res. Bull. **19**, 179 (1984).

[4] A. K. Padhi, K. S. Nanjundaswamy, and J. B. Goodenough, J. Electrochem. Soc. **144**, 1188 (1997).

[5] R. G. Parr and W. Yang, *Density-functional theory of atoms and molecules* (Clarendon, New York, 1989).

[6] P. Hohenberg and W. Kohn, Phys. Rev. **136**, 864 (1964).

[7] W. Kohn and L. J. Sham, Phys. Rev. **140**, A1133 (1965).

[8] J. P. Perdew, K. Burke, and M. Ernzerhof, Phys. Rev. Lett. **77**, 3865 (1996).

[9] J. P. Perdew and Y. Wang, Phys. Rev. B **45**, 13244 (1992).

[10] J. P. Perdew, R. G. Parr, M. Levy, and J. L. Balduz, Phys. Rev. Lett. **49**, 1691 (1982).

[11] R. O. Jones and O. Gunnarsson, Rev. Mod. Phys. **61**, 689 (1989).

[12] W. E. Pickett, Rev. Mod. Phys. **61**, 433 (1989).

[13] V. I. Anisimov, *Strong coulomb correlations in electronic structure calculations: beyond the local density approximation*, Amsterdam, Netherlands, 2000).

[14] V. I. Anisimov and O. Gunnarsson, Phys. Rev. B **43**, 7570 (1991).

[15] V. I. Anisimov, I. V. Solovyev, M. A. Korotin, M. T. Czyzyk, and G. A. Sawatzky, Phys. Rev. B **48**, 16929 (1993).

[16] A. G. Petukhov, I. I. Mazin, L. Chioncel, and A. I. Lichtenstein, Phys. Rev. B **67**, 153106 (2003).

[17] A. I. Liechtenstein, V. I. Anisimov, and J. Zaanen, Phys. Rev. B **52**, R5467 (1995).

[18] V. I. Anisimov, J. Zaanen, and O. K. Andersen, Phys. Rev. B **44**, 943 (1991).

[19] S. L. Dudarev, G. A. Botton, S. Y. Savrasov, C. J. Humphreys, and A. P. Sutton, Phys. Rev. B **57**, 1505 (1998).

[20] O. Bengone, M. Alouani, P. Blöchl, and J. Hugel, Phys. Rev. B **62**, 16392 (2000).

[21] F. Lechermann, M. Fähnle, B. Meyer, and C. Elsässer, Phys. Rev. B **69**, 165116 (2004).

[22] P. Mohn, C. Persson, P. Blaha, K. Schwarz, P. Novák, and H. Eschrig, Phys. Rev. Lett. **87**, 196401 (2001).

[23] J. R. Dahn, E. W. Fuller, M. Obrovac, and U. v. Sacken, Solid State Ionics **69**, 265 (1994).

[24] C. Delacourt, P. Poizot, S. Levasseur, and C. Masquelier, Electrochemical and Solid State Letters **9**, A352 (2006).

[25] B. Kang and G. Ceder, Nature **458**, 190 (2009).

[26] L. Laffont, C. Delacourt, P. Gibot, M. Y. Wu, P. Kooyman, C. Masquelier, and J. M. Tarascon, Chem. Mater. **18**, 5520 (2006).

[27] G. Y. Chen, X. Y. Song, and T. J. Richardson, Electrochemical and Solid State Letters **9**, A295 (2006).

[28] N. Meethong, H. Y. S. Huang, W. C. Carter, and Y. M. Chiang, Electrochemical and Solid State Letters **10**, A134 (2007).
[29] C. Delmas, M. Maccario, L. Croguennec, F. Le Cras, and F. Weill, Nat. Mater. **7**, 665 (2008).
[30] P. Gibot, M. Casas-Cabanas, L. Laffont, S. Levasseur, P. Carlach, S. Hamelet, J. M. Tarascon, and C. Masquelier, Nat. Mater. **7**, 741 (2008).
[31] D. Morgan, A. Van der Ven, and G. Ceder, Electrochemical and Solid State Letters **7**, A30 (2004).
[32] M. S. Islam, D. J. Driscoll, C. A. J. Fisher, and P. R. Slater, Chem. Mater. **17**, 5085 (2005).

Chapter 2

Accurate Oxidation Enthalpies from First-principles Calculations and the Application to Thermal Stability Investigation for Cathode Materials

We begin this chapter with a short description of the thermal stability problem associated with cathode materials in Li-ion batteries. We then propose the research objectives for our first-principles study on this topic. After identifying the major errors in our computational methodology and possible remedies, we present the framework of our *ab initio* model and demonstrate it on several common cathode materials. This chapter ends with a discussion of our investigation results and potential drawbacks of our model and possible future works on this topic.

2.1 Thermal stability problem for cathode materials

2.1.1 Introductions

Dell's large-scale recall of laptop batteries in 2006 raised considerable public concern and criticism of the safety issues for rechargeable Li-ion batteries. As more Li is electrochemically removed from the cathode in a drive for higher energy density, the electrode material becomes highly oxidized and may degrade through exothermic or endothermic phase transitions. The decomposition of the cathode material at a high state of charge can result in the release of heat and oxygen gas, which can lead to runaway reactions. In order to improve the thermal stability of rechargeable lithium batteries, it is

important to understand the thermal degradation mechanisms of cathode materials at various charging states.

From a materials science point of view, for a phase transformation of an electrode material to occur, a thermodynamic driving force towards another phase (or combination of phases) needs to exist. If the mobility of the ions is high enough to allow their migration at the temperature where the free energy change for the conversion is negative, we consider the reaction to be thermodynamically controlled. This is shown schematically on the right hand side of Figure 2-1. Upon heating, atomic mobility is high enough near T_c^K, but the transformation does not occur until T_c^{TD}, the thermodynamic transition temperature, is reached. For reactions with low thermodynamic reaction temperature, the situation in the left hand side of Figure 2-1 is more likely: In this case, the thermodynamic driving force for phase conversion already exists at low temperature, but the conversion only occurs when the ions achieve a high enough mobility. We refer to these as kinetically controlled transitions. Modeling the kinetics of phase transformations from first-principles is an unsolved problem in materials science. In the context of Li-electrode materials useful qualitative information can be obtained by understanding how the mobility of a transition metal cation in a close-packed oxygen framework is determined by its energy difference in the octahedral and tetrahedral site, which is largely controlled by ligand field effects.[1, 2] Ligand field theory predicts for example that Co^{3+} and Mn^{4+} are unlikely to be mobile due to their strong octahedral site preference, while Mn^{3+} and Mn^{2+} are expected to be mobile already at room temperature.[1] The transformation of a layered $Li_{0.5}MO_2$ compound to the spinel structure is an example of a kinetically controlled transformation. At partial state of delithiation all layered Li_xMO_2

(with $x < 1$) compounds with the R-3m structure (where M is 3*d* transition metal) have a thermodynamic driving force for the conversion to spinel, even at 0 K, with a negative (exothermic) transformation enthalpy,[3] but the temperature at which it occurs is determined by the mobility of the transition metal cation and the amount of vacancies created by delithiation.[1, 2] Ligand field energy differences between the octahedral and tetrahedral site explain very well, for example, why out of the three layered $Li_{0.5}MO_2$ (M = Mn, Co, Ni) compounds, $Li_{0.5}MnO_2$ is the least stable and $Li_{0.5}CoO_2$ the most stable.

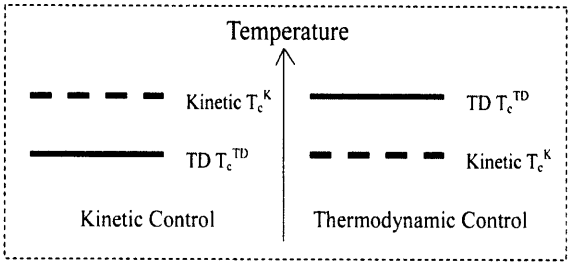

Figure 2-1 Schematic illustration of kinetically and thermodynamically controlled phase transitions. T_c^K and T_c^{TD} are the kinetic and thermodynamic critical transition temperatures, respectively.

Another class of transitions which is important for understanding the thermal stability of electrodes is those that reduce the average valence of the electrode by losing oxygen either through outgassing or oxidation of the electrolyte. Reactions that release O_2 gas have large positive entropy of reaction and can always become favorable at high enough temperature, even if they have positive reaction enthalpy. In this thesis we mainly focus on these reduction reactions, though we will make occasional comments about the important kinetically controlled reactions.

2.1.2 Proposed first-principles studies

First-principles computations have been shown to be effective in predicting a wide variety of properties for cathode materials in Li-ion batteries, including the intercalation voltage,[4] Li-vacancy ordering,[5] Li diffusion,[6, 7] complex transition metal ordering,[8] and recently even electronic transport.[9] However, little or no computational studies on understanding the stability of cathode materials at the high state of charge had been reported by 2006. This problem is in part due to the difficulty of correctly predicting the energy of reduction reactions with Density Functional Theory (DFT) when the Local Density Approximation (LDA) or Generalized Gradient Approximation (GGA) is used for the exchange-correlation correction.[10] This problem is particularly crucial when studying the thermal stability of cathodes as their decomposition is almost always driven by a tendency to reduce the highly charged electrode. It was recently shown that the self-interaction present in LDA and GGA, which is responsible for the underestimation of the redox potential,[11] also creates significant errors in the enthalpy of standard oxidation/reduction reaction.[10] The availability of practical LDA+U schemes, in which much of the self-interaction in transition metals due to correlation effects of the localized d or f electrons is removed,[12, 13] opens up the possibility of quantitative investigations of cathode instabilities at highly charged states.

We intend to develop a new first-principle approach to predict the thermodynamics of thermal degradation reactions for charged cathode materials. Our objectives include understanding the phase evolutions during the thermally induced phase transformations, obtaining accurate reaction enthalpies and approximate critical temperatures for

important decomposition reactions, and eventually establishing an *ab initio* framework to investigate the thermal stability problem for other promising cathode materials. The model will be benchmarked to three common cathode materials, layered Li_xNiO_2, Li_xCoO_2, and spinel $Li_xMn_2O_4$, whose thermal stabilities have been well studied in experiments. Dealing with cathode materials of relatively simple chemistries, we can build a generic framework rather than address material specific behaviors.

2.1.3 Material crystal structures

A) Layered lithium transition metal oxides Li_xMO_2

The interesting layered cathode materials with a chemical formula of $LiMO_2$ often possess a α-$NaFeO_2$ type structure (see Figure 2-2) with a space group of R-*3m*. This is a distorted rock-salt superstructure with a FCC close-packed oxygen framework. The Li and transition metal cations sit at the octahedral interstitial sites of the oxygen sublattice and form an alternating cation planes along the [111] direction. The whole (111) oxygen planes may relax in the [111] direction giving rise to different slab spaces that affect lithium mobility substantially.[14]

B) Spinel lithium transition metal oxides $Li_xM_2O_4$

The spinel structure cathode material has a general chemical formula of $Li_xM_2O_4$, and is so named because at $x = 1$ it has the same crystal structure (with a space group of F*d3m*) as the spinel mineral $MgAl_2O_4$ (see Figure 2-3). The spinel crystal structure possesses the same FCC close-packed oxygen framework as the α-$NaFeO_2$ type structure. The difference lies in the arrangement of cations within the oxygen lattice framework. At $x =$

1, lithium ions occupy 1/8 of the tetrahedral interstitials and transition metal ions occupy 1/2 of the octahedral sites. Upon the further lithiation until $x = 2$, the energetically favored structure has lithium occupying the remaining 1/2 of the octahedral sites left by the transition metal ions.[15]

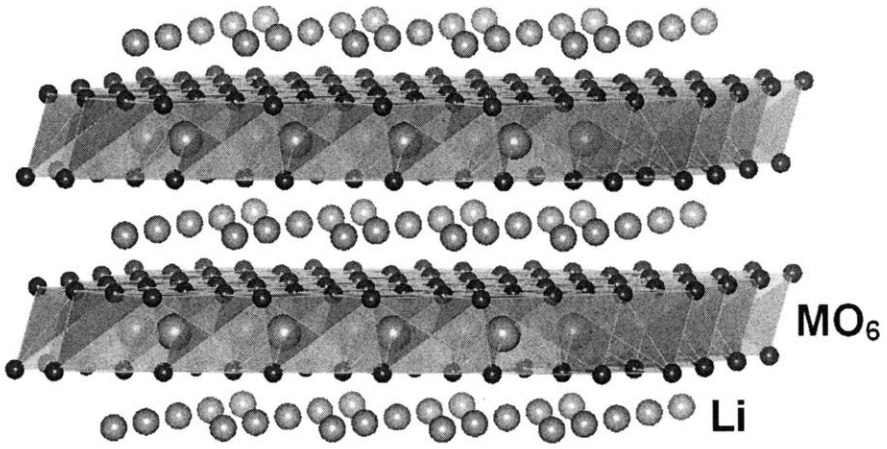

Figure 2-2 Crystal structure of layered cathode material $LiMO_2$.

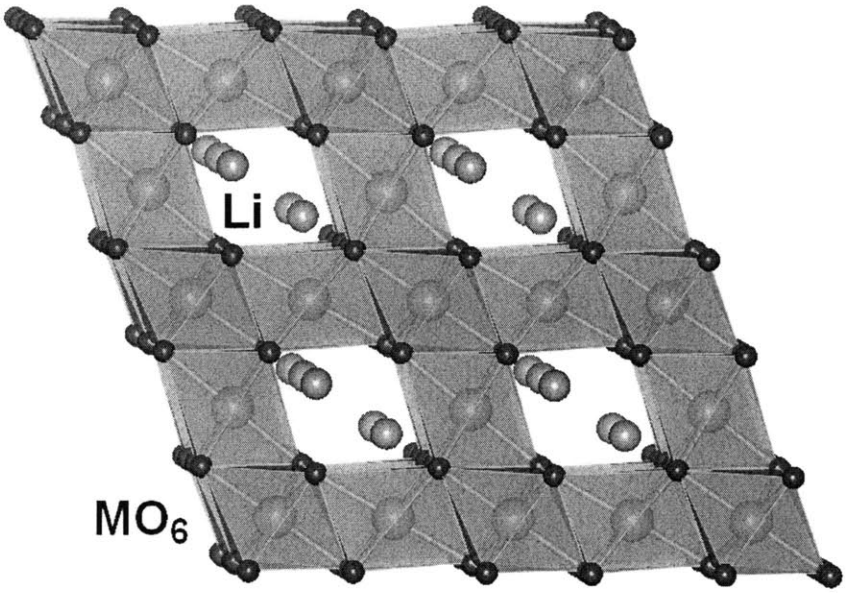

Figure 2-3 Crystal structure of spinel cathode material LiM_2O_4.

2.2 Previous experimental studies

Before the establishment of our first-principles model in 2006, thermal stability problem for several common cathode materials had been extensively studied in experiments. A thorough analysis of those experimental observations will help us understand the problems and anticipate the potential calculation errors in our *ab initio* approach. In this section, we review previous experimental studies of thermal stability for layered Li_xNiO_2, Li_xCoO_2, and spinel $Li_xMn_2O_4$.

2.2.1 Li_xNiO_2

Substantial delithiation of $LiNiO_2$ is known to lead to very unstable compounds that decompose at lower temperature than is the case for delithiated Li_xCoO_2 and $Li_xMn_2O_4$.[16] Thomas et al. suggested that $Li_{0.5}NiO_2$ undergoes a first-order transformation above 420 K to the cubic spinel phase $LiNi_2O_4$ which is stable up to 570 K.[17] Lee et al. have also investigated the composition and temperature dependence of the thermal behavior of Li_xNiO_2: They find that for $x > 0.5$, Li_xNiO_2 decomposes into layered $LiNiO_2$ and spinel $LiNi_2O_4$, while for $x < 0.5$, Li_xNiO_2 converts to spinel accompanied by the release of oxygen.[18] Further increase in temperature leads to a formation of the rock-salt phase in which Li and Ni ions are disordered, with oxygen release at all compositions. Figure 2-4 illustrates the possible reaction scheme and the corresponding structure changes during the transformation from the layered to the rock-salt structure. Guilmard and coworkers have reported that the transformation from layered to spinel involves the migration of Ni cations from the Ni layer into the Li layer, and a displacement of Li from the octahedral

to the tetrahedral sites.[19] Such spinel phases obtained through cation migrations are not perfectly ordered and intermediate pseudospinel structures always appear.[19] Additionally, it has been reported that further decomposition into the rock-salt structure is an *exothermic* reaction that involves the random redistribution of Li and Ni cations across the cation layers and the evolution of oxygen.[20] Lee et al. observed that for $x \geq 0.5$, the reaction heat when the layered structure transforms to spinel decreases linearly with increasing x in Li_xNiO_2. However, for $x < 0.5$ the reaction heat increases as x approaches 0.5.[18] They argued that the change in heat flow near $x = 0.5$ is due to the oxygen release when $x < 0.5$, and interpreted the thermal behavior of Li_xNiO_2 as an overlap of the *exothermic* reaction to form a spinel and the *endothermic* oxygen evolution reaction.

2.2.2 Li_xCoO_2

Partially delithiated $LiCoO_2$ in the layered (R-*3m*) structure is known to be metastable and the material loses oxygen at temperatures above 470 K.[16, 21, 22] Dahn et al. suggested that delithiated materials decompose to stoichiometric $LiCoO_2$ and spinel Co_3O_4 according to the following reactions:[16]

$$Li_xCoO_2(layered) \rightarrow xLiCoO_2(layered) + \frac{(1-x)}{3}Co_3O_4(spinel) + \frac{(1-x)}{3}O_2 \qquad (2\text{-}1)$$

Differential scanning calorimetry (DSC) measurements of the chemically dilithiated Li_xCoO_2 without the presence of electrolyte indicates that reaction (2-1) is an exothermic reaction, and the material is less reactive as x increases.[21, 22]

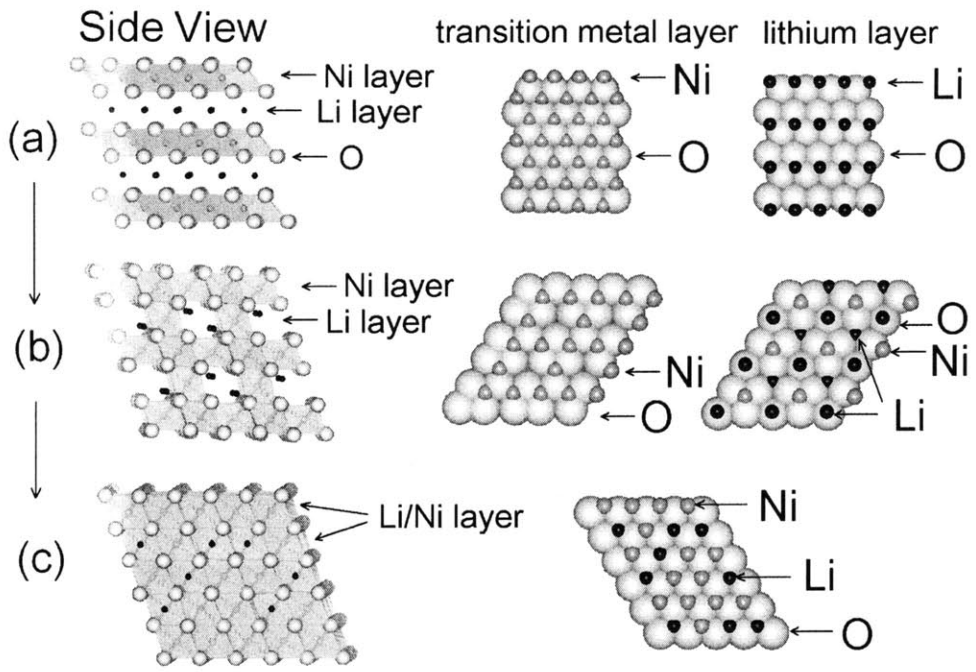

Figure 2-4 Possible reaction scheme and structure changes during the transition of (a) layered structure (R-*3m*) Li_xNiO_2 to (b) spinel structure (F*d3m*) $LiNi_2O_4$ and further to (c) disordered rock-salt structure (F*m3m*) with a composition of $Li_{0.33}Ni_{0.67}O$. In (c), the metal layers are identical in composition.

2.2.3 $Li_xMn_2O_4$

Lithium manganese oxides that have been studied as possible positive electrode materials are $LiMnO_2$ with the monoclinicly distorted α-$NaFeO_2$ type layered structure (C*2/m*),[23-27] $LiMnO_2$ with the orthorhombic structure (P*mnm*),[28, 29] and spinel (F*d-3m* or $I4_1/amd$) $LiMn_2O_4$.[28-30] Mishra et al. studied the relative stability of Li_xMnO_2 in different crystal structures at $x = 0$, 0.5, and 1.[31, 32] At the composition of MnO_2, the layered structure is more stable compared to the spinel (λ-MnO_2) and orthorhombic form. These are all structures with ABC oxygen stacking. Pyrolusite (β-MnO_2) with AB oxygen

stacking is generally regarded as the most stable structure at this composition.[33] Previous experiments and theoretical work have shown that the orthorhombic $LiMnO_2$ structure with antiferromagnetic spin arrangement to be lower in energy than the fully lithiated spinel $Li_2Mn_2O_4$ or layered structure.[31, 34, 35] The layered and orthorhombic structures are known to undergo rapid transformations to the spinel structure upon delithiation.[27, 36-38] The rapid nature of this transformation was previously attributed to the ease by which Mn^{3+} disproportionates and moves through the tetrahedral sites.[2] Spinel $Li_xMn_2O_4$ is not observed to be susceptible to any major structural transformation upon electrochemical cycling over the range $0 \leq x \leq 2$, though the practical cycling of Li is limited to $0 \leq x \leq 1$ due to the asymmetric lattice expansion of $Li_{1+x}Mn_2O_4$ induced by Jahn-Teller effect.[28] Schilling et al. reported that the fully delithiated $Li_xMn_2O_4$ ($x = 0$) undergoes an exothermic transition to β-MnO_2 at 540 K followed by an endothermic decomposition into α-Mn_2O_3 at 820 K.[39] For the cubic spinel $LiMn_2O_4$, experimental studies have reported various phase transitions accompanied by the loss of oxygen at high temperature:[39-43] Tsuji et al. reported that the material has weight loss in air around 960 K with two more weight loss peaks at 1210 K and 1350 K. Monoclinic Li_2MnO_3 appears as the first decomposition product, followed by orthorhombic $LiMnO_2$ and tetragonal spinel Mn_3O_4.[40]

From the above literature review of experimental thermal stability studies, one can make two generic observations for all three types of cathode materials: First, charged cathode materials generate oxygen gas as temperature increases; Second, highly oxidized cathode materials at charged states degrade into mixture of compounds with lower

valence state during the oxygen loss process. This indicates that the underlying chemical reactions behind the thermal stability problem are the temperature dependent oxidation/reduction reactions with oxygen gas involved. In order to build an accurate first-principle model to study the thermal stability problem and achieve the goals we proposed earlier this chapter, the accurate prediction of oxidation/reduction reaction energies is crucial. However, as we see in the next section, accurate oxidation enthalpies for transition metal oxides are rather challenging in DFT, especially when oxygen molecules participate in the oxidation reaction.

2.3 Errors in first-principles predictions of oxidation energies for transition metal oxides and possible corrections

Before we dive into the problem of predicting oxidation energies for cathode materials, which are typically ternary lithium transition metal oxides, let us first consider binary transition metal oxides in this section and evaluate the DFT accuracy in calculating oxidation energies for them.

Although LDA and GGA are rather crude approximations to the many-body electron problems in DFT, their successes in accurately predicting many materials properties are in large part due to the cancellation of errors in energy differences. In this section, we show that GGA has systematic and non-canceling errors in the energy of oxidation reactions for 3*d* transition metal oxides, and we identify two causes for them.

It is well known that the binding energy of the O_2 molecule exhibits large errors when LDA or GGA is used.[44-46] Much of this overbinding is not cancelled when forming an oxide where O^{2-} binds largely electrostatically. The overbinding of the O_2 molecule by

both LDA and GGA makes calculated oxidation energies less negative than experimental values when O_2 is the oxidant. While the O_2 binding error represents essentially a constant shift in oxidation energies and, if present alone, would be easy to correct for, a more subtle error arises due to the self-interaction errors present in LDA/GGA. This error, related to the fact that reduced and oxidized states in transition metal oxides have different number of localized *d*-electrons, is present even when the energy of the oxidant is exactly known. The magnitude of the self-interaction in LDA/GGA depends very much on the nature of the hybridization of electron orbitals in the oxide. When an electron is transferred between significantly different environments, as is the case for many redox processes, little error cancellation is to be expected. This is well observed in GGA (or LDA) predictions for electrochemical oxidation reactions, in which the energy of the oxidation source (the electron acceptor) is not suspect as in the case for O_2. For example, the energy to simultaneously extract a Li^+ ion and an electron from a lithium transition metal oxide and add both to Li metal can be in error by as much as 1.5 eV (out of 4 eV).[11] The Li^+ binding in the oxide is purely electrostatic and should be well represented by LDA or GGA. The culprit in these large electrochemical energy errors is the 3*d*-metal oxidation state change. When an electron is removed from the localized 3*d*-orbital of a transition metal ion in an oxide, and transferred to the metallic 2*s*-orbital of Li^+ ion in the metal (the electron accepting process), it experiences considerably less self-interaction in the metallic state of Li, leading to a consistent underestimation of the energy required for this redox process. While this error has been identified and corrected in calculations on Li-insertion oxides,[11, 47] we expect that similar effects will play a role in the reactions of transition metals to their oxides. We investigate a large number of oxidation reactions of

3*d*-metals and attempt to separate the error related to the O_2 molecule from that caused by the self-interaction. We also suggest that the latter error can be remedied with GGA+*U*.

2.3.1 Benchmark compounds

We first focus solely on oxidation reactions with O_2 for binary oxides, as accurate experimental data is available for them. We consider the general oxidation reaction,

$$MO_x + \frac{y-x}{2} O_2 \rightarrow MO_y \tag{2-2}$$

and calculate the reaction energy (on a per O_2 molecule basis) as:

$$\Delta H_o = \frac{E(MO_y) - E(MO_x) - \frac{y-x}{2} E(O_2)}{\frac{y-x}{2}} \tag{2-3}$$

Note that we neglect the $P\Delta V$ term when comparing calculated reaction energies with measured enthalpies. Strictly speaking if we approximate the volume change in reaction (2-2) with the volume of O_2 gas, this $P\Delta V$ term is not small at room temperature (about 25.8 meV per formula unit of O_2 molecule). However, it only represents a constant shift of the calculated oxidation energy and we will see later that this term can be properly addressed in our error correction procedure. Experimental room temperature formation enthalpy and heat capacity of compounds are obtained from the *JANAF* thermochemical tables [48] and from the monograph by Kubaschewski [49].

The oxides of V, Cr, Mn, Fe, Co, Ni and Cu are studied. We did not investigate Ti oxides as they are metallic in their partially reduced states, where the "full localized limit" version of GGA+*U* used here might not be an appropriate approach. The crystal structures of these oxides and their magnetic configurations are summarized in Table 2-1.

Since β-MnO_2 has a nontrivial helimagnetic structure in ground state, we assume a ferromagnetic electronic structure for practical reasons.

2.3.2 Error related to oxygen molecule and possible correction

Figure 2-5 shows the energy to form various oxides from their metals as calculated using GGA. The calculated reaction energy (per mole O_2) is plotted versus the experimental enthalpy. There is a clear tendency for GGA to underestimate the oxidation energy. This trend can be attributed to the overbinding of GGA in the O_2 molecule. We calculate a binding energy of O_2 of -6.02 eV, which compares well with previous GGA calculations of -5.99 eV.[46] The experimental binding energy is considerably lower and about -5.23 eV.[67] To separate the O_2 binding error from more complex correlation effects in the 3*d* localized orbitals of transition metal oxides, the oxidation energies of several non-transition metal oxides is plotted as an insert in Figure 2-5. The latter indicates a rather constant shift between calculated and experimental values. The minor deviation of SiO_2 from the constant shift can be attributed to the high Si-O bond covalency in that oxide. The constant shift, estimated as -1.36 eV per O_2 from Figure 2-5, is larger than the binding energy error of O_2 in GGA. We believe that the additional error might be GGA error associated with adding electrons to the oxygen *p*-orbital when O^{2-} is formed from O_2.

Table 2-1 Crystal structures and magnetic configurations of transition metal oxides. Except for β-MnO_2 the experimental structures and magnetic configurations were used in the calculations.

TMO	Crystal structure	Magnetic structure	T_N /K or T_C /K
VO	Fm-3m [50]	AFM	125 [51]
MnO	Fm-3m [50]	AFM	122 [52]
FeO	Fm-3m [50]	AFM	175 [52]
CoO	Fm-3m [50]	AFM	289 [52]
NiO	Fm-3m [50]	AFM	523 [52]
CuO	C2/c [53]	AFM	225 [54]
VO_2	$P2_1/c$ [50]	NM	340K [55]
β-MnO_2	$P4_2/mnm$ [50]	AFM	92 [56]
NiO_2	R-3m or C2/m [57]		
V_2O_3	R-3c [50]	AFM	150 [51]
Cr_2O_3	R-3 [50]	AFM	310 [58]
α-Mn_2O_3	Pbca [59]	AFM	90 [59]
α-Fe_2O_3	R-3c [50]	AFM	953 [50]
Mn_3O_4	$I4_1/amd$ [60]	FM	42 [61]
Fe_3O_4	Fd-3m [12]	FM*	860[12]
Co_3O_4	Fd-3m [62]	AFM	33 [63]
Cu_2O	Pn-3m [64]	DM	
V_2O_5	Pmmn [65]	DM	
CrO_3	C2cm [66]	DM	

[a]: anti-ferromagnetic; [b]: non-magnetic; [c]: ferromagnetic; [d]: ferrimagnetic; [e]: diamagnetic.

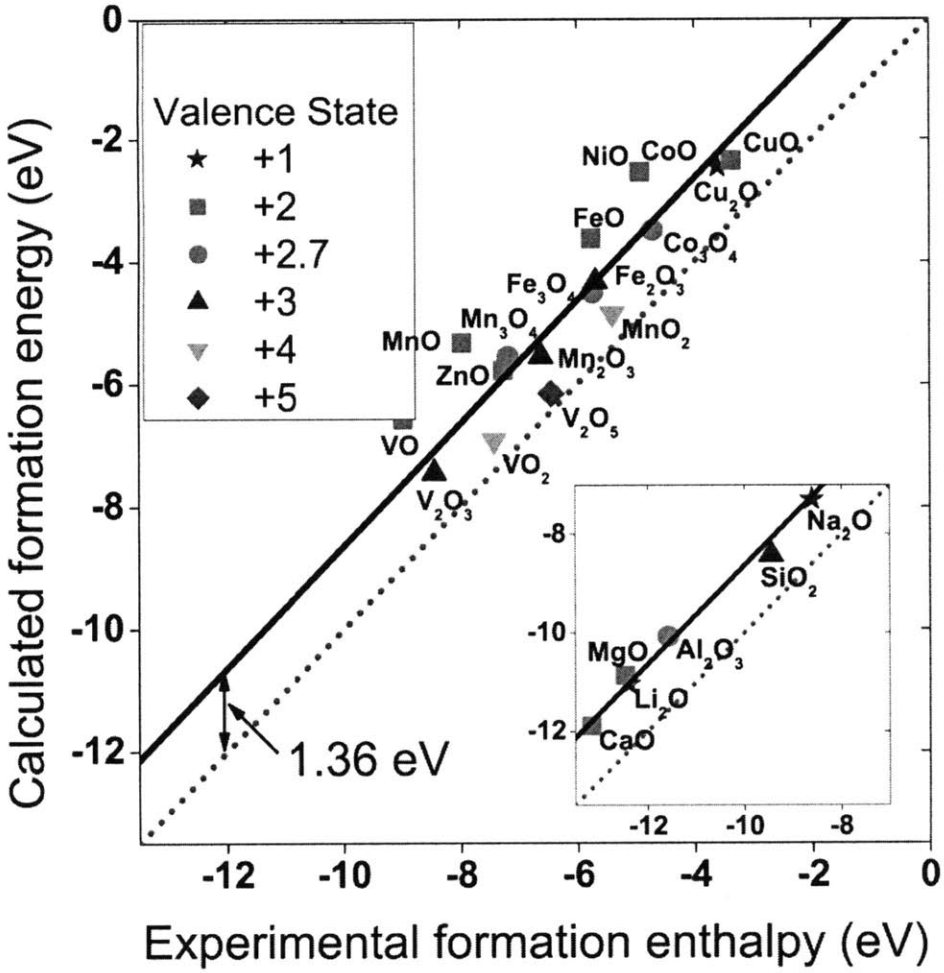

Figure 2-5. Formation energy of oxides (per O_2 in the reaction) in the GGA approximation as a function of the experimental enthalpy.[48, 49] The data symbol indicates the valence of the metal ion. The insert shows non-transition metal oxides. The solid line is the best fit for the non-transition metal data and a -1.36 eV energy correction for O_2 molecule is obtained from this fit.

Now we can comment on the appropriateness of neglecting $P\Delta V$ term in equation (2-2). When we compare our calculated formation energies and experimental formation enthalpies in Figure 2-5, we do neglect the $P\Delta V$ term in the DFT calculated values. However, later we shift the total energy oxygen molecule by 1.36 eV per O_2 and fit the

calculated oxidation energies for non-transition metal oxides to the experimental enthalpies, which actually includes the $P\Delta V$ term as long as the experimental enthalpies are tabulated at the same reference states. When we eventually apply the total energy correction to O_2 molecule in equation (2-2), we assure ourselves that the energy correction has already included the $P\Delta V$ effect. The only pitfall is that strictly speaking, this implicit $P\Delta V$ correction is a value averaged over the pressure effects for the six non-transition metal oxides used in Figure 2-5.

One should also be reminded that the correction of -1.36 eV per O_2 is specific to the computational details in our density functional theory calculations. The oxygen pseudopotential used here has a kinetic energy cutoff of 400 eV. If we perform the same calculations but use an oxygen pseudopotential that has a kinetic energy cutoff of 283 eV, we obtain a correction of -0.84 eV per O_2 formula unit instead.

2.3.3 Error related to localized *d*-electrons and improvements using GGA+*U*

By using the correction derived above for O_2 molecule, we can identify other sources of error in the oxidation energy obtained with GGA. Substantial deviations between calculated and experimental values still exist for the 3*d* transition metal oxides. We believe that the remaining error is due to inaccuracies of GGA in the correlation energy of the 3*d*-states in the transition metal oxides. Correlation effects are substantial in the localized orbitals formed by the metal 3*d*-orbital and oxygen 2*p*-ligands.

Correlation effects in localized orbitals can be treated with the GGA+*U* approach.[12, 68-70] In GGA+*U*, local atomic-like 3*d*-states are projected out and treated with a Hubbard model. While this treats correlation between the 3*d*-states and removes the self-

interaction, it suffers somewhat from the arbitrary nature of the projection orbitals, which are atomic-like, rather than the true one-electron orbitals. This makes GGA+U less applicable to metals where the d-orbitals are not atomic-like anymore. Because of this problem with metallic states, we investigate the accuracy of GGA+U on reactions that oxidize a low-valent oxide to a higher valent one, e.g. reaction (2-2). Since these reactions involve a transfer of electrons from the $3d$-states of the metal to the oxygen $2p$-states, these reactions should still show the energy error that GGA makes in the $3d$ transition metal orbitals.

Figure 2-6 shows how the calculated oxidation energies for several transition metal oxides change with the value of U in the GGA+U method. For a transition metal with n accessible oxidation states, (n-1) independent oxidation reactions are shown. Short horizontal lines indicate the experimental values of the oxidation enthalpy at room temperature. The corrected value for the O_2 molecule is taken into account to obtain these results.

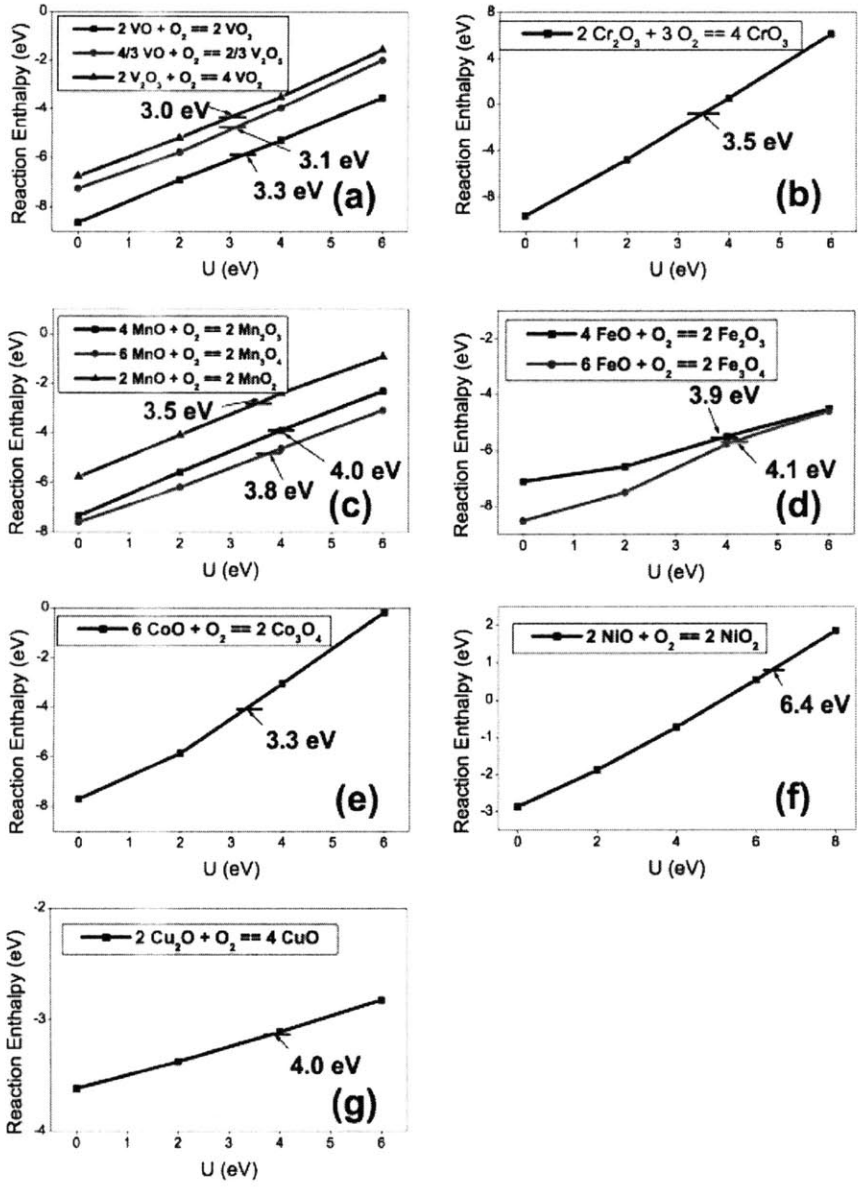

Figure 2-6 Oxidation energies of transition metal oxides as a function of *U*: (a) Vanadium oxides; (b) Chromium oxides; (c) Manganese oxides; (d) Iron oxides; (e) Cobalt oxides; (f) Nickel oxides; (g) Copper oxides. Short horizontal lines indicate experimental oxidation enthalpy values at room temperature.

Table 2-2. Magnetic moments M (in μ_B per TM atom), band gaps E_g (in eV) and U values (in eV) used for transition metal oxides.

TMO	M			E_g			U^*
	GGA	GGA+U	Exp.	GGA	GGA+U	Exp.	
VO	2.12	2.68		0.6	2.4		3.1
MnO	4.39	4.65	4.58-4.79 [68]	1.5	3.2	3.6-3.8 [71]	4.0
FeO	3.43	3.69	3.32 [68]	0	2.2	2.4 [71]	4.0
CoO	2.37	2.65	3.35-3.8 [68]	0	2	2.4 [71]	3.3
NiO	1.32	1.72	1.64-1.90 [68]	0.6	3.4	4 [71]	6.4
CuO	0	0.53	0.68 [54]	0	0.5	1.4 [71]	4.0
VO_2	0	1.09		0.1	0.8	0.7 [71]	
β-MnO_2	2.74	3.24	1.84-2.35 [56]	0	0		
V_2O_3	1.38	1.85	1.2 [72]	0	1.3	0.2 [71]	
Cr_2O_3	2.63	2.9	3.8 [73]	1	2.8	3.4 [71]	3.5
α-Mn_2O_3	3.56	3.92	3.4-3.9 [59]	0	0.5		
α-Fe_2O_3	3.58	4.14	4.9 [74]	0.5	1.8	2.0-2.7 [71],2 [74]	
Mn_3O_4	4.48 [a]	4.70 [a]		0.2	0.6		
	3.82 [b]	4.01 [b]					
Fe_3O_4	3.54 [a]	4.06 [a]	4 [51]	0	1.7	0.07 [75]	
	3.60 [b]	3.64 [b]					
	3.59 [b]	4.17 [b]					
Co_3O_4	2.39 [a]	2.67 [a]	3.02 [76]	0.7	1.6	1.6 [77]	
	0.11 [b]	0.07 [b]					
Cu_2O	0	0		0.4	0.6	2.4 [71]	
V_2O_5	0	0		1.6	2.1	2.0 [71]	
CrO_3	0	0		1.7	1.8		

[a]: A sites; [b]: B sites in spinel structure AB_2O_4

*: The same U value for each transition metal oxides system

For all the oxidation reactions we investigated, unmodified GGA (at $U = 0$) overestimates the oxidation energies, in some cases by several electron volts. Turning on U stabilizes the reduction products (which have more $3d$-electrons) and reduces the oxidation energy. This trend is obtained consistently in all six chemistries and with all reactions studied. In the three systems (V, Mn and Fe), for which data on multiple oxidation reactions are available, it is encouraging that the U values, which bring each calculated oxidation energy in agreement with experiments, lie within a narrow range. To investigate whether these U values also improve the other physical properties, we show in Table 2-2 the band gaps and magnetic moments, calculated in the GGA+U with U values derived from Figure 2-6. GGA results and available experimental values are also provided. It is encouraging that for many systems, the U value that corrects the oxidation energies also improves the band gaps and magnetic moments. A few notable exceptions are present. The electronic structure of Cu oxides is challenging and it is not surprising that even GGA+U does not obtain good band gaps for CuO and Cu_2O. The large discrepancy in Fe_3O_4 is possibly related to the off-stoichiometry and charge disorder between the A and B sites that are common in this material.

2.3.4 Conclusions for obtaining accurate oxidation energies in DFT

To shortly summarize our investigations presented in this section, we have identified two substantial contributions to the error in GGA oxidation energies. The first contribution originates from the overbinding of GGA in the O_2 molecule and the electron addition to oxygen when O^{2-} is formed. This error only occurs when the oxidant is O_2. The second error occurs in all oxidation reactions and is related to the correlation error in

$3d$ orbitals in GGA. Strong self-interaction in GGA systematically penalizes a reduced state (with more d-electrons) over an oxidized state, resulting in an overestimation of oxidation energies. The constant error in the oxidation energy from the O_2 binding error can be corrected by fitting the formation enthalpy of simple non-transition metal oxides. Removal of the O_2 binding error makes it possible to address the correlation effects in $3d$ transition metal oxides with the GGA+U method. Calculated oxidation energies agree well with experimental data for reasonable and consistent values of U.

2.4 Application to the investigation of thermal stability

After identifying the major errors in our computational tool and suggesting possible corrections, we are now ready to apply the investigations above and build a first-principles model to study the thermal stability problem for cathode materials.

2.4.1 Computational methodology

All total energies in the thermal stability work are calculated using GGA. Self-interactions and correlation effects due to localized d electrons have been addressed with the GGA+U method in its rotational invariant form.[78] The projected augmented wave (PAW) [79] method is used, as implemented in the Vienna Ab initio Simulation Package (VASP).[80] An energy cutoff of 500 eV and appropriate k-point meshes are chosen to ensure that the total energies are converged within 3 meV per formula unit.

Many of the decomposition reactions cause a change in the average oxidation states of the transition metal ions and are accompanied by the release of O_2 gas. In previous section we have shown that in such cases two substantial errors are present in GGA.[10]

The first error originates from the overestimation of the binding energies of the O_2 molecule and the electron addition to oxygen when O^{2-} is formed. The magnitude of this error was estimated to be -1.36 eV per O_2 molecule.[10] To achieve reasonable and quantitative accuracy, we therefore increase all calculated oxidation energies by -1.36 eV. The second error in GGA is related to the correlation error in transition metals due to the localized 3*d* orbitals in GGA and can be alleviated through the use of the GGA+*U* method.[12] This approach treats the localized *d* orbitals with an explicit Hubbard term, and cancels the self-interactions. The GGA+*U* treatment was shown to be crucial to obtain accurate oxidation energies and Li-insertion voltages.[11] *U* parameters have been calculated self-consistently in some typical crystal structures for cathode materials.[11] Based on these results, we chose *U* values of 6 eV, 5.5 eV and 4.2 eV for Ni in the Li-Ni-O_2 system, Co in Li-Co-O_2 system, and Mn in Li-Mn-O_2 system, respectively. The value of *U* tends to become smaller as the valence state of the ion decreases. Hence, these values of *U* may be somewhat too large for strongly reduced states (e.g. NiO and MnO).

Ternary Li-M-O_2 phase diagrams in this thesis are constructed by projecting the vertices of the three-dimensional energy convex hull onto the two-dimensional Gibbs triangle, describing the Li-M-O_2 composition space. This construction assures that each point in the phase diagram represents the phase or combination of phases with the lowest energy. Introducing temperature into *ab initio* phase stability calculations is a complex procedure which involves the calculation of the relevant vibrational, configurational and electronic excitations.[81-85] However, in reactions that involve the loss of oxygen, the reaction entropy is dominated by the creation of O_2 gas, and the effect of temperature is effectively to lower the chemical potential of O_2 in the system, thereby decreasing the

free energy of reduced products. Hence, for the general decomposition reaction of a lithium transition metal oxide,

$$Li_xM_yO_{z+z'} \rightarrow Li_xM_yO_z + {}^{z'}\!/_{2}\, O_2, \tag{2-4}$$

the entropy change ΔS originates mainly from the oxygen gas released. Assuming the temperature dependence of the reaction enthalpy is small compared to the $-T\Delta S$ term, the reaction Gibbs free energy can be approximated by,

$$\Delta G = \Delta H - T\Delta S \approx -E^{\circ}(Li_xM_yO_{z+z'}) + E^{\circ}(Li_xM_yO_z) + {}^{z'}\!/_{2}\, E^{*}(O_2) - T\Delta S \tag{2-5}$$

where "E°" refers to the total energy at 0 K and "$E^{*}(O_2)$" is the calculated energy of an O_2 molecule at 0 K plus 1.36 eV per O_2 molecule to compensate for the GGA error in O_2. This correction also includes the $P\Delta V$ contribution to the enthalpy as we discussed in the previous section. We have compared the calculated oxidation enthalpies at 0 K with the experimental values at room temperature for typical transition metal oxides, and estimated the enthalpy difference to be less than 10 kJ per mole of O_2 [10]. This is significantly smaller than the contribution from the entropy of O_2 gas formation which is about 110 kJ/mol at 500K [48]. Thus, in our approach the temperature dependence in ΔG is exclusively given by the $-T\Delta S$ term, where ΔS corresponds to the oxygen gas entropy. A reference state with oxygen partial pressure of one atmosphere is assumed. The temperature for which the reaction Gibbs free energy in equation (2-5) equals zero is the thermodynamic transition temperature at which a stable compound on the left hand side of (2-4) becomes unstable with respect to compounds on the right hand side of (2-4).

$$T = \frac{\Delta H}{\Delta S} \approx \frac{-E^{o}(Li_xM_yO_{z+z'}) + E^{o}(Li_xM_yO_z) + {}^{z'}\!/_{2}\, E^{*}(O_2)}{{}^{z'}\!/_{2}\, S(O_2)} \tag{2-6}$$

The entropy for oxygen gas is a function of temperature and can be obtained from the *JANAF* thermochemistry tables.[48] We solve equation (2-6) iteratively: The entropy value for oxygen gas at room temperature is first used in equation (2-6) to estimate the thermodynamic transition temperature T. The entropy value for oxygen gas at the predicted temperature is then used to calculate the transition temperature T again. This iteration proceeds until the new predicted temperature T differs from the previous temperature value by less than 20 K.

2.4.2 Li_xNiO_2

In order to clarify the origin of heat generation during the phase transformations, particularly for the decomposition reaction of a spinel phase into a rock-salt phase, we have calculated the ternary phase diagram (see Figure 2-7) for Li-Ni-O_2 at 0 K using GGA+U with U on Ni = 6 eV, which is the self-consistently calculated value for Ni^{4+} ions in the layered structure.[11] Note that this is an approximation since the U value depends on the oxidation state and crystal environment, both of which are changing during the decomposition. However, the U value needs to be fixed to one consistent value in order to have reasonable reaction energies. The diagram shows the stable compounds and three-phase equilibria at 0 K. Delithiation of layered $LiNiO_2$ proceeds along the line that connects this composition with NiO_2. There are no thermodynamically stable partially delithiated states (composition 4, 5 and 6 in Figure 2-7 were tested) even though metastable Li-vacancy ordered states are known to exist.[86-88] The delithiation path for $0.5 < x < 1$ lies on the edge of the $LiNiO_2$-$LiNi_2O_4$-NiO equilibrium triangle so that the delithiated phases are unstable with respect to the formation of spinel:

$$Li_xNiO_2(layered) \rightarrow (1-x)LiNi_2O_4(spinel) + (2x-1)LiNiO_2(layered) \quad (2\text{-}7)$$

This reaction occurs without a loss of oxygen. For x < 0.5 the situation is qualitatively different as the delithiation path cuts through the $LiNi_2O_4$-NiO-O_2 equilibrium triangle, indicating that the layered phase may degrade through the formation of O_2 gas, spinel $LiNi_2O_4$ and NiO:

$$Li_xNiO_2(layered) \rightarrow xLiNi_2O_4(spinel) + (1-2x)NiO(rocksalt) + \frac{(1-2x)}{2}O_2 \quad (2\text{-}8)$$

We also computed the energy of a pseudospinel $(Li_3Ni_2^{2+})_{tet}(Ni_7^{3+}Ni_3^{4+})_{oct}O_{20}$ as has been suggested to occur experimentally,[19] but did not find it to be stable. It may become more stable at higher temperature due to the mixing entropy induced by Li and Ni sharing sites. An alternative explanation is that the pseudospinel is observed in experiments as a transient state towards the formation of $LiNi_2O_4$ spinel and NiO.

The calculated enthalpies for reactions (2-7) and (2-8) are shown in Figure 2-8. In agreement with experiments we find that the conversion from the layered structure to spinel is exothermic. The measured value at $x = 0.75$ is more negative than our calculated number, though we point out that the excess Ni which is always present in experimental samples may change the reaction energy. At $x = 0.25$, we find that the conversion of the layered structure to a perfectly ordered spinel with NiO and O_2 gas gives an even more negative reaction heat, while the formation of the pseudospinel phase generates a much less heat. This is in accordance with the spinel being the most stable reaction product. The two available experimental values at $x = 0.25$ [18, 89] fall between our calculated reaction heat for forming spinel and pseudospinel which may indicate that either an intermediate phase between the two structures (more ordered pseudospinel) or a mixture of the two phases is formed. The phase diagram in Figure 2-7 and the heats of reaction in

Figure 2-8 agree well with experiments indicating that our approach can at least predict the thermodynamically stable phases.

Figure 2-7 shows that partially delithiated layered phases are thermodynamically unstable against spinel. Whether these transitions occur will depend on the mobility of the Ni ions. Layered to spinel conversion requires the migration of Ni ions into the Li slab space passing through the intermediate tetrahedral sites. Ni^{4+} is known to have a strong octahedral site preference due to its filled t_{2g} states [2] while Ni^{3+} has a somewhat weaker octahedral preference. Both ions are therefore not very mobile which explains the kinetic stability of the material at room temperature and slightly above [17]. Given that the transformation from the layered structure to spinel requires elevated temperature, it is possible that the $LiNi_2O_4$ spinel becomes thermodynamically unstable before it can be achieved kinetically from the layered phase. Figure 2-9 shows the calculated temperature evolution of the system. The temperatures in the Figure 2-9 are estimated using equation (2-6). As temperature increases, we find that spinel $LiNi_2O_4$ becomes thermodynamically unstable towards products with lower average oxidation state of Ni according to the following reaction:

$$LiNi_2O_4(spinel) \rightarrow LiNiO_2(layered) + NiO(rocksalt) + (1/2)O_2 \qquad (2\text{-}9)$$

In this reaction half of the Ni cations are reduced to Ni^{2+}. The reaction enthalpy of (2-9) is calculated to be 218 meV (*endothermic*) per formula unit of $LiNi_2O_4$. The value of this decomposition heat can be more positive if a disordered rocksalt structure is formed instead of the mixture of $LiNiO_2$ and NiO. The temperature at which spinel becomes thermodynamically unstable is quite low in our calculations and would imply that it should not exist at room temperature. Several factors may influence this result.

Inaccuracies in DFT, in the chosen U values, or in the entropy approximations in equation (2-5) and (2-6) could all modify this temperature. In addition, real $LiNiO_2$ always contains Ni excess, and the created Ni^{2+} may stabilize the material somewhat against reduction.

Hence, if spinel is unstable at room temperature, or its formation is kinetically limited, direct conversion to $LiNiO_2$, NiO and O_2 will occur according to,

$$Li_xNiO_2(layered) \rightarrow xLiNiO_2(layered) + (1-x)NiO(rocksalt) + \frac{(1-x)}{2}O_2 \qquad (2\text{-}10)$$

The reaction enthalpy of (2-10) is calculated to be 28 meV, 5 meV and -93 meV per formula unit of Li_xNiO_2 respectively for x = 0.75, x = 0. 5 and x = 0.25, indicating that the heat generation depends on Li content x. The reaction enthalpy in equation (2-10) changes from positive to negative as the amount of oxygen generated increases. Arai et al. [90] have reported that the overall layered to rock-salt transformation is endothermic for $x \geq 0.4$, and exothermic for $x < 0.3$, which is consistent with our calculations.

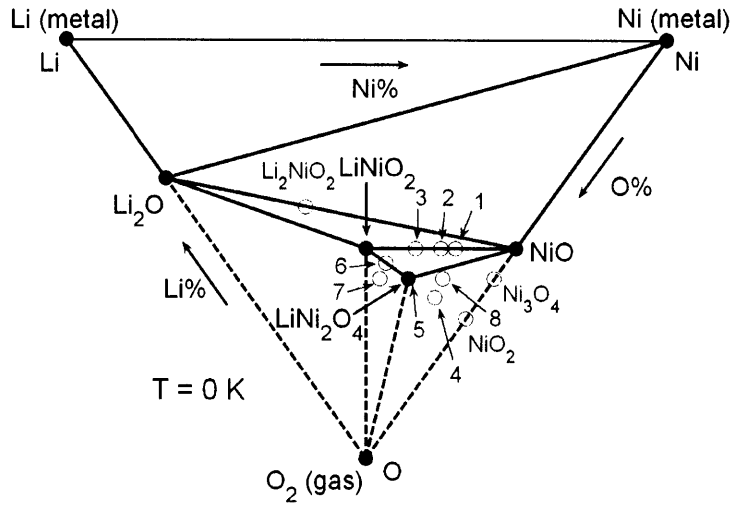

Figure 2-7 Calculated ternary phase diagram for Li-Ni-O_2 at 0 K. Dashed lines indicate that triangles connecting O_2 depend on pressure. Filled (unfilled) circles indicate stable (unstable) compounds. Points labeled as 1, 2 and 3 represent rock-salt structures of composition $Li_xNi_{1-x}O$ with x = 0.2, 0.25 and 0.33. Points labeled as 4, 5 and 6 are layered structures of composition Li_xNiO_2 with x = 0.25, 0.5 and 0.75. Points labeled as 7 and 8 are pseudospinel structures of composition $(Li_3)_{tet}(LiNi_5^{4+})_{oct}O_{12}$ and $(Li_3Ni_2^{2+})_{tet}(Ni_7^{3+}Ni_3^{4+})_{oct}O_{20}$. Li_2NiO_2 has an orthorhombic structure.[91] Ni_3O_4 has a spinel structure $(Ni^{2+})_{tet}(Ni_2^{3+})_{oct}O_4$.

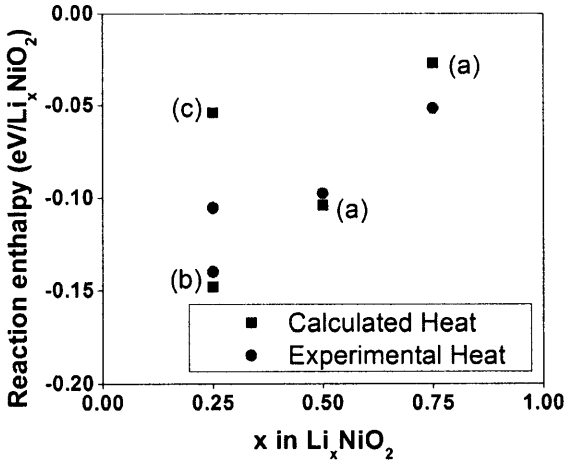

Figure 2-8 Calculated and experimental enthalpies for the reaction of layered Li_xNiO_2 to spinel. Circles are experimental results [18, 89]. Squares are calculated results. Points labeled as (a) are calculated according to reaction (2-7). Point labeled as (b) is calculated according to reaction (2-8). Point labeled as (c) indicates the formation of pseudospinel phase $(Li_3Ni_2^{2+})_{tet}(Ni_7^{3+}Ni_3^{4+})_{oct}O_{20}$ plus oxygen gas in the layered to spinel conversion.

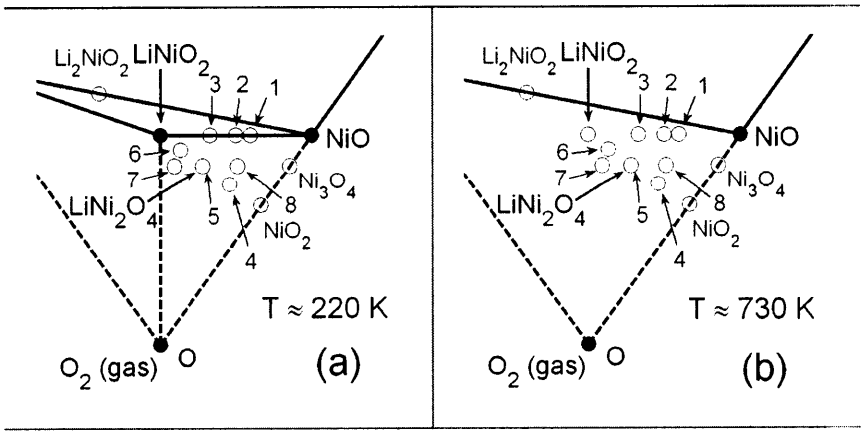

Figure 2-9 Temperature evolution of ternary phase diagram of Li-Ni-O_2. Filled (unfilled) circles indicate stable (unstable) compounds. Points labeled as 1-8 are the same as those in Figure 2-8.

2.4.3 Li_xCoO_2

Figure 2-10 shows the calculated ternary diagram for Li-Co-O_2 at T = 0 K and the temperature evolution of the system. Similar to the situation in the Ni system, our T = 0 K calculation (see Figure 2-10a) confirms that partially delithiated Li_xCoO_2 (composition 1, 2 and 3 in Figure 2-10 were tested) is thermodynamically unstable against the formation of spinel $LiCo_2O_4$ and some other products.[2, 3, 92] Spinel Co_3O_4 appears as a stable phase in the Li-Co-O_2 phase diagram. This is different from the Ni system since Ni_3O_4 is not stable and NiO forms instead. For $0.5 < x < 1$ the delithiation path lies on the edge of the $LiCoO_2$-$LiCo_2O_4$-Co_3O_4 equilibrium triangle so that delithiated phases form spinel through the reaction:

$$Li_xCoO_2(layered) \rightarrow (1-x)LiCo_2O_4(spinel) + (2x-1)LiCoO_2(layered) \qquad (2\text{-}11)$$

For $x < 0.5$ the delithiation path cuts through the $LiCo_2O_4$-Co_3O_4-O_2 equilibrium triangle indicating that the layered phase may degrade with a loss of O_2:

$$Li_xCoO_2(layered) \rightarrow xLiCo_2O_4(spinel) + \frac{(1-2x)}{3}Co_3O_4(spinel) + \frac{(1-2x)}{3}O_2 \qquad (2\text{-}12)$$

The loss of oxygen here is less than the amount in the Ni system (on a per formula unit basis) due to the reduction to Co_3O_4 in the Co-system, as compared to NiO in the Ni-materials.

The calculated reaction enthalpies indicate that reactions (2-11) and (2-12) are all *exothermic* at the four compositions we tested (see line (a) in Figure 2-11). Thus, the conversion from the partially delithiated layered to the spinel structure is energetically favored at all temperatures and will occur at a temperature where the Co cation gains enough mobility. In our calculations spinel $LiCo_2O_4$ becomes thermodynamically

unstable as temperature increases (see Figure 2-10b to 2-10d), and decomposes into layered $LiCoO_2$, Co_3O_4 and O_2:

$$LiCo_2O_4(spinel) \rightarrow LiCoO_2(layered) + (1/3)Co_3O_4(spinel) + (1/3)O_2 \quad (2\text{-}13)$$

Reaction (2-13) is calculated to be *endothermic* with an enthalpy change of 190 meV per formula unit of $LiCo_2O_4$. Hence, the equilibrium reaction path for delithiated layered Li_xCoO_2 would be the *exothermic* conversion of partially delithiated layered Li_xCoO_2 to spinel, followed by the *endothermic* decomposition of spinel $LiCo_2O_4$ to layered $LiCoO_2$ and Co_3O_4.

Whether in reality the spinel appears as a stable intermediate, or direct decomposition of the layered phase occurs depends on whether the temperature at which the Co ions become mobile is above or below the thermodynamic transition temperature for the spinel decomposition reaction. The kinetic limitation of converting the partially delithiated layered Li_xCoO_2 to spinel was suggested by previous theoretical work due to the high activation barrier found for Co migration.[1, 2] Ligand field splitting of electron levels gives Co^{3+} a very strong preference for octahedral sites, limiting its ability to hop through tetrahedral sites. Slow reaction kinetics for the decomposition reaction (2-1) is also observed in experimental studies,[22, 89] particularly for the highly discharged states. If spinel $LiCo_2O_4$ does not form, decomposition would proceed according to reaction (1), as suggested by Dahn.[16]

In Figure 2-11 we show the calculated reaction heat for the direct decomposition of layered Li_xCoO_2 following reaction (2-1). The dashed line shows the contribution from the *exothermic* layered to spinel conversion according to reactions (2-11)-(2-12) and the dotted line shows the contribution from the *endothermic* spinel decomposition according

to reaction (2-13). The overall reaction heat of (2-1) is the combination of the two reaction heats and is calculated to be -93 meV, -51 meV and 5 meV per formula unit of Li_xCoO_2, respectively for $x = 0.25$, $x = 0.5$ and $x = 0.75$. The reaction heat changes from negative to positive as x increases, similar to what we find in the Ni system. The result for the reaction heat at $x = 0.5$ compares well with Yamaki et.al 's DSC measurements [21] of -50 J/g (-49 meV per formula unit of Li_xCoO_2). Their measurement at $x = 0.75$ gives an exothermic reaction enthalpy of -20 J/g (-20 meV per formula unit of Li_xCoO_2), which is between the heat released in the layered to spinel conversion and the heat resulting from spinel decomposition. This may imply that in experiments reaction (2-1) in $Li_{0.75}CoO_2$ is not complete.

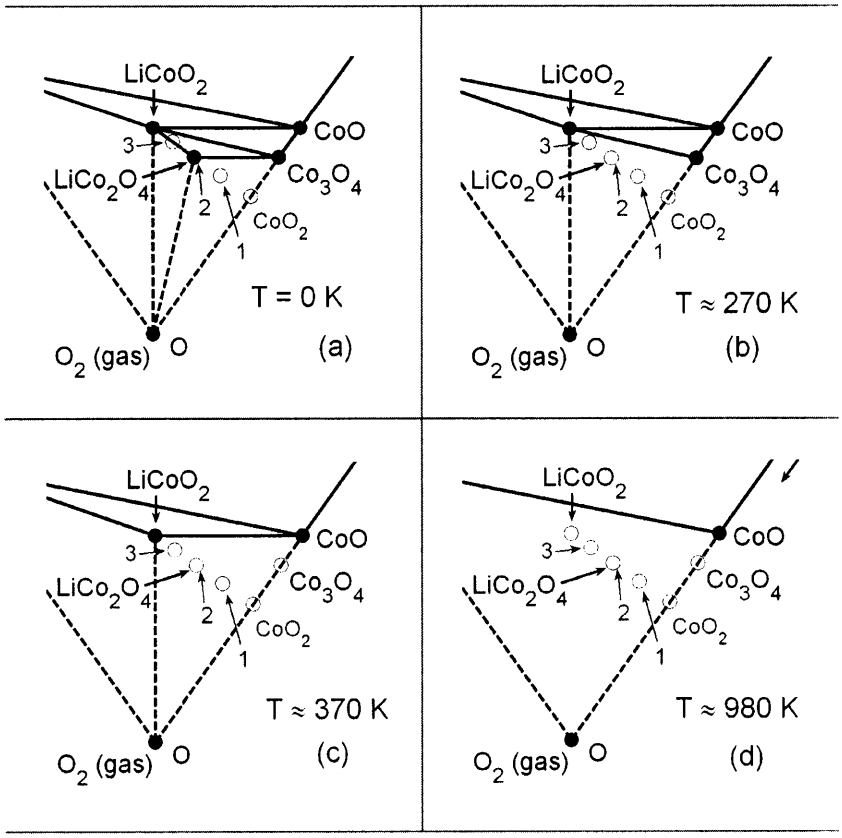

Figure 2-10 Ternary phase diagram of Li-Co-O_2 at 0 K and its temperature evolution. Filled (unfilled) circles indicate stable (unstable) compounds. Points labeled as 1, 2 and 3 are layered structures of composition Li_xCoO_2 with x = 0.25, 0.5 and 0.75.

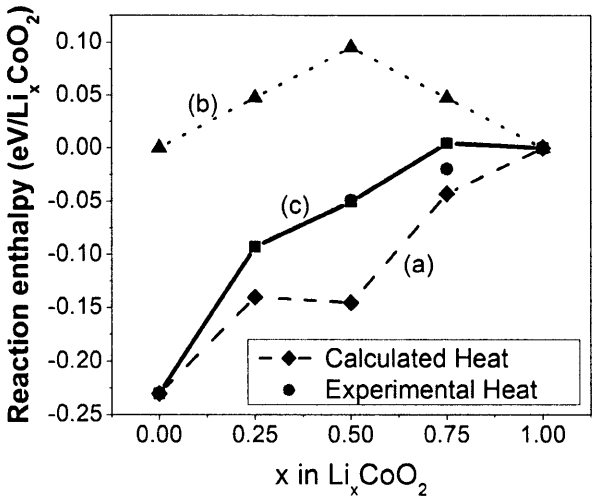

Figure 2-11 Calculated and experimental enthalpies for the decomposition of layered Li_xCoO_2 as a function of the Li composition *x*: (a) diamond points are calculated reaction heat for the layered to spinel composition (reaction (2-11) to (2-12) in text); (b) triangle points represent the reaction heat for the spinel decomposition (reaction (2-13) in text); (c) square points show the overall reaction heat for the direct decomposition of layered Li_xCoO_2 (reaction (2-1) in text). The two available experimental values [21] are marked by circles.

2.4.4 $Li_xMn_2O_4$

Our phase diagram in Figure 2-12 shows that delithiated spinel (composition 1 was tested in Figure 2-12) is metastable with respect to β-MnO_2 formation. As this transformation requires reshuffling of the oxygen layers, it is unlikely to occur at low temperature. Thus, in constrast to Li_xNiO_2 and Li_xCoO_2, $LiMn_2O_4$ is not thermodynamically unstable with respect to oxygen loss upon delithiation since the β-MnO_2–$LiMn_2O_4$ tie line is part of a stable three-phase triangle in the phase diagram.

Hence, we will focus on the spinel $Li_xMn_2O_4$ at composition $x = 0$ and 1, and discuss the possible degradation mechanism for the material at elevated temperatures. According to our calculated Li-Mn-O_2 ternary phase diagram (see Figure 2-12), cubic spinel $LiMn_2O_4$ appears in the diagram as a stable phase. As the temperature increases, $LiMn_2O_4$ decomposes in several characteristic stages. In going from Figure 2-13b to Figure 2-13c, $LiMn_2O_4$ has decomposed into monoclinic Li_2MnO_3 and tetragonal spinel Mn_3O_4. Further increasing the temperature towards Figure 2-13d leads to a reaction where Li_2MnO_3 disappears by reacting with some of the Mn_3O_4 to form orthorhombic $LiMnO_2$. Further reactions (Figure 2-13e to 2-13f) lead to the formation of MnO and disappearance of all ternary compounds from the phase diagrams. The phases appearing as decomposition products of $LiMn_2O_4$ compare well with those observed in Tsuji's experimental thermal stability studies at this Li content.[40] The calculated ternary phase diagram also provides the decomposition information for the fully delithiated $LiMn_2O_4$ (λ-Mn_2O_4 in Figure 2-12 and Figure 2-13): λ-Mn_2O_4 is unstable compared to β-MnO_2, and is gradually reduced to α-Mn_2O_3, Mn_3O_4 and MnO according to our phase diagram (Figure 2-12, Figure 2-13a to 13b, 13e). Decomposition products β-MnO_2, α-Mn_2O_3 and Mn_3O_4 are observed in experiments,[39] but the highly reduced product MnO has not been reported.

Since Li_2MnO_3 is only stable as a decomposition product in a narrow temperature range, we consider directly the decomposition of spinel $LiMn_2O_4$ into orthorhombic $LiMnO_2$, Mn_3O_4 and O_2 following the reactions below,

$$LiMn_2O_4 \rightarrow LiMnO_2 + (1/3)Mn_3O_4 + (1/3)O_2 \qquad (2\text{-}14)$$

The reaction enthalpy of (2-14) is calculated to be 0.984 eV per formula unit of $LiMn_2O_4$. This is close to Tsuji's experimental results of 547 ± 70 J/g (1.035 eV per formula unit of $LiMn_2O_4$) [40]. Note that reaction (2-14) is calculated to be highly endothermic compared to the decomposition of spinel $LiNi_2O_4$ and $LiCo_2O_4$, indicating a thermodynamically controlled decomposition of $LiMn_2O_4$. However, the large and positive reaction entropy from oxygen gas can make the decomposition reaction (2-14) favorable at high temperature.

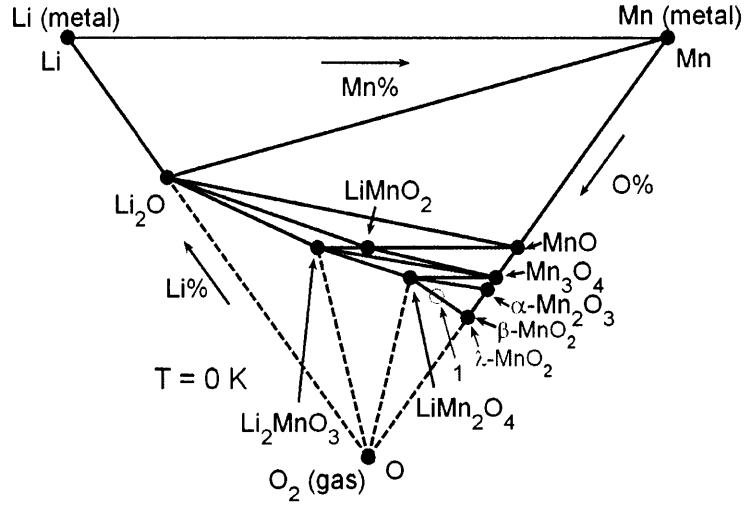

Figure 2-12 Calculated ternary phase diagram for Li-Mn-O_2 at 0 K. Point labeled as 1 is the half delithiated spinel with a composition of $Li_{0.5}Mn_2O_4$. Filled (unfilled) circles indicate stable (unstable) compounds.

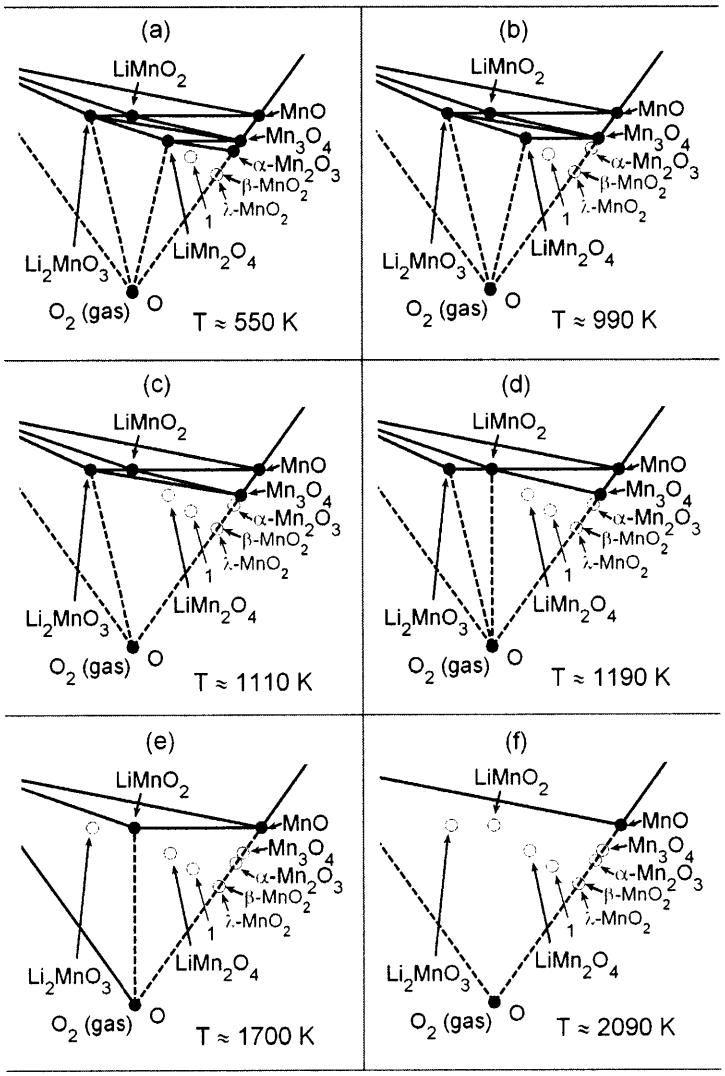

Figure 2-13 Temperature evolution of ternary phase diagram of Li-Mn-O_2. Filled (unfilled) circles indicate stable (unstable) compounds. Point labeled as 1 is the half delithiated spinel with a composition of $Li_{0.5}Mn_2O_4$.

2.4.5 Extension to quaternary system

We are interested in building an *ab initio* framework that is applicable to study the thermal stability problem for as many cathode materials as possible. The methodology presented above is suitable to investigate any cathode material with a ternary chemistry. However, many of the interesting cathode materials nowadays are quaternary lithium

transition metal compounds. Mathematically, the underlying convex hull methodology used in our model works well even at high dimensions. One practical difficulty is to find an effective presenting scheme to display the results at high dimensions. We further extend the methodology and demonstrate it on the interesting $LiFePO_4$ quaternary system. More details can be found in Ref. 93.[93]

2.4.6 Impacts of organic electrolyte

In practical batteries it is the stability of the cathode materials in the organic electrolyte that is important. To simulate the safety of real battery systems, the effects of the electrolyte need to be included in our model. Previous experimental studies of the reactions between electrolyte and cathode materials have shown that cathode materials can be more reactive in the presence of electrolyte, and that the reaction heat is consistent with what is expected from the combustion of electrolyte by the oxygen gas released as the cathode material decomposes.[21, 22, 94, 95] The electrolyte can modify the stability of pure cathode results in three ways:

1) It can catalyze electrode decomposition reaction at the electrode surface.
2) Its combustion equilibrium creates a low oxygen chemical potential in the system which will reduce the electrode at lower temperature than for a pure cathode.
3) Its combustion with oxygen from the electrode decomposition adds exothermic heat to the overall reaction.

We will focus on the thermodynamics of the reactions between electrolyte and cathode materials and the modifications to the heat flow. As a case study, ethylene

carbonate (EC) is selected to represent the electrolyte in our study. In reality EC is always used together with diethyl carbonate (DEC) and both of them can combust.

The combustion of electrolyte depends upon the environmental oxygen chemical potential. If we consider the full combustion of EC, the reaction can be expressed by:

$$2C_3H_4O_3 + 5O_2 \rightarrow 6CO_2 + 4H_2O \tag{2-15}$$

We calculated the energy of EC in its solid state with a space group of C*2/c* [96] and added the experimental measured heat of melting [97] to obtain the energy of its liquid state. The other species were calculated as molecules. The resulting reaction heat of -10.577 eV per formula of EC is in reasonable agreement with the experimental value of -11.187 eV per formula of EC.[98] The critical oxygen chemical potential which turns the reaction Gibbs free energy of (2-15) negative is given by,

$$\begin{aligned} &\mu_{O_2} = \tfrac{6}{5}\mu_{CO_2} + \tfrac{4}{5}\mu_{H_2O} - \tfrac{2}{5}\mu_{C_3H_4O_3} \approx \\ &\tfrac{6}{5}\left(E^{\circ}_{CO_2} - TS_{CO_2}\right) + \tfrac{4}{5}\left(E^{\circ}_{H_2O} - TS_{H_2O}\right) - \tfrac{2}{5}\left(E^{\circ}_{C_3H_4O_3} - TS_{C_3H_4O_3}\right) \end{aligned} \tag{2-16}$$

Here "E°" represents the energy of each specie at 0 K in a pure molecule or solid state and "*S*" implies the entropy at temperature "*T*". For the combustion of EC to be thermodynamically favorable, oxygen has to be provided by the environment at a chemical potential larger than the value given in equation (2-16). Figure 2-14 shows this critical oxygen chemical potential in equation (2-16) as a function of temperature. The oxygen chemical potential of oxygen gas (at a pressure of one atmosphere) is also plotted in Figure 2-14 and it lies much higher than the critical oxygen chemical potential for the combustion reaction (2-15). The third relevant oxygen chemical potential is the one established by an O_2-producing decomposition reaction. In that case,

$$\mu_{O_2} = \frac{2}{z'}\left(\mu_{Li_xM_yO_{z+z'}} - \mu_{Li_xM_yO_z}\right) \approx \frac{2}{z'}\left(E^o(Li_xM_yO_{z+z'}) - E^o(Li_xM_yO_z)\right) \qquad (2\text{-}17)$$

This equilibrium oxygen chemical potential is independent of temperature if the reaction energies on the right hand side of equation (2-17) are temperature independent. In Figure 2-14 we also plotted this chemical potential for several decomposition reactions of the three cathode materials evaluated in this thesis. Solid lines (a) and (b) give the decomposition reactions of spinel $LiNi_2O_4$ and $LiCo_2O_4$ according to reactions (2-9) and (2-13) respectively; line (c) represents the decomposition of Co_3O_4 into CoO; line (d) represents the decomposition of λ-Mn_2O_4 into α-Mn_2O_3; line (e) indicates the decomposition of spinel $LiMn_2O_4$ following reaction (2-14). Note that lower oxygen chemical potentials in these decomposition reactions indicate higher stability, i.e. the system has less power to oxidize its environment or release oxygen. At a temperature where the critical oxygen chemical potential for the decomposition of cathode material equals the chemical potential of oxygen gas, the decomposition reaction becomes thermodynamically favorable and oxygen gas is spontaneously generated from the cathode materials. It can also be seen from Figure 2-14 that the critical oxygen potentials for cathode decomposition are all above the one for the combustion reaction of the electrolyte, indicating that the reduction of cathode materials by the electrolyte is thermodynamically possible, and can occur at the surface of cathodes. However, at low temperature it is unlikely that this occurs in bulk for the same reason that EC does not spontaneously combust in air even though its thermodynamics allow it to. A more likely scenario is that electrolyte combustion by a charged cathode can only start at a temperature above its flash point, and high enough to favor oxygen release from the cathode.

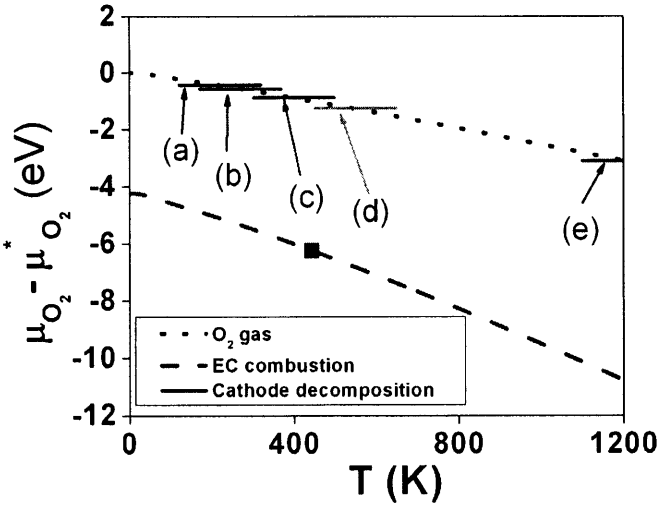

Figure 2-14 Calculated critical oxygen chemical potentials μ_{O_2} as a function of temperature. All μ_{O_2} are shown with their differences from the oxygen chemical potential at 0 K (denoted as $\mu^*_{O_2}$). Dotted line shows the change in μ_{O_2} for oxygen gas as temperature increases. Dashed line shows the critical μ_{O_2} for the combustion reaction of ethylene carbonate (EC). Solid lines show the critical μ_{O_2} for different decomposition reactions of cathode materials. See the text for detail about the specifications of each solid line. Flash point of EC is marked with a square.

Under such a scenario the temperature at which the bare electrode (i.e. without electrolyte) releases O_2 gas, is still the critical temperature at which decomposition starts, but the presence of the electrolyte significantly modifies the reaction heat and enhances decomposition by further heating the system: Hence, while this is not a true catalytic effect, the heat generation by the electrolyte may help sustain the cathode decomposition reaction at a lower temperature than when no electrolyte is present.

Our results confirm the known hierarchy of safety issues in cathode materials. Even though it suffers from other capacity loss problems, spinel $LiMn_2O_4$ is a stable and safe material. Even the fully delithiated spinel Mn_2O_4 requires high temperature to initialize decomposition with oxygen loss (line (d) in Figure 2-14). In the presence of electrolyte the layered $LiNiO_2$ and $LiCoO_2$ have more safety issues, since the delithiated phases at low Li concentration can decompose with a loss of oxygen. The electrolyte plays the role of oxygen sink and creates a highly exothermic reaction, which further facilitates the decomposition of layered Li_xMO_2. Taking $Li_{0.5}CoO_2$ as an example, Figure 2-14 (line b and c) shows that around the flash point of EC, $Li_{0.5}CoO_2$ can decompose into Co_3O_4 or CoO with the release of oxygen. This is consistent with what is found by MacNeil et al. in their experimental study [94]. If EC is considered to be in excess, and a full combustion is assumed, the possible reactions between EC and $Li_{0.5}CoO_2$ can be summarized as,

$$Li_{0.5}CoO_2 + (1/15)C_3H_4O_3 \rightarrow (1/2)LiCoO_2 + (1/6)Co_3O_4 + (1/5)CO_2 + (2/15)H_2O \quad (2\text{-}18)$$

$$Li_{0.5}CoO_2 + (1/10)C_3H_4O_3 \rightarrow (1/2)LiCoO_2 + (1/2)CoO + (3/10)CO_2 + (1/5)H_2O \quad (2\text{-}19)$$

depending on the different reduction products of $Li_{0.5}CoO_2$. The reaction enthalpies of (2-18) and (2-19) are calculated to be -0.982 eV and -1.375 eV per formula of $Li_{0.5}CoO_2$, which is -1004 J/g and -1406 J/g respectively based on the weight of $Li_{0.5}CoO_2$. Reaction (2-18) and (2-19) generate a different amount of heat due to the different amounts of oxygen gas released by the decomposition reactions of $Li_{0.5}CoO_2$. These calculated numbers of reaction heats are in good agreement with the experimental value of 1000 $\pm$ 250 J/g, reported by Baba et al. [22]. These reaction heats are substantially larger than the reaction heat for the exothermic decomposition of $Li_{0.5}CoO_2$ without the presence of electrolyte, and can cause the thermal runaway reactions inside the cells.

2.5 Discussions

In this section, we discuss our first-principles studies of oxidation energies for transition metal oxides and the thermal stability problems for cathode materials.

2.5.1 Accurate oxidation enthalpies for transition metal oxides

All calculated oxidation energies in Figure 2-5 are less negative than experimental values when GGA is used. We believe that this error is systematic and has two distinct contributions. The first and most obvious error originates from the inaccuracy of GGA in reproducing the O_2 change of state. The O_2 molecule binds too strongly in GGA and its dissociation in oxidation reactions therefore requires too much energy leading to an underestimation of the oxidation energy. It is not likely that the GGA error in describing the covalent bonding of O_2 cancels in the reaction energy as the oxygen ion has limited covalency in the oxide. Rather than correcting reaction energies with the difference between the calculated and experimental binding energy of O_2, we choose to fit a correction to the formation enthalpy of simple non-transition metal oxides, such as Li_2O, MgO, etc. This allows us to include any correlation energy error associated with adding two electrons to the oxygen *p*-orbital.

We believe that the remaining error, after the oxygen change of state is corrected, is due to the correlation energy in the 3*d*-metal states. This error will also be present in oxidation reactions that do not involve O_2 molecules. The correlation energy can clearly be identified (Figure 2-5): all GGA oxidation energies are too negative, indicating that GGA penalizes the reduced state where more 3*d*-orbitals are filled. This is familiar to

what has been observed for electrochemical redox energies (where the energy of O_2 does not play a role): the GGA self-interaction overestimates the energy of the filled $3d$-states, thereby artificially lowering redox potentials. In our results, the effect of the self-interaction is to increase the energy of the reduced state. It is then no surprise that increasing the localization into $3d$-orbitals and removing self-interaction from it with GGA+U decreases the magnitude of the oxidation energy, bringing it closer to experimental values.

Note that if an uncorrected O_2 energy is used, the pure GGA results in Figure 2-6 would be in better agreement with experiment, due to the cancellation of two substantial errors: underestimation of the oxidation energy due to the O_2 binding error and overestimation due to the self-interaction in $3d$-states. This cancellation is rather arbitrary and can not be relied on to get accurate results. Indeed, differences between calculated and experimental oxidation energies in GGA can be as high as 1 eV.

The U values that bring the calculated oxidation energies in agreement with experimental results are remarkably consistent for a given transition metal, which implies that the U values of different oxidation states may lie close together. This could make the GGA+U with the U values fitted here of practical value in predicting the potential and energy of redox processes more accurately.

We did not discuss oxides of Ti in this thesis. Ti-oxides have weakly localized d-orbital electrons, and when reduced are almost always metallic. The GGA+U approach used here (also referred as the "fully localized limit" (FLL) GGA+U), is developed to correct bandgap errors of insulators, and is not appropriate for such metallic systems.

Finally, we use the experimental reaction enthalpy data at room temperature, while our first principles calculations results are for 0K. The enthalpy difference is estimated by integrating the heat capacity difference between the reactants and products from 0K to room temperature. We find that this difference is usually less than 10 kJ per mole O_2 (100 meV/molecule). Taking the oxidation of VO to VO_2 as an example, the enthalpy difference between 0K and room temperature is just 5.77 kJ per mole of O_2 reacted. This small enthalpy difference will have only a small influence on our results. The only exception is the reaction of cobalt oxide "6 $CoO+O_2 \rightarrow 2\ Co_3O_4$", which has a relative large enthalpy difference of 28 kJ per mole of O_2 reacted between room temperature and 0K. This difference would change the fitted U to 3.5 eV, compared to the value of 3.3 eV in Figure 2-6(e).

In conclusion, we have investigated the oxidation energies of 3*d* transition metal using GGA and GGA+U. When using O_2 as the oxidant, the error in the binding energy of O_2 is opposite to the error caused by the correlation error in the 3*d*-orbitals, and the two errors mask each other to some extent. Hence, GGA will be considerably more in error when calculating reactions where 3*d*-metals (oxides) are oxidized by means other than oxygen. The calculated reaction energies become correct for very reasonable and systematic values of U. Although GGA+U is semi-empirical in nature, it has been found to improve the accuracy in predicting the energetics of redox processes from first principles.

2.5.2 Thermal stability of cathode materials

Our first-principles calculations suggest that significant thermodynamic instabilities exist for charged electrode materials. The instability of delithiated layered and orthorhombic $LiMO_2$ (M = Ni, Co and Mn) structures towards spinel formation was already pointed out previously.[3, 92] This exothermic reaction can essentially proceed without changes in oxidation state of the cations and is unrelated to the reductive stability of the transition metal cation. Whether the layered to spinel structural conversions occur, depends on the kinetics of the cation diffusion. Mn^{3+} and Co^{3+} are known to have respectively the highest and lowest mobility among the three cations.[2] Thus, it is more difficult for layered Li_xCoO_2 to complete the conversion into a spinel structure. If the kinetic limitation of the layered to spinel transformation at low temperature inhibits the appearance of the intermediate spinel phase, a direct degradation of the layered structure into lower-valent transition metal oxides occurs, accompanied by the loss of oxygen. The overall reaction then consists of the *exothermic* layered-to-spinel conversion followed by the *endothermic* spinel decomposition. The possibility of metal reduction in charged electrodes by the transfer of metal ion to anode was previously suggested,[99] though diffusion of the transition metal ion through the solid state and through the electrolyte makes this difficult. Metal reduction by loss of oxygen on the cathode side, as modeled in this thesis, is a more likely reduction mechanism. We find that the reaction heat for the overall degradation (layered to lower-valent products) can change from positive to negative as the amount of oxygen released increases. Reflecting the different oxidation/reduction potentials of the different M^{4+} ions, the LiM_2O_4 spinels have very different decomposition enthalpies for M = Ni, Co and Mn. The decomposition of spinel $LiMn_2O_4$ is highly *endothermic*, about 0.984 eV per formula unit of $LiMn_2O_4$ if it

decomposes into orthorhombic $LiMnO_2$ and tetragonal Mn_3O_4. This reaction heat is considerably larger than the numbers for $LiNi_2O_4$ and $LiCo_2O_4$, 0.218 eV and 0.19 eV respectively. Under thermodynamic control the large and positive reaction enthalpy indicates that a relatively high temperature is needed for the decomposition of spinel $LiMn_2O_4$. As the thermodynamic transition temperature for the $LiNi_2O_4$ and $LiCo_2O_4$ spinels are rather low, their transitions may be kinetically limited.

The three systems have different decomposition products as temperature increases. This is particularly relevant for $x < 0.5$ in Li_xMO_2: from the calculated phase diagram layered Li_xNiO_2 is located in the O_2-NiO-$LiNi_2O_4$ (or O_2-NiO-$LiNiO_2$ at high temperature) equilibrium triangle, thus, it tends to degrade into rocksalt NiO with a loss of oxygen. For layered Li_xCoO_2 the presence of Co_3O_4 in the phase diagram gives decomposition products of spinel Co_3O_4 and O_2, and less oxygen is generated compared to the case of layered Li_xNiO_2. The delithiation of spinel $LiMn_2O_4$ proceeds along the $LiMn_2O_4$-(λ)Mn_2O_4 equilibrium line without any loss of oxygen, reflecting again the fact that Mn reaches the 4+ oxidation state more easily than Co or Ni.[100] The fact that it has both a thermodynamically very stable charged and discharged state gives the delithiated spinel $Li_xMn_2O_4$ more thermal stability compared to layered Li_xNiO_2 and Li_xCoO_2.

At elevated temperature the loss of oxygen for layered Li_xMO_2 brings safety issues for batteries since the released oxygen can react with the organic electrolyte inside the cell. Our study shows that the critical oxygen chemical potential needed to make the combustion of ethylene carbonate thermodynamically favorable is always below the critical oxygen chemical potentials for the decomposition reactions of cathode materials. Thus, the surface reduction of cathode materials by electrolyte is thermodynamically

possible. If we assume that the flash point of the electrolyte is the minimum temperature needed to start the reaction between O_2 and the electrolyte, then the bulk combustion will start at the flash point or at the temperature at which oxygen is released from the cathode material, whichever is greater. The heat of electrolyte combustion is one order of magnitude larger than those from the exothermic reactions of cathode materials. Even though the oxygen release reactions from the cathode are endothermic, the combustion of electrolyte by the released O_2 is highly exothermic making the overall reaction exothermic. As a result, the amount of heat generation depends almost linearly on the amount of oxygen consumed by the electrolyte if excess electrolyte is assumed. This suggests that in the presence of excess electrolyte layered Li_xNiO_2 can be more dangerous than Li_xCoO_2 as it generates more oxygen gas. On the contrary, spinel $LiMn_2O_4$ is less reactive compared the layered Li_xMO_2 since the delithiation can proceed without the loss of oxygen. Our result underscores the critical role that non-flammable electrolytes can play in the safety of Li-ion batteries.[101] The cathode decomposition is either mildly exothermic or endothermic (when O_2 is released), which in itself is less likely to lead to a runaway reaction. Only when the released O_2 finds a combustible reagent such as the electrolyte or anode, do strongly exothermic reactions occur.

In the present first-principles approach, the GGA+*U* method is crucial to understand the decomposition mechanisms and obtain accurate oxidation energies, particularly when the transition metal ion has an overall change in oxidation state. In some cases, the GGA approximation (without *U*) can give qualitatively incorrect reaction energies, and predict an *exothermic* reaction to be *endothermic* (e.g. decomposition of layered $Li_{0.25}CoO_2$, $Li_{0.5}CoO_2$ and $Li_{0.25}NiO_2$). The major uncertainty of the GGA+*U* method is the *U*

parameter. In this study we used U values self-consistently calculated in similar crystal structures [11]. U parameters determined in this way can give accurate reaction energies for most of the cases in this work, but if a reaction produces a large change in the valence state of transition metal ions, or a dramatic change in crystal structure, the selection of reasonable U values can be difficult. The decomposition of spinel $LiNi_2O_4$ to NiO serves as an example. This reaction has half of the Ni reduced from 4+ to 2+. Fitting the calculated formation energy of $LiNiO_2$ ($2Li_2O + 4NiO + O_2 \rightarrow 4LiNiO_2$) to the experimental value,[102] a U value of 5.2 eV is obtained. A decrease of U from 6 eV (used in this work) to 5.2 eV will increase the estimated decomposition temperature in Figure 2-9a from 220 K to 430 K. The latter temperature may be more reasonable since the presence of spinel $LiNi_2O_4$ as an intermediate phase has been reported in thermal stability tests of layered Li_xNiO_2.[19, 20, 103, 104] Quantitative prediction of thermal decomposition temperatures for some reactions is still a challenge.

The new approach presented in this work is promising to predict the thermal stability of charged cathode materials. We believe that this first-principles approach can be useful to better understand the decomposition mechanisms of cathode materials and we hope that it will contribute to the development of safe and stable electrode materials.

2.6 Future work

We have developed an *ab initio* method to study the thermal stability of cathode materials in Li-ion batteries. The key is to make reasonable approximations of temperature effects and use the calculated temperature dependent phase diagrams to analyze phase stability of charged cathode materials at elevated temperature. The success

of this approach relies on the accurate evaluation of oxidation reaction energies from first-principles. However, there are some uncertainties and drawbacks that one should be aware of.

First, the predictions of critical reaction temperature are rather crude in the present model. Currently, we approximate the reaction entropy of the thermal decomposition reaction by the entropy of oxygen gas. While this approximation of temperature effects provides a relatively simple and fast scheme to predict critical decomposition temperatures without performing extensive entropy calculations additionally, it has considerable limitations of bringing the accuracy of temperature predictions to a high level. Calculating the reaction enthalpies for transition metal oxides from density functional theory should be quite accurate, provided that the appropriate U values are used. The large amount of calculations needed for entropy evaluation is the real intimating factor. However, we can perform certain semi-empirical procedures to improve the temperature predictions. A potential solution is to approximate the temperature dependency of the reaction enthalpy and entropy with polynomial expansions. By choosing a number of transition metal oxides, the heat capacity data of which have been tabulated, we can fit the reaction enthalpy and entropy of those oxidation reactions with polynomial terms of temperature. Once we obtain the "expansion" coefficients, we can use them in the temperature predictions for thermal degradations of cathode materials. This is somewhat similar to the correction for oxygen energy that we currently use.

Second, the reaction enthalpies predicted for the decomposition of transition metal oxides are accurate conditioning on that we use the right U values in the GGA+U

calculations. The evaluation of accurate U values can be quite challenging for some cases and it is difficult to justify that the U values predicted from linear response theory [13] are appropriate for the calculation of all thermodynamic data, especially for those oxidation reactions where transition metal ions experience considerable change of oxidation states and coordination environments, e.g. Ni^{4+} in layered structure to Ni^{2+} in rocksalt structure. One needs to carefully choose the proper U values before performing large scale of GGA+U calculations for the thermal stability study of cathode materials with new chemistries.

Last, we do not consider the kinetics of the thermal degradation reactions in this model. Note that the thermal degradations studied in this thesis are of two categories: kinetically driven phase transformations and thermodynamically controlled ones. For the former reactions, we only determine the reaction enthalpy at 0K and leave the prediction of critical reaction temperature to the investigation of cation mobility at elevated temperature. For the latter reactions, we are currently predicting at which temperature the thermodynamically controlled reaction is energetically favorable and we do not determine how fast the degradation process can occur. The quantitative evaluation of reaction kinetics can be quite challenging from first-principles. However, it would be quite interesting if one can build a kinetic model to evaluate the reaction rate of those thermal degradation reactions. Combined with our current prediction of reaction enthalpies, one can provide valuable thermodynamic input data for the thermal stability modeling of Li-ion batteries at a macroscopic level.[105] For the investigation of oxidation/reduction reactions between cathode materials and organic electrolyte, we only studied the thermodynamic aspects and conclude that all reductions of cathode material

by electrolyte are energetically favorable. This is not surprising at all but the real reaction can be rate dependent. Therefore, one needs to consider the reaction at atomistic level and consider the kinetic reaction at the interface between cathode material and electrolyte. Recently, there are some modeling works that are pursuing in this direction. Atomic potentials computed from *ab initio* methods have been incorporated into the study of the interfacial reactions between cathode materials and electrolyte.[106] These modeling works can provide insights about the degradation reactions of cathode materials from a different perspective.

2.7 Conclusions

We have presented a new method for predicting the thermodynamics of thermal degradation of charged materials for rechargeable Li batteries and demonstrated on three cathode materials. The degradation mechanism and the calculated decomposition heat for the three systems are in good agreement with experiments. When present, the electrolyte can act as a sink for the oxygen released from the cathode. Although oxygen release from the cathode is generally endothermic, its combustion with the electrolyte leads to a highly exothermic reaction.

References:

[1] J. Reed, G. Ceder, and A. Van der Ven, Electrochem. Solid-State Lett. **4**, A78 (2001).

[2] J. Reed and G. Ceder, Chem. Rev. **104**, 4513 (2004).

[3] A. Van der Ven and G. Ceder, Phys. Rev. B **59**, 742 (1999).

[4] M. K. Aydinol, A. F. Kohan, and G. Ceder, J. Power Sources **68**, 664 (1997).

[5] A. Van der Ven, M. K. Aydinol, and G. Ceder, J. Electrochem. Soc. **145**, 2149 (1998).

[6] A. Van der Ven and G. Ceder, Electrochem. Solid-State Lett. **3**, 301 (2000).

[7] D. Morgan, A. Van der Ven, and G. Ceder, Electrochemical and Solid-State Letters **7**, A30 (2004).

[8] A. Van der Ven and G. Ceder, Electrochem. Commun. **6**, 1045 (2004).

[9] T. Maxisch, F. Zhou, and G. Ceder, Physical Review B **73**, 104301 (2006).

[10] L. Wang, T. Maxisch, and G. Ceder, Physical Review B **73**, 195107 (2006).

[11] F. Zhou, M. Cococcioni, C. A. Marianetti, D. Morgan, and G. Ceder, Phys. Rev. B **70**, 235121 (2004).

[12] V. I. Anisimov, F. Aryasetiawan, and A. I. Liechtenstein, J. Phys.: Condens. Matter **9**, 767 (1997).

[13] M. Cococcioni and S. de Gironcoli, Phys. Rev. B **71**, 035105 (2005).

[14] K. Kang, Y. S. Meng, J. Breger, C. P. Grey, and G. Ceder, Science **311**, 977 (2006).

[15] M. M. Thackeray, J. Electrochem. Soc. **142**, 2558 (1995).

[16] J. R. Dahn, E. W. Fuller, M. Obrovac, and U. v. Sacken, Solid State Ionics **69**, 265 (1994).

[17] M. G. S. R. Thomas, W. I. F. David, J. B. Goodenough, and P. Groves, Mater. Res. Bull. **20**, 1137 (1985).

[18] K. K. Lee, W. S. Yoon, K. B. Kim, K. Y. Lee, and S. T. Hong, J. Power Sources **97-98**, 321 (2001).

[19] M. Guilmard, L. Croguennec, D. Denux, and C. Delmas, Chem. Mater. **15**, 4476 (2003).

[20] H. Arai, S. Okada, Y. Sakurai, and J. Yamaki, Solid State Ionics **109**, 295 (1998).

[21] J. Yamaki, Y. Baba, N. Katayama, H. Takatsuji, M. Egashira, and S. Okada, J. Power Sources **119**, 789 (2003).

[22] Y. Baba, S. Okada, and J. Yamaki, Solid State Ionics **148**, 311 (2002).

[23] A. R. Armstrong and P. G. Bruce, Nature **381**, 499 (1996).

[24] F. Capitaine, P. Gravereau, and C. Delmas, Solid State Ionics **89**, 197 (1996).

[25] A. R. Armstrong, A. D. Robertson, and P. G. Bruce, Electrochim. Acta **15**, 285 (1999).

[26] P. G. Bruce, A. R. Armstrong, and R. L. Gitzendanner, J. Mater. Chem. **9**, 193 (1999).

[27] Y. Shao-Horn, S. A. Hackney, A. R. Armstrong, P. G. Bruce, R. Gitzendanner, C. S. Johnson, and M. M. Thackeray, J. Electrochem. Soc. **146**, 2404 (1999).

[28] M. M. Thackeray, Prog. Solid State Chem. **25**, 1 (1997).

[29] M. Winter, J. O. Besenhard, M. E. Spahr, and P. Novak, Adv. Mater. **10**, 725 (1998).

[30] P. G. Bruce, Chem. Commun. **19**, 1817 (1997).
[31] S. K. Mishra and G. Ceder, Phys. Rev. B **59**, 6120 (1999).
[32] G. Ceder and S. K. Mishra, Electrochem. Solid-State Lett. **2**, 11 (1999).
[33] Y. Chabre and J. Pannetier, Prog. Solid State Chem. **23**, 1 (1995).
[34] G. Dittrich and R. Hoppe, Z. Anorg. Allg. Chem. **368**, 262 (1969).
[35] R. Hoppe, G. Brachtel, and M. Jansen, Z. Anorg. Allg. Chem. **417**, 1 (1975).
[36] A. Blyr, C. Sigala, G. Amatucci, D. Guyomard, Y. Chabre, and J. M. Tarascon, J. Electrochem. Soc. **145**, 194 (1998).
[37] Y. M. Chiang, D. R. Sadoway, Y. Jiang, B. Huang, and H. Wang, Electrochem. Solid-State Lett. **2**, 107 (1999).
[38] G. Vitins and K. West, J. Electrochem. Soc. **144**, 2587 (1997).
[39] O. Schilling and J. R. Dahn, J. Electrochem. Soc. **145**, 569 (1998).
[40] T. Tsuji, H. Umakoshi, and Y. Yamamura, J. Phys. Chem. Solids **66**, 283 (2005).
[41] V. Massarotti, D. Capsoni, and M. Bini, Solid State Commun. **122**, 317 (2002).
[42] M. M. Thackeray, M. F. Mansuetto, and J. B. Bates, J. Power Sources **68**, 153 (1997).
[43] J. M. Tarascon, F. Coowar, G. Amatuci, F. K. Shokoohi, and D. G. Guyomard, J. Power Sources **54**, 103 (1995).
[44] R. O. Jones and O. Gunnarsson, Rev. Mod. Phys. **61**, 689 (1989).
[45] D. C. Patton, D. V. Porezag, and M. R. Pederson, Phys. Rev. B **55**, 7454 (1997).
[46] B. Hammer, L. B. Hansen, and J. K. Norskov, Phys. Rev. B **59**, 7413 (1999).
[47] O. Le Bacq, A. Pasturel, and O. Bengone, Phys. Rev. B **69** (2004).
[48] M. W. Chase, *NIST-JANAF Thermochemical Tables* (American Institute of Physics, Melville, NY, 1998).
[49] O. Kubaschewski, C. B. Alcock, and P. I. Spencer, *Materials thermochemistry* (Pergamon Press, Oxford, 1993).
[50] C. N. R. Rao and B. Raveau, *Transition Metal Oxides* (Wiley-VCH, New York, 1995).
[51] D. Adler, Rev. Mod. Phys. **40**, 714 (1968).
[52] J. Kubler and A. R. Williams, J. Magn. Magn. Mater. **54**, 603 (1986).
[53] H. Yamada, Y. Soejima, X. G. Zheng, and M. Kawaminami, Trans. Mater. Res. Soc. Jpn. **25**, 1199 (2000).
[54] B. X. Yang, J. M. Tranquada, and G. Shirane, Phys. Rev. B **38**, 174 (1987).
[55] M. Abbate, F. M. F. De Groot, J. C. Fuggle, Y. J. Ma, C. T. Chen, F. Sette, A. Fujimori, and Y. Ueda, Phys. Rev. B **43**, 7263 (1991).
[56] M. Regulski, R. Przeniosło, I. Sosnowska, and J. U. Hoffmann, Phys. Rev. B **68**, 172401 (2003).
[57] J. M. Tarascon, G. Vaughan, Y. Chabre, L. Seguin, M. Anne, P. Strobel, and G. Amatucci, J. Solid State Chem. **147**, 410 (1999).
[58] B. N. Brockhouse, J. Mater. Chem. **21**, 961 (1953).
[59] M. Regulski, R. Przeniosło, I. Sosnowska, D. Hohlwein, and R. Schneider, J. Alloys Compd. **362**, 236 (2004).
[60] V. Baron, J. Gutzmer, H. Rundloef, and R. Tellgren, Am. Mineral. **83**, 786 (1998).
[61] B. Chardon and F. Vigneron, J. Magn. Magn. Mater. **58**, 128 (1986).
[62] W. L. Smith and A. D. Hobson, Acta Crystallogr. Sect. B: Struct. Sci **29**, 362 (1973).

[63] W. Kündig, M. Kobelt, H. Appel, G. Constabaris, and R. H. Lindquist, J. Phys. Chem. Solids **30**, 819 (1969).
[64] R. Restori and D. Schwarzenbach, Acta Crystallogr. Sect. B: Struct. Sci **42**, 201 (1986).
[65] R. Enjalbert and J. Galy, Acta Crystallogr., Sect. C: Cryst. Struct. Commun. **42** (1986).
[66] A. Bystroem and K. A. Wilhelmi, Acta Chem. Scand. **4**, 1131 (1950).
[67] J. A. Pople, M. H. Gordon, D. J. Fox, K. Raghavachari, and L. A. Curtiss, J. Chem. Phys. **90**, 5622 (1989).
[68] V. I. Anisimov, J. Zaanen, and O. K. Andersen, Phys. Rev. B **44**, 943 (1991).
[69] W. E. Pickett, S. C. Erwin, and E. C. Ethridge, Phys. Rev. B **58**, 1201 (1998).
[70] I. V. Solovyev, P. H. Dederichs, and V. I. Anisimov, Phys. Rev. B **50**, 16861 (1994).
[71] R. Zimmermann, P. Steiner, R. Claessen, F. Reinert, S. Hufner, P. Blaha, and P. Dufek, J. Phys.: Condens. Matter **11**, 1657 (1999).
[72] C. Castellani, C. R. Natoli, and J. Ranninger, Phys. Rev. B **18**, 4945 (1978).
[73] A. Rohrbach, J. Hafner, and G. Kresse, Phys. Rev. B **70**, 125426 (2004).
[74] G. Rollmann, A. Rohrbach, P. Entel, and J. Hafner, Phys. Rev. B **69**, 165107 (2004).
[75] A. Chainani, T. Yokoya, T. Morimoto, T. Takahashi, and S. Todo, Phys. Rev. B **51**, 17976 (1995).
[76] W. L. Roth, J. Phys. Chem. Solids **25**, 1 (1964).
[77] J. van Elp, J. L. Wieland, H. Eskes, P. Kuiper, G. A. Sawatzky, F. M. F. de Groot, and T. S. Turner, Phys. Rev. B **44**, 6090 (1991).
[78] S. L. Dudarev, G. A. Botton, S. Y. Savrasov, C. J. Humphreys, and A. P. Sutton, Phys. Rev. B **57**, 1505 (1998).
[79] G. Kresse and D. Joubert, Phys. Rev. B **59**, 1758 (1998).
[80] G. Kresse and J. Furthmuller, Phys. Rev. B **54**, 11169 (1996).
[81] G. D. Garbulsky and G. Ceder, Phys. Rev. B **49**, 6327 (1994).
[82] J. M. Sanchez and D. de Fontaine, Phys. Rev. B **17**, 2926 (1978).
[83] M. Asta, R. McCormack, and D. de Fontaine, Phys. Rev. B **48**, 748 (1993).
[84] G. Ceder, Comput. Mater. Sci. **1**, 144 (1993).
[85] G. J. Ackland, J. Phys.: Condens. Matter **14**, 2975 (2002).
[86] M. E. A. Y. de Dompablo, A. Van der Ven, and G. Ceder, Phys. Rev. B **66**, 064112 (2002).
[87] C. Delmas, M. Menetrier, L. Croguennec, S. Levasseur, J. P. Peres, C. Pouillerie, G. Prado, L. Fournes, and F. Weill, Int. J. Inorg. Mater. **1**, 11 (1999).
[88] J. P. Peres, F. Weill, and C. Delmas, Solid State Ionics **116**, 19 (1999).
[89] Z. Zhang, D. Fouchard, and J. R. Rea, J. Power Sources **70**, 16 (1998).
[90] H. Arai and Y. Sokurai, J. Power Sources **81**, 401 (1999).
[91] K. Kang, C. H. Chen, B. J. Hwang, and G. Ceder, Chem. Mater. **16**, 2685 (2004).
[92] C. Wolverton and A. Zunger, J. Electrochem. Soc. **145**, 2424 (1998).
[93] S. P. Ong, L. Wang, B. Kang, and G. Ceder, Chem. Mater. **20**, 1798 (2008).
[94] D. D. MacNeil and J. R. Dahn, J. Electrochem. Soc. **148**, A1205 (2001).
[95] D. D. MacNeil and J. R. Dahn, J. Electrochem. Soc. **148**, A1211 (2001).
[96] C. J. Brown, Acta Crystallogr. **7**, 92 (1954).

[97] *Infotherm Thermophysical Properties Database* (FIZ CHEMIE, Berlin, 2005).
[98] D. R. Lide, *CRC Handbook of Chemistry and Physics* (CRC Press, Cleveland, Ohio, 1977).
[99] G. Ceder and M. K. Aydinol, Solid State Ionics **109**, 151 (1998).
[100] M. S. Whittingham, Chem. Rev. **104**, 4271 (2004).
[101] K. Xu, S. Zhang, J. L. Allen, and T. R. Jow, J. Electrochem. Soc. **149**, A1079 (2002).
[102] M. Wang and A. Navrotsky, Solid State Ionics **166**, 167 (2005).
[103] K. K. Lee, W. S. Yoon, K. B. Kim, K. Y. Lee, and S. T. Hong, J. Electrochem. Soc. **148**, A716 (2001).
[104] K. K. Lee, W. S. Yoon, and K. B. Kim, J. Electrochem. Soc. **148**, A1164 (2001).
[105] X. Zhang, A. M. Sastry, and W. Shyy, J. Electrochem. Soc. **155**, A542 (2009).
[106] O. Borodin and G. Smith, in *MRS Spring 2008*, San Francisco, 2008).

Chapter 3

First-principles Studies of Surface Properties for Olivine Structure $LiMPO_4$

In this chapter, we first briefly review previous studies on two aspects of $LiMPO_4$ cathode materials: controlling particle shape and understanding the lithiation/delithiation mechanism. We believe that our first-principles study of $LiMPO_4$ surfaces will be a valuable addition to previous experimental work and provide insights from a different perspective. After explaining our first-principles approach to surface studies, we present the calculated surface properties for $LiFePO_4$ and $LiMnPO_4$, and provide the equilibrium particle morphologies under vacuum condition. Our surface studies begin with stoichiometric surfaces. In next chapter, we will extend our studies into non-stoichiometric surfaces and show the dependency of equilibrium particle shape on external chemical conditions. We conclude this chapter by discussing several interesting results in our first-principles investigations and the implications on phase transformation mechanisms and morphology control.

3.1 Introductions

3.1.1 Material transport, morphology control, and phase transformation

Among the four olivine structure $LiMPO_4$ (M = Fe, Mn, Co, and Ni), $LiFePO_4$ has appeared as a promising cathode material for high-power rechargeable lithium-ion batteries, but much of its unusual phase transformation behavior and transport properties

remain to be understood. The orthorhombic olivine structure of $LiFePO_4$ has a space group of P*nma* and is rather anisotropic in many properties. Maxisch et al.[1] calculated the elastic moduli for $LiFePO_4$ and the delithiated $FePO_4$ form of it, and found significant variations along the three orthorhombic directions. Due to the anisotropic nature of the olivine crystal structure, the variation in the transport properties is even more significant. Morgan et al.'s *ab initio* study indicated that while Li^+ mobility is high in the tunnels along the [0 1 0] direction, Li^+ hopping between tunnels is very unlikely.[2] Similar conclusions were reached by Islam et al. using potential models.[3] Recently, transport measurements on single crystalline $LiFePO_4$ have also become available.[4] In the early development of $LiFePO_4$, it was thought that the material's charge/discharge rate was limited by electronic transport, leading to the development of doping [5] and carbon coating techniques [6-8] to improve the apparently low electronic conductivity of the material. It has also been suggested that the transport limitations can be overcome by using small particles.[6, 9] In 2006, fairly good electrochemical performance has been achieved without the use of carbon coating by reducing particle size to about 140 nm.[10] Recently, through innovative size-reducing and surface coating, the material performance has almost approached its theoretical limit even at extremely high charging/discharging rate.[11]

The proven success in size control has stimulated continuing efforts to synthesize nano-$LiMPO_4$ particles.[12-16] However, given the anisotropic nature of the material, control of particle *shape* may be as important as average *size* control. This has activated research in new synthesis routes for $LiFePO_4$. Starting with the pioneering work of Whittingham's group[17, 18] and more recently work by other research groups[19-22], well crystallized particles of $LiFePO_4$ can be formed via a hydrothermal approach. More

interestingly, several studies reported platelet shape $LiFePO_4$ crystals in the hydrothermal synthesis.[17, 23] Electron microscopy studies by Richardson et al.[24] showed that the large facet of the plate-like crystals is the (0 1 0) surface. Given the one-dimensional Li diffusion path along the [0 1 0] direction, Richardson et al.[24] further suggested that the use of thin, unagglomerated particles with large (010) surface area would increase the active area and decrease the diffusion distances for Li ions. For a crystal in its thermodynamic equilibrium shape, the relative area of each facet on a particle depends on its surface energy. In the case of plate-type $LiFePO_4$, a preference of the (0 1 0) facet on the crystal implies that the (0 1 0) surface is thermodynamically favored over other facets. To effectively control the particle morphology, it is crucial to know the equilibrium particle morphology.

$LiMnPO_4$, another important cathode material of the $LiMPO_4$ family, can be an ideal substitute for the commonly used cathode material $LiCoO_2$ due to its equilibrium voltage of 4.1 V, which is compatible with the electrolyte presently used in Li-ion batteries. While it has lower density leading to a lower energy density, its safety, like that of other lithium transition metal phosphate, is probably much better than that of $LiCoO_2$. Unfortunately, its electrochemical performance, even at reasonable current rate, is not good.[13, 25-28] There are still debates on why $LiMnPO_4$ has a poor electrochemical performance. Various possible explanations, such as, the lack of existence of a pure fully-delithiated phase $MnPO_4$ in the olivine structure,[29] the intrinsically low electronic conductivity,[26] the slow lithium diffusion kinetics within $MnPO_4$,[30] and the large coherent strain between $LiMnPO_4$ and $MnPO_4$,[31] have been proposed. The most effective experimental approach reported in previous literature is still the use of small $LiMnPO_4$

particles to improve its rate performance.[26, 27, 30] However, following the same anisotropic transport argument as for $LiFePO_4$, morphology control with the objective of reducing particle thickness in the [010] direction and maximizing the active (010) surface area can be more effective to improve the electrochemical performance of $LiMnPO_4$. Thus, a plate-type particle shape with reduced thickness in [010] direction can be more beneficial than a spherical particle of the same volume. At present, experimental or computed data on the surface energetics and equilibrium particle morphology of $LiMnPO_4$ are not available.

On the other hand, the electrochemical performance enhancement for nano-scale $LiFePO_4$ has raised discussions about whether there is any fundamental change to the material at the nano-size region.[32, 33] We believe that surfaces can be important for the perturbation that they may cause in the voltage curve.[34] While for bulk materials the surface effect on the charge/discharge thermodynamics is negligible; for nano-particles, the region influenced by the surface may become a significant fraction of the total amount of Li sites due to the increasing surface-to-volume ratio. Any variations in the surface Li redox potentials will lead to inhomogeneous delithiation/lithiation of nano-scale $LiFePO_4$ particles: if in certain crystal orientation the surface voltage is lower than the bulk value, a region extending from that surface will be delithiated while the bulk is not. While the extend of this region is currently not known, one can expect it to be several layers due to the phase separating nature of $LiFePO_4$ and $FePO_4$.[35] Similarly, the surfaces with potential above that of bulk $LiFePO_4$ will create a lithiated region extending from these surfaces even when the bulk of the material is delithiated. Interestingly, Laffont et al.'s recent findings [36] on Li insertion/extraction from plate-type nano-$LiFePO_4$

with a large (010) surface area are consistent with our model. They found that the $LiFePO_4$-to-$FePO_4$ phase transition initially occurs at the center region on the (010) plane of the plate-type particle, and the $FePO_4$-to-$LiFePO_4$ conversion first take place at the peripheral region of the particle. This inhomogeneous Li insertion/extraction for the well faceted nano-$LiFePO_4$ is unexpected and is inconsistent with the core-shell model of delithiation, which assumes isotropic kinetic transformation behavior within a single $LiFePO_4$ particle.[37] Up to now, it is not clear whether this phase transformation behavior is universally true for all phosphates.

3.1.2 Proposed surface studies for olivine $LiMPO_4$

In the previous subsection, we have discussed recent experimental efforts of $LiMPO_4$ on two interesting topics: particle morphology control and the unusual lithiation/delithiation at nano size region. We believe that first-principles surface investigations for the olivine structure $LiMPO_4$ can be insightful to explain some of the ambiguities left by experimental studies. We are interested in several surface properties of $LiMPO_4$: surface structures, surface energies, and surface redox potentials. Our studies start from stoichiometric $LiMPO_4$ surfaces. Once surface energies are calculated, the thermodynamic equilibrium shape of a crystal can be determined through a Wulff construction, which is a minimization of the total surface energy subject to fixed total volume.[38] For the thermodynamically stable facets in the Wulff shape, we further calculate their surface redox potentials as the average energy (per formula unit of Li) to extract (insert) Li from (into) the outermost layer of a given surface. The calculated surface redox potentials will clarify if there is any thermodynamic difference between

surface layers and bulk region, and thus provide reasonable explanations of the electrochemical performance difference between nano-scale and bulk $LiMPO_4$ reported in literature.[31, 36] Furthermore, any anisotropy in the calculated surface redox potentials will indicate that Li extraction/insertion may occur in a non-trivial manner. By comparing the calculated surface potentials between $LiFePO_4$ and $LiMnPO_4$, we can conclude if the anisotropic phase transformation behavior for $LiFePO_4$ is general to different olivine structure cathode materials.

3.2 Surface and morphology studies from first-principles

3.2.1 Existing theories of predicting particle morphology

1) Wulff construction

The first method of predicting equilibrium particle shape of a crystal is documented in the seminal *The Collected Works of J. W. Gibbs*.[39] For a crystal in equilibrium with its surroundings, the total surface energy must be minimal at a given volume. A polar plot of the surface energy can be constructed by drawing along each crystallographic orientation $\boldsymbol{n}$ a vector, whose norm equals the surface energy in this direction. A plane perpendicular to each vector is then drawn passing through the endpoint of the vector. The inner envelope of all these planes forms a Wulff construction and only planes that are part of the Wulff shape are thermodynamically stable. Wulff shape can be generated by optimizing the half-plane intersections for all crystal facets through a linear programming approach.[40] In this thesis, Wulff shapes are generated using *Qhull*, which implements "Quickhull" algorithm for a fast generation of convex hull.[41]

2) Growth morphology

Another method of simulating crystal morphology is based on Hartman-Perdok theory,[42] which attempts to consider the kinetic factors for crystal growth by using the attachment energy for each crystal plane, rather than the surface energy. The attachment energy is defined as the energy released on a per formula unit basis when a new slice of depth d_{hkl} is attached to the crystal face. The attachment energy can be expressed as

$$E_{attach} = \frac{E_{crystal} - E_{slice}}{n} \tag{3-1}$$

where $E_{crystal}$ is the energy of the crystal, E_{slice} refers to the energy of the crystal slice in the [*hkl*] direction, and n is the number of formula units per slice.

It is assumed that the growth rate is proportional to the attachment energy from a layer-by-layer growth mechanism. Therefore, surfaces with smaller attachment energies in magnitude will have slower growth rates and be more likely to dominate the final morphology. A crystal morphology derived from this method is called the "growth" morphology.

The investigations of crystal "growth" morphology are commonly seen in literatures where electrostatic point-charge models were used to evaluate total energies of inorganic crystals. The number of formula units per slice is relatively easy to define in those potential models as one can choose the distance threshold in the energy evaluation for crystal slice. For slab models (details explained in next subsection) used in DFT calculations, it is difficult to separate a slice layer from any bulk component that it may accidentally include. Hence, one can mistakenly decrease the magnitude of calculated attachment energy simply because of including too many atomic layers in the slice layer. In this thesis, we do not study the "growth" morphology for $LiMPO_4$.

3) Lattice spacing method

The so-called Bravais-Friedel-Donnay-Harker (BFDH) approach is in name of the authors who develop this method to predict crystal morphology.[43, 44] It is purely a geometrical calculation that uses crystal lattice and symmetry to generate a list of possible growth faces and their relative growth rates. The growth rate of a facet is inversely proportional to its interplanar spacing. It does not account for any energetics of the system.

3.2.2 Formalism of surface energy

First-principles investigations of surfaces and the calculations of surface energies are well-established for metal oxides.[45-49] In this subsection, we will derive the formula used to evaluate surface energy from first-principles calculations. For stoichiometric surface, its definition of surface energy is trivial and can be considered as a special case of non-stoichiometric surfaces. Therefore, we will provide the general thermodynamic formulism for non-stoichiometric surfaces here.

The thermodynamic quantity of interest to describe equilibrium between a surface and its environment is the surface grand potential φ, which is the Legendre transform of the surface energy with respect to the number of particles n_x of species x.

$$\varphi = \frac{G(T, p, n_x) - \sum_x n_x \mu_x(T, p_x)}{S} \tag{3-2}$$

where T and p are the temperature and pressure, G is the Gibbs free energy of the solid exposing the surface of interest, S is the total surface area, n_x are the number of particles x in the solid, and μ_x and p_x are the chemical potentials and the partial pressures of the

particles in the external reservoirs (solution or gas phase). For the sake of clarity, we first provide the standard formalism for the thermodynamic equilibrium between surfaces of binary oxides M_xO_y and an external environment. The generalization to $LiFePO_4$ is provided later.

For surfaces of binary oxides M_xO_y and external adsorbate *ad*, the chemical potentials of three different species need to be considered: M, O, and *ad*. If the M and O particle reservoirs are in thermal equilibrium with bulk M_xO_y phase that surfaces of interest grow from (If this were not the case, the bulk phase would either grow or decompose), the chemical potentials of M and O satisfy,

$$G_{MxOy} = x\,\mu_M + y\,\mu_O \tag{3-3i}$$

where G_{MxOy} is the total energy of a bulk M_xO_y unit. Hence, there are only two independent chemical potentials, and eliminating μ_M from the equation for the surface grand potential yields the following expression for φ:

$$\varphi = \frac{G(\{n_x\}) - \frac{n_M}{x} G_{MxOy} + \left(\frac{n_M y}{x} - n_O\right)\mu_O - n_{ad}\mu_{ad}}{2S} \tag{3-3ii}$$

Neglecting the vibrational entropy contributions and finite temperature enthalpy changes in the solid state, we can approximate the Gibbs free energy $G(T,p,n_x)$ by the total energies (e.g. $E(\{n_x\})$ and E_{MxOy}) calculated by density functional theory. The accuracy of this approximation was carefully investigated by Reuter et al. [50]. For a given environment (as expressed by the external chemical potentials), the surface structure with lowest grand potential is the thermodynamically stable ground-state structure. The above formalism has been extensively used in literatures to study non-stoichiometric surfaces,

e.g. Fe_2O_3 [51], Al_2O_3 [48], RuO_2 [50], V_xO_y grown on Pd surface [52], and H_2-H_2S/MoS_2 gas-solid interface [53].

Following the thermodynamic formalism described above, we can express the surface grand potential for non-stoichiometric $LiFePO_4$ surface as,

$$\gamma = \frac{E_{slab} - n_{Li}\mu_{Li} - n_{Fe}\mu_{Fe} - n_P\mu_P - n_O\mu_O - n_{ad}\mu_{ad}}{2S} \quad (3\text{-}4i)$$

where E_{slab} is the total energy of the non-stoichiometric slab. $\mu_{Li}, \mu_{Fe}, \mu_P, \mu_O$, and μ_{ad} are the chemical potentials for Li, Fe, P, O, and adsorbates (excluding external oxygen adsorbate), respectively. n_{Li}, n_{Fe}, n_P, n_O, and n_{ad} are the atomic numbers.

Note that the chemical potentials for all atomic species are not completely independent because of equilibrium between bulk $LiFePO_4$ (α) and particle reservoirs,

$$E_\alpha = \mu_{Li} + \mu_{Fe} + \mu_P + 4\,\mu_O \quad (3\text{-}4ii)$$

where E_α is the total energy of bulk $LiFePO_4$. Substituting equation (3-4ii), we can rewrite equation (3-4i) as,

$$\begin{aligned}\gamma &= \frac{E_{slab} - n_{Li}\mu_{Li} - n_{Fe}(E_\alpha - \mu_{Li} - \mu_P - 4\mu_O) - n_P\mu_P - n_O\mu_O - n_{ad}\mu_{ad}}{2S} \\ &= \frac{E_{slab} - n_{Fe}E_\alpha - (n_{Li} - n_{Fe})\mu_{Li} - (n_P - n_{Fe})\mu_P - (n_O - 4n_{Fe})\mu_O - n_{ad}\mu_{ad}}{2S}\end{aligned} \quad (3\text{-}4iii)$$

The fourth term in the numerator above is zero if we only consider non-stoichoimetry of Li and O in the surface layer ($n_P = n_{Fe}$). Using the dummy substitution,

$$n_{Fe} = n_{Li} + (n_{Fe} - n_{Li}) \quad (3\text{-}4iv)$$

equation (3-4iii) can further be rewritten as,

$$\gamma = \frac{E_{slab} - n_{Li}E_\alpha - (n_{Fe} - n_{Li})E_\alpha + (n_{Fe} - n_{Li})\mu_{Li} - (n_O - 4n_{Fe})\mu_O - n_{ad}\mu_{ad}}{2S} \quad (3\text{-}4v)$$

For the phase equilibrium between bulk $LiFePO_4$ (α) and $FePO_4$ (β), there is a critical Li chemical potential,

$$E_\alpha = E_\beta + \mu_{Li}^{\,b} \tag{3-4vi}$$

Using equation (3-4vi), we can rewrite (3-4i) as,

$$\gamma = \frac{E_{slab} - n_{Li}E_\alpha - (n_{Fe} - n_{Li})\left[E_\beta - (\mu_{Li} - \mu_{Li}^b)\right] - (n_O - 4n_{Fe})\mu_O - n_{ad}\mu_{ad}}{2S} \tag{3-4vii}$$

From equation (3-4vii), we can see that the surface grand potential for non-stoichiometric $LiFePO_4$ surfaces is a function of **three** independent variables, μ_{Li}, μ_O, and μ_{ad}. In next chapter, we consider four types of surface adsorbates, H, H_2O, OH, and O, and we convert all their chemical potentials to be linearly dependent on oxygen chemical potential in equation (3-4vii). Therefore, surface grand potential of our interest can be plotted with **two** independent chemical potentials. We further fix the Li chemical potential at the critical value $\mu_{Li}^{\,b}$,

$$\mu_{Li} = \mu_{Li}^{\,b} \tag{3-4viii}$$

Then surface energy of a non-stoichiometric $LiFePO_4$ surface can be evaluated using the following equation,

$$\gamma = \frac{E_{slab} - n_{Li}E_\alpha - (n_{Fe} - n_{Li})E_\beta - (n_O - 4n_{Fe})\mu_O - n_{ad}\mu_{ad}}{2S} \tag{3-4ix}$$

For a stoichiometric surface ($n_{Li} = n_{Fe}$, $n_O = 4n_{Fe}$, $n_{ad} = 0$), equation above reduces to the conventional definition of surface energy,

$$\gamma = \frac{E_{slab} - n_{Li}E_\alpha}{2S} \tag{3-4x}$$

3.2.3 Calculating surface properties in VASP

All total energies in our surface work are calculated using the GGA. The GGA+U approach[54, 55] is used to accurately calculate the surface redox potentials and to guarantee that the excess holes or electrons are properly localized. For calculations of $LiFePO_4$ surfaces, we choose a J value of 1 eV and a U value of 5.3 eV, which is the average of the self-consistently calculated U values for Fe^{2+} (U = 4.7 eV in $LiFePO_4$) and Fe^{3+} (U = 5.9 eV for $FePO_4$).[56] Similarly for $LiMnPO_4$, we choose a U value of 5.5 eV. We found the values of surface energies for $LiFePO_4$ to vary less than 3% as the U value decreases from 5.3 eV to 4.7 eV. We employ the "fully localized" double counting scheme as presented by Liechtenstein et al.[57] Previous GGA+U calculations on $LiFePO_4$ indicate that this U parameter and double counting scheme provide for good agreement with experiment. A ferromagnetic high-spin state is assumed for Fe and Mn ions. The bulk $LiFePO_4$ ($FePO_4$) is paramagnetic at room temperature[58] and the energetic effects of the magnetic ordering are small[59].

To investigate surface properties of olivine structure $LiMPO_4$, we use slab model (see Figure 3-1), in which a set of infinite layers separated by vacuum layers are repeated periodically along the surface normal. Lattice parameters of the supercell (including both slab and vacuum) are fixed and only atoms near the surface (refer to "relaxed layer" in Figure 3-1) are allowed to relax until forces on them are smaller than 0.03 eV/Å. The inner part of the slab (refer to "frozen layer" in Figure 3-1) is frozen at bulk positions to simulate the bulk of this material. The thicknesses of vacuum, slab and free relaxation layer are all varied to obtain a surface energy in the given direction converged to within 5% of the calculated value. These are the necessary convergence tests to be performed for first-principles investigations of surface properties.

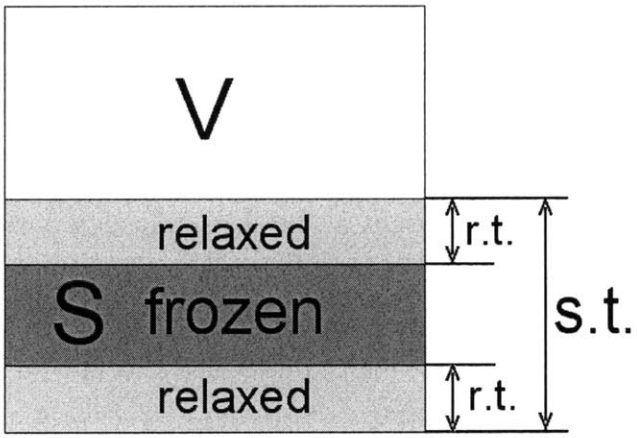

Figure 3-1 Schematic illustration of the slab model used in surface calculation. The top part refers to the vacuum. The bottom part represents the slab with its thickness labeled as "*s.t.*". The two sides (light-grey part) of the slab are the free relaxed layers with the same thickness labeled as "*r.t.*".

3.2.4 Construction of surfaces from bulk

Lattice parameters of the relaxed bulk $LiFePO_4$ structure are a=10.4363 Å, b=6.0491 Å, c=4.7546 Å, in good agreement with experiments.[58] Figure 3-2 shows the crystal structure of bulk $LiFePO_4$ after relaxation. The initial unrelaxed surface structures are carved out of the fully relaxed bulk crystal. In principle, surface with a given Miller index can terminate anywhere along the direction of surface normal. However, in this study we first consider only stoichiometric surfaces for the investigation of surface energies. Under this assumption, the candidate planes for surface terminations are limited. For example, to create a stoichiometric (1 0 0) surface, the possible termination planes are (0.5, y, z) and (0.25, y, z) (expressed in fractional coordinates for the unit cell setting in Figure 3-2).

Other terminations in this orientation will create either a non-stoichiometric surface, or a surface that is equivalent to any of the two mentioned above.

For atoms that lie on the cutting plane, the following principles have been additionally adopted:

(1) The PO_4 tetrahedron is always preserved if the surface termination cuts through it, and a corrugated surface may be created. As shown in Figure 3-2a, the tentative termination plane (0.5, *y*, *z*) for the (1 0 0) surface would cut through the highly covalent P-O bonds and create a surface with the under-coordinated P being exposed on top of the surface. Our calculations suggest that such a surface has a very high surface energy. Thus, in practice a neighboring Fe atom is left under-coordinated in order to keep the PO_4 tetrahedron intact.

(2) For an ionic or partially ionic crystal, it is known that a charged surface with a perpendicular dipole moment will induce a polarizing electric field throughout the crystal, resulting in a very large surface energy.[60] Hence, all the surfaces studied in this work are "Type II" or "Type III" surfaces according to the well-known classification by Tasker [60], with a vanishing dipole in the direction of the surface normal.

(3) The ion coordination loss at the surface should be minimized. This rule is practically useful as various stoichiometric surface configurations can be created at the termination plane. The stable surfaces are expected to have low ion coordination loss.

The candidate planes for surface terminations can also be narrowed down by applying the third rule described above. For example, for the (0 1 0) surface, the cut at plane (*x*, 0.5,

z) in Figure 3-2b would have 2 Fe-O bonds and 3 Li-O bonds cut per $a \times c$ unit surface area. However, if the surface terminates at plane (x, 0.25, z) in Figure 3-2b, the coordination number loss would further increase to 5 Fe-O bonds and 3 Li-O bonds on the same surface area. Thus, a surface terminating at plane (x, 0.5, z) is expected to give a lower surface energy than the one at plane (x, 0.25, z). For several orientations it is not possible to predetermine which of the different surface configurations will be lower in energy. For example, surface (1 0 0) has one Fe-O bond and three Li-O bonds (per surface area of $b \times c$) broken if cut at plane (0.5, y, z) in Figure 3-2a. Conversely, it would have three broken Fe-O bonds and no broken Li-O bond on the same surface area if cleaving at plane (0.25, y, z) in Figure 3-2a. Therefore, multiple termination possibilities are calculated for those directions where possible.

For each possible surface termination, the surface is then simulated using the slab technique as we discussed in the previous section. We have chosen our slabs such that the two sides of it are symmetrically equivalent and can be mapped into each other by an inversion, mirror or glide type of symmetry operation in the middle of the slab. This is possible for $LiFePO_4$ due to the particular space group of $P2_1/n\ 2_1/m\ 2_1/a$ (the full convention). In the olivine crystal structure, positions with inversion symmetry are 4*a* sites ((0, 0, 0), (0.5, 0, 0.5), (0, 0.5, 0), (0.5, 0.5, 0.5)) and 4*b* sites ((0, 0, 0.5), (0.5, 0, 0), (0, 0.5, 0.5), (0.5, 0.5, 0)). Moreover, there are mirror and glide symmetries perpendicular to the three principal axes of the orthorhombic unit cell. In Ref.46 and Ref.61-69 [46, 61-69], where the slab model is employed to investigate surface properties with *ab initio* methods, readers can find more examples of using symmetry of underlying crystal structure to

ensure that the stoichometric surfaces on each side of the slab give the same structure configuration and energy.

3.3 Stoichiometric $LiMPO_4$ surfaces

3.3.1 Calculated surface energies

A. $LiFePO_4$

The calculated surface energies for seven low-index surfaces of $LiFePO_4$ are summarized in Table 3-1. Among the seven low-index orientations, surface (0 1 0), (1 0 0) and (1 0 1) have the lowest energies. While it is not practical to study all high-index surfaces, several surfaces that potentially have low energies are studied in this work. Based on the calculated surface energies in low-index orientations and noting that surface (1 0 1) has the lowest energy among the non-principal directions, we also investigated the (2 0 1) and (3 0 1) surfaces, which are indeed calculated to be low energy surfaces. Although one can argue that other high-index surfaces may influence the thermodynamic stability of the nine surfaces studied here, as we discuss later, the crystal morphology is not significantly modified by including more high-index surfaces.

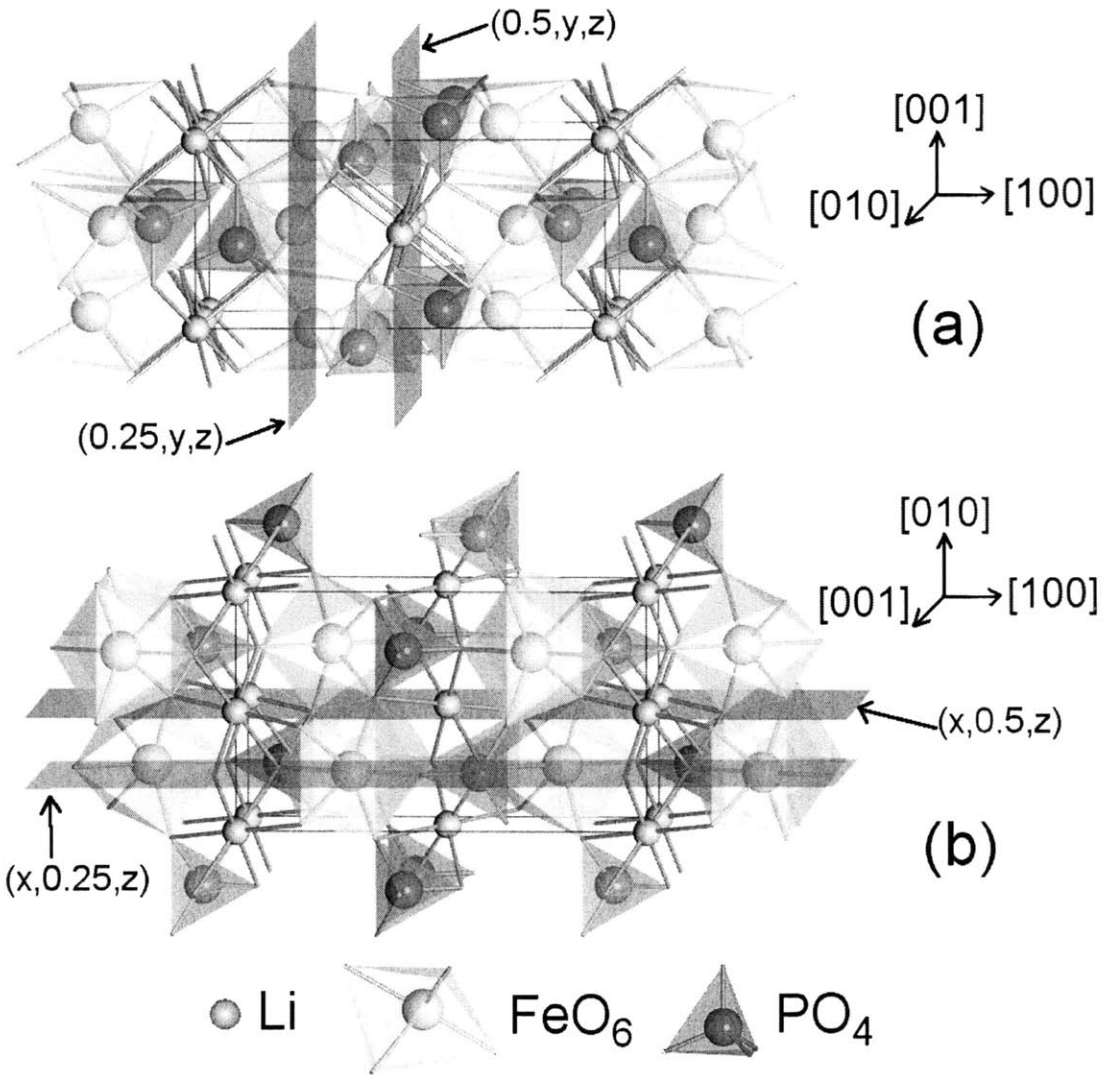

Figure 3-2 Relaxed crystal structure of bulk $LiFePO_4$ and possible planes for surface terminations in two orientations. Panel (a) shows for the (1 0 0) surface the two possible cuts containing points (0.25, *y*, *z*) and (0.5, *y*, *z*), respectively. Panel (b) shows for the (0 1 0) surface the two termination planes (*x*, 0.25, *z*) and (*x*, 0.5, *z*), respectively.

Table 3-1 Calculated surface energies γ (in unit of J/m^2) of $LiMPO_4$ in fifteen directions and surface redox potentials Φ (in unit of V) of $LiMPO_4$ in six directions.

Directions	(100)	(010)	(001)	(011)	(101)	(110)	(111)	(012)	(021)	(102)	(201)	(120)	(210)	(301)	(401)
γ of $LiMnPO_4$	0.66	0.67	1.04	0.67	0.65	1.36	0.81	1.20	0.88	1.11	0.55	1.01	0.87	0.67	1.23
Φ of $LiMnPO_4$	4.18	3.20		4.09	3.70						3.86		3.76		
γ of $LiFePO_4$	0.66	0.64	0.97	0.76	0.62	1.30	0.85				0.52			0.62	1.15
Φ of $LiFePO_4$	3.84	2.95		3.79	3.25						3.76				

B. $LiMnPO_4$

We also investigate surface energies for $LiMnPO_4$ in thirteen low-index directions with components of the Miller index lower than two, plus two high-index directions. For each orientation, different surface terminations are considered and only the lowest value of surface energy is reported here. As summarized in Table 3-1, the calculated surface energies are in the range of 0.55 J/m^2 to 1.36 J/m^2. The relative low energy surfaces are (100), (010), (011), (101), (201), and (301). However, the values of surface energies in these six directions are not significantly different from each other.

3.3.2 Calculated surface structures

To investigate how surface energy relates to surface structure, we will show the relaxed surface structures of $LiFePO_4$ in this section and provide the displacements of under-coordinated ions on the surfaces. Energetics for high energy terminations in each crystal orientation are also provided. We do not present the relaxed surface structures of $LiMnPO_4$ as they are quite similar to those for $LiFePO_4$.

A. The (1 0 0) surface

We find that the low energy cut in this direction terminates at point (0, 0, 0) (a plane symmetrically equivalent to plane (0.5, *y*, *z*) in Figure 3-2a). A slab of 11.3 Å with a relaxation layer of 3.9 Å is sufficient to get a converged surface energy. The surface termination cuts through the LiO_6 octahedra and one vertex of the PO_4 tetrahedra. As

mentioned in the methodology section, we keep the PO_4 tetrahedra intact because of the strong covalent P-O bonds, consequently, the nearby FeO_6 octahedra are cut instead. In the original unrelaxed structure, the $Li_{(1)}$ on the surface are 3-fold coordinated by oxygen, and 5-fold coordinated $Fe_{(1)}$ are buried farther below the surface. The relaxed structure is shown in Figure 3-3 and the detailed relaxations are provided in Table 3-X at the end of this chapter. Note that while the displacements given here are absolute values, they can also be considered relative to the bulk, as the unit cell does not move as a whole because the atoms 3 Å below the surface undergo only minor displacements. The $Li_{(1)}$ atom relaxes most. It is originally coordinated with $O_{(1)}$, $O_{(2)}$ and $O_{(3)}$ (see Figure 3-3) but relaxes toward the two-fold "bridging" $O'_{(1)}$ atom in the neighboring row of O atoms, and looses its bonding with $O_{(3)}$. The distance between $Li_{(1)}$ and $O'_{(1)}$ is about 2.9 Å, which is much larger than the average bond length of 1.85 Å for $Li_{(1)}$-$O_{(1)}$ and $Li_{(1)}$-$O_{(2)}$ bonds on the surface. Therefore, we consider the $Li_{(1)}$ to be 2-fold coordinated after the relaxations. The 5-fold $Fe_{(1)}$ lies well beneath the surface and its relaxation is negligibly small. We also studied another possible surface cut in the (1 0 0) direction which terminates at point (0.25, 0, 0) (see plane (0.25, *y*, *z*) in Figure 3-2a). This surface cut leaves the 3-fold coordinated Fe atoms directly exposed on the surface, and is calculated to have a somewhat higher surface energy of 0.73 J/m^2.

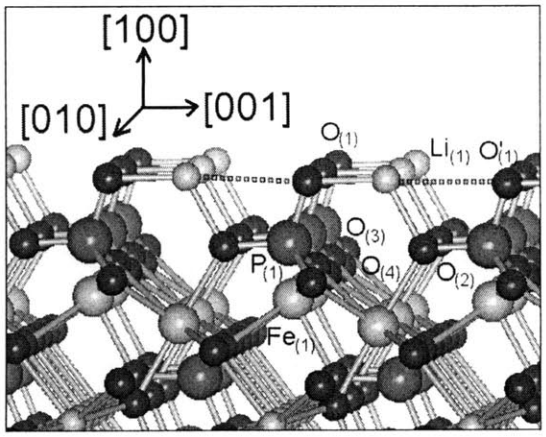

Figure 3-3 The relaxed surface structure of (1 0 0) surface. Color setting for the Li, Fe, and P atoms is the same as in Figure 3-2. Oxygen atoms are shown as red. The under-coordinated ions are labeled. The dotted lines mean that the two atoms, $Li_{(1)}$ and $O'_{(1)}$, are probably not bonded because of the large distance between them.

B. The (0 1 0) surface

The low energy surface is found to terminate at point (0, 0, 0) (a plane equivalent to plane (x, 0.5, z) in Figure 3-2b) with a surface energy calculated to be 0.64 J/m^2, compared with the much higher value of 1.21 J/m^2 if the surface is terminated at point (0, 0.25, 0) (see plane (x, 0.25, z) in Figure 3-2b). A slab of 12.1 Å with a relaxation layer of 3.3 Å is sufficient to get a converged surface energy for the low energy termination. The low energy termination in this direction cuts through the LiO_6 octahedra but only cuts the top of the FeO_6 octahedra, leaving 3-fold Li and 5-fold Fe exposed on the surface. The relaxed structure of the low energy termination is shown in Figure 3-4 and the relaxations are provided in Table 3-X. The 3-fold $Li_{(1)}$ is drawn toward one of three

nearest-neighbor oxygen atom $O_{(1)}$ so that the length of the $Li_{(1)}$-$O_{(1)}$ bond decreases from 2.227 Å to 2.027 Å after the relaxations. The length of the bond between the 5-fold $Fe_{(1)}$ and 2-fold $O_{(2)}$ drops from 2.274 Å to 2.076 Å because of the displacement of $O_{(2)}$ in the direction of [-1 0 0]. The distance between the 5-fold $Fe_{(2)}$ and 3-fold $O_{(1)}$ is also reduced from 2.276 Å to 2.100 Å because of the displacement of $Fe_{(2)}$ in the direction of [0 0 1].

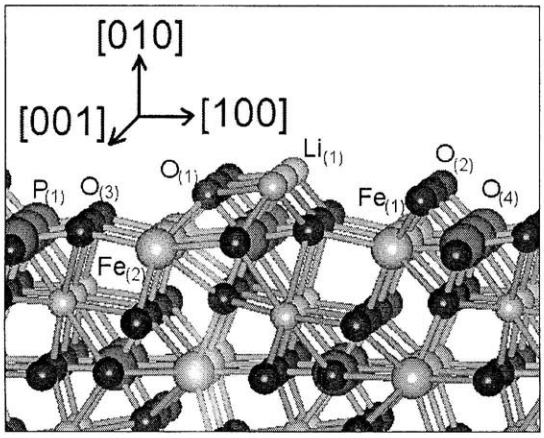

Figure 3-4 The relaxed surface structure of (0 1 0) surface.

C. The (0 0 1) surface

In this direction, the low energy surface cut is found to terminate at point (0, 0, 0) and the surface energy is calculated to be 0.97 J/m^2. Another possible cut terminates at point (0, 0, 0.25) but results in a slightly higher surface energy of 1.02 J/m^2. For the low energy termination, the relaxed structure is shown in Figure 3-5 and the relaxations are given in the Table 3-X. A slab of 11.8 Å with a relaxation layer of 3.0 Å is used. The low energy termination cuts through the centers of FeO_6 octahedra and LiO_6 tetrahedra, so 3-fold $Fe_{(1)}$

and 3-fold $Li_{(1)}$ are exposed on the surface. The surface would also cut through the caps of the PO_4 tetrahedra, however, the $P_{(1)}$ tetrahedron is preserved by leaving the Fe and Li atoms in the layer immediately beneath under-coordinated. Therefore, the $Fe_{(2)}$, $Li_{(2)}$ and $Li_{(3)}$ are all 5-fold coordinated. The $P_{(1)}$-$O_{(1)}$ bond sticks out in the direction of surface normal. Numbers for the (0 0 1) surface in Table 3-X suggest that the dominating relaxations are the inward displacements of the $Li_{(1)}$ and $Fe_{(1)}$.

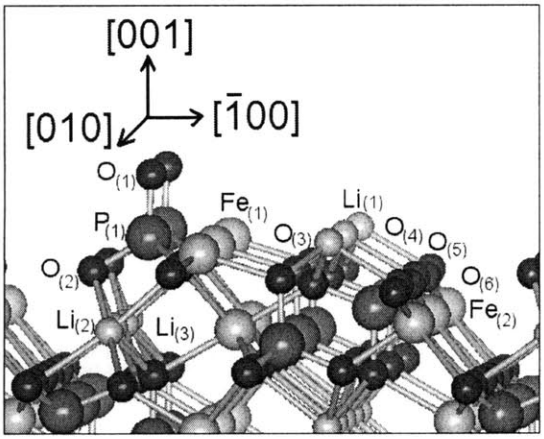

Figure 3-5 The relaxed surface structure of (0 0 1) surface.

D. The (0 1 1) surface

The low energy surface cut is found to terminate at point (0, 0, 0) with a calculated surface energy of 0.76 J/m^2. A slab of 7.5 Å with a relaxation layer of 2.5 Å is sufficient. Another possible cut terminates at point (0, 0.5, 0) but provides a much higher surface energy of 1.50 J/m^2. For the low energy termination, the relaxed structure is shown in Figure 3-6 and the relaxations are given in the Table 3-X. We can see that the surface cut

runs through the centers of FeO_6 tetrahedra and LiO_6 tetrahedra leaving the $Fe_{(1)}$ and $Fe_{(2)}$ 4-fold coordinated and the $Li_{(1)}$ 3-fold coordinated on the surface. The surface plane also cuts a cap of another LiO_6 tetrahedron which is not on the outermost surface, so $Li_{(2)}$ and $Li_{(3)}$ are left 5-fold coordinated near the top surface. Numbers for the (0 1 1) surface in the Table 3-X suggest that the 3-fold $Li_{(1)}$ undergoes a substantial displacement in the [1 0 0] direction. The distances between $Li_{(1)}$ and the nearest-neighbor Fe atoms, $Fe_{(1)}$ and $Fe_{(2)}$, are increased from 3.548 Å and 3.310 Å, to 4.431 Å and 5.214 Å, respectively. These increased separations between under-coordinated Li and Fe may be because the electrostatic repulsion between them is less effectively screened on the surface. There are substantial inward displacements for the 3-fold $Fe_{(1)}$ and $Fe_{(2)}$. For the 5-fold $Li_{(2)}$, the displacement along the direction of [-1 0 0] increases the distance between $Li_{(2)}$ and $O_{(7)}$ from 2.228 Å to 2.617 Å. Therefore, we consider that the $Li_{(2)}$ is not bonded with $O_{(7)}$ any more after the relaxations and effectively becomes 4-fold coordinated.

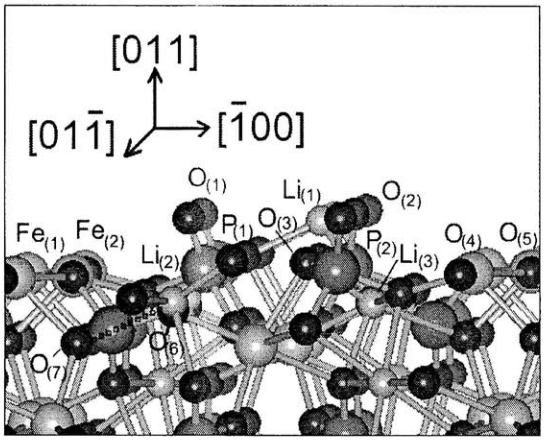

Figure 3-6 The relaxed surface structure of (0 1 1) surface.

E. The (1 0 1) surface

We find that the low energy cut for the (1 0 1) surface terminates at the point (0, 0, 0) with a calculated surface energy of 0.62 J/m^2. A slab of 9.7 Å with a relaxation layer of 2.6 Å is sufficient. Another cut terminates at point (0, 0, 0.5) but provides a much higher energy of 1.35 J/m^2. The relaxed structure of the low energy termination is shown in Figure 3-7 and the relaxations are given in Table 3-X. The surface cuts through the Fe and Li octahedra, and leaves 3-fold $Li_{(1)}$ and $Li_{(2)}$ together with 5-fold $Fe_{(1)}$ and 4-fold $Fe_{(2)}$ on the surface. The dominating relaxations are the inward displacements of the 3-fold $Li_{(1)}$, $Li_{(2)}$, and the 4-fold $Fe_{(2)}$. The 5-fold $Fe_{(1)}$ undergoes minor relaxations compared to other under-coordinated atoms on the surface.

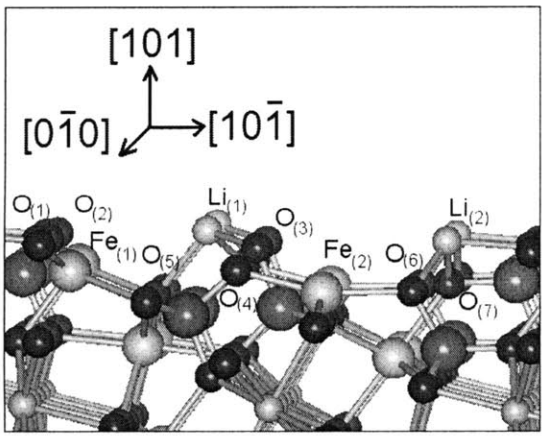

Figure 3-7 The relaxed surface structure of (1 0 1) surface.

F. The (1 1 0) surface

There are two possible cutting options for the (1 1 0) surface: one terminates at point (0, 0, 0) and the other terminates at point (0.5, 0, 0). Note that there is mirror symmetry located at (x, 1/4, z), and n glide symmetry perpendicular to the a axis located at (1/4, y, z). Points (x, 1-x, z) are therefore symmetrically equivalent to points (x, x-1/2, z) through mirror symmetry, and further equivalent to points (1/2-x, x, z+1/2) through the n glide symmetry. Hence, the two cuts actually provide the same surface structure. A slab of 10.5 Å with a relaxation layer of 3.2 Å is used. The relaxed structure of (1 1 0) surface is shown in Figure 3-8 and the relaxations are given in Table 3-X. The most significant relaxation is the displacement of 4-fold $Li_{(1)}$ in the [1 -1 0] direction. The distance between $Li_{(1)}$ and $Fe_{(1)}$ is increased from 3.309 Å to 5.068 Å after relaxation. This is again because of the strong electrostatic repulsion between $Li_{(1)}$ and $Fe_{(1)}$.

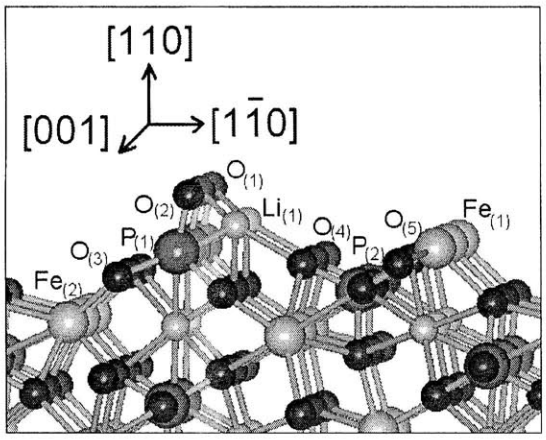

Figure 3-8 The relaxed surface structure of (1 1 0) surface.

G. The (1 1 1) surface

There are two types of cuts for the (1 1 1) surface, one terminates at point (0, 0, 0) and the other terminates at point (0.5, 0, 0). While the former termination cuts right through the centers of PO_4 tetrahedra and creates a rather corrugated surface in order to preserve the PO_4 tetrahedra, the latter termination cuts right through centers of the LiO_6 and FeO_6 octahedra and creates a relatively flat surface. The surface energies are calculated to be 0.91 J/m^2 for the former termination and 0.85 J/m^2 for the latter one. The low energy cut is shown in Figure 3-9 and the relaxations are given in Table 3-X. A slab of 11.5 Å with a relaxation layer of 3.2 Å is used. Most atoms on the surface undergo inward displacements except for the $P_{(1)}$ atom.

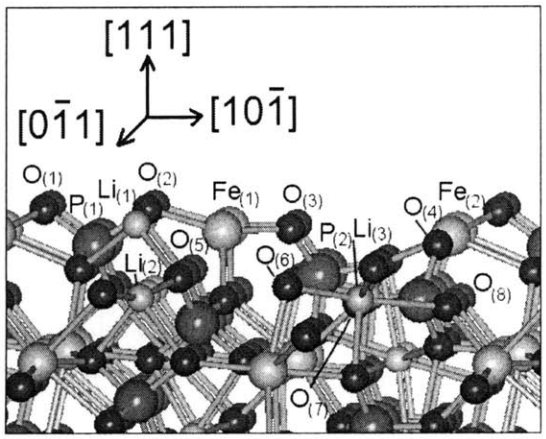

Figure 3-9 The relaxed surface structure of (1 1 1) surface.

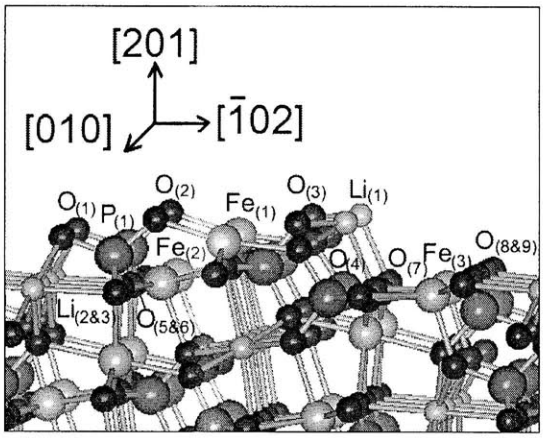

Figure 3-10 The relaxed surface structure of (2 0 1) surface.

H. The (2 0 1) surface

We find that the low energy cut for the (2 0 1) surface terminates at the point (0, 0, 0) (also across the symmetrically equivalent point (0.5, 0, 0)) with a calculated surface energy of 0.52 J/m^2. This is the lowest value of the surface energies we found. To obtain a converged number, a slab of 10.9 Å with a relaxation layer of 3.2 Å is used. Another possible cut terminates at point (0, 0, 0.5) (also across point (0.5, 0, 0.5)) but results in more coordination loss on the surface, and provides a higher surface energy of 1.17 J/m^2. The relaxed structure for the former termination is shown in Figure 3-10 and the relaxations are given in Table 3-X. This surface cut leaves 3-fold $Li_{(1)}$, 4-fold $Fe_{(1)}$, 5-fold $Fe_{(2)}$ and $Fe_{(3)}$ exposed on the surface. The 3-fold $Li_{(1)}$ is drawn toward $O_{(3)}$ and $O_{(4)}$ in the direction of [1 0 -2]. $Li_{(2)}$ and $Li_{(3)}$ also move in the direction of [1 0 -2], resulting in an increase of the mean distance for $Li_{(2)}$-$O_{(5)}$ and $Li_{(3)}$-$O_{(6)}$ from 2.23 Å to 2.33 Å, which is somewhat larger than the average Li-O bond length of 2.13 Å on this surface.

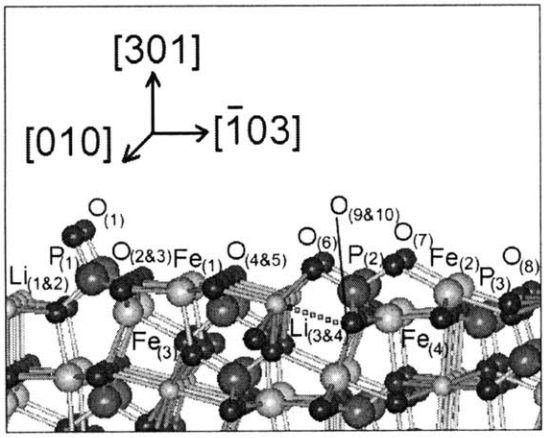

Figure 3-11 The relaxed surface structure of (3 0 1) surface.

I. The (3 0 1) surface

The low energy cut is found to terminate at point (0.5, 0, 0) (also across the symmetrically equivalent point (0, 0, 0.5)). We find that in the unit cell we have chosen (with a surface area of about 107 $Å^2$), 5 Fe-O bonds and 6 Li-O bonds are influenced by this termination. Another possible cut terminates at point (0, 0, 0) (also across point (0.5, 0, 0.5)) but creates a higher coordination number loss, that is, 9 Fe-O bonds and 6 Li-O bonds are affected on the same surface area. We expect the latter termination to give higher surface energy considering the high coordination number loss for Fe on that surface. For the low energy cut, a slab of 10.3 Å with a relaxation layer of 3.8 Å is used. The relaxed structure is shown in Figure 3-11 and the relaxations are given in Table 3-X. The surface cut is rather flat except for one PO_4 tetrahedron sticking out from the surface. There are three 5-fold Fe and one 4-fold Fe exposed on the surface. The termination also

creates 4-fold $Li_{(1)}$ and $Li_{(2)}$ together with 5-fold $Li_{(3)}$ and $Li_{(4)}$. We find that the $P_{(1)}$-$O_{(1)}$ bond is tilted in the direction of [1 0 -3]. Similar to the surface (2 0 1), both $Li_{(3)}$ and $Li_{(4)}$ undergo displacements in the directions of [1 0 -3]. The average distance between $Li_{(3)}$ (or $Li_{(4)}$) and $O_{(9)}$ (or $O_{(10)}$ for $Li_{(4)}$) is increased to 2.556 Å, which again is considerably larger than the average bond length of 2.116 Å for the Li-O bonds on this surface. Therefore, we consider the $Li_{(3)}$ and $Li_{(4)}$ to be 4-fold coordinated after relaxation.

3.3.3 Correlation between surface energy and surface structure

Surface energy can be attributed to the energy required to break bonds when a surface is created. In order to better understand how the structure of a surface relates to its energy, we build a simple model to capture the effect of coordination loss on the surface energy. Due to the structure similarity among olivine structure $LiMPO_4$, we use $LiFePO_4$ as a case study here. We express the surface energy in terms of the multiplicities by which various coordinations are created for Fe and Li after surface termination and relaxation,

$$\Delta E = \sum_{i=3}^{5} m_i \cdot f_i + \sum_{j=2}^{5} n_j \cdot l_j = A \cdot X \qquad (3\text{-}5)$$

f_i (or l_j) in equation (3-5) specifies the energy difference between i-fold Fe (or j-fold Li) and 6-fold Fe (or Li) in the bulk, in eV per formula unit. Labels m_i (or n_j) are the numbers of i-fold Fe (or j-fold Li) created per unit area on the surface. Index "i" counts from 3 because the least coordinated Fe on the surface is still bonded with three O atoms. Index "j" starts from 2 because 2-fold Li is found on the relaxed (1 0 0) surface. "A" is the

matrix form of m_i and n_j, and "X" is the array form of f_i and l_j. Table 3-X provides numbers of coordination loss for Fe and Li on various surfaces and Table 3-1 provides surface energies for different orientations. In practice, the coefficients f_i and l_j are found by a least-squares approximate solution X to equation (3-5) obtained through a QR decomposition of matrix A.[70] The resulting energy parameters X are summarized in Table 3-2. We can see that the energy required for the formation of a surface Fe ion approximately scales with the degree of under-coordination. Hence, the more Fe is left under-coordinated the more it will contribute to the increase in surface energy. A very different trend is obtained for Li. The loss of coordination for Li on the surface can actually lower the energy of the system compared to the octahedral Li coordination in the bulk. In fact creation of 5-fold coordinated Li has a very significant negative energy contribution to the surface energy. Only for the 2-fold coordinated Li is the effect on the surface energy positive. As we discuss later, these results for Li may be a reflection of the fact that Li^+ in bulk is more stable in lower coordinated tetrahedral sites than in octahedral sites.

Table 3-2 Contributions of various coordinated Fe (f_i) and Li (l_j) to the surface energy.

f_3	f_4	f_5	l_2	l_3	l_4	l_5
3.80	2.25	1.05	0.14	-0.27	-0.31	-0.52

Using the parameters in Table 3-2, we can evaluate the surface energies again with the fitting equation (3-5). We have compared the surface energies γ' obtained through the fitting model and the values γ directly calculated with our *ab-initio* methods. The relative differences between γ and γ' (defined as $\frac{\gamma'-\gamma}{\gamma}$) are found to be less than 10% except for two surfaces. The energy of the (0 1 1) surface is underestimated by about 10.5% using the fitting model, and the surface energy in the direction of [2 0 1] is overestimated by about 10.4%. Given the computational error of 5% that we estimated in the calculations of surface energies, we believe that the fitting model gives reasonable estimations of the surface energies in various orientations, and it can replicate the energy preferences for most of the surfaces we studied. More importantly, the parameters in Table 3-2 make it possible to estimate the surface energy of other surfaces.

3.3.4 Wulff shapes under vacuum condition

A. $LiFePO_4$

The Wulff shape for $LiFePO_4$ based on the surface energies in Table 3-1 is shown in Figure 3-12. A grey scale scheme is used whereby lighter surfaces indicate lower surface energy. Only five of the nine surfaces that we have studied appear in the constructed Wulff shape. The other four are not stable against combinations of the five low energy facets. High energy surfaces, such as, the (0 0 1) and (1 1 0) surface, are completely replaced with facets of low energy surfaces. Surface (3 0 1) is calculated to be of low

energy but is still not stable with respect to the formation of faceting by (2 0 1) and (1 0 0) surfaces. Generally, the lower in energy a surface is, the more area the facet contributes to the Wulff shape. The two low energy surfaces, the (0 1 0) and (2 0 1) facets, dominate in the equilibrium shape and contribute up to about 85% of the total surface area in Figure 3-12. The Wulff shape is slightly capped by the (1 0 0) surface and truncated by the (1 0 1) surface in the [0 0 1] direction.

A more complete Wulff construction would require energetic information of other high-index surfaces, which are computationally challenging with the DFT methods. However, using the fitted parameters in Table 3-2 and the coordination number loss for a given surface, we can explore the possible existence of low energy surface in other high-index orientations. Among the twelve high-index directions ([0 1 2], [0 1 3], [0 2 1], [0 3 1], [1 0 2], [1 0 3], [1 2 0], [1 3 0], [2 1 0], [3 1 0], [4 0 1], and [5 0 1]) that we further studied, three surfaces are moderately low in energy, with the surface energy estimated to be about 0.71, 0.78, and 0.75 J/m^2, respectively for surface (0 1 3), (1 0 2), and (1 2 0). These high-index surfaces, when additionally included into the Wulff construction, only slightly change the Wulff shape shown in Figure 3-12. A tiny (0 1 3) facet will replace the vertex shared by the facets (0 1 1), (1 0 1) and (-1 0 1), and the (1 2 0) facet is expected to truncate the edge shared by the (0 1 0) and (1 0 0) facets. The total areas of the (0 1 3) and (1 2 0) facets contribute less than 6% of the Wulff shape, while all other high-index surfaces are less likely to appear. Therefore, the overall morphology of Wulff shape in Figure 3-12 is preserved.

Notice that our Wulff shape gives an aspect ratio of about one. The particles obtained through a hydrothermal synthesis have aspect ratios that range from three [18, 23] to ten [24]. We suspect that surface chemistry in solution can induce a change in the aspect ratio by modifying the surface energies. One indication we have for this argument is that surface energies of $FePO_4$ (as summarized in Table 3-3) are quite different from the numbers (given in Table 3-1) for $LiFePO_4$ in some directions. While the surface energies of $FePO_4$ in the [1 0 1] and [2 0 1] directions are mildly changed compared to those of $LiFePO_4$, a considerably lower surface energy is found in the [0 1 0] orientation of $FePO_4$, suggesting the thickness of the Wulff shape in the [0 1 0] direction can be further reduced if a $FePO_4$ layer is formed at the (0 1 0) surface. Moreover, the (1 0 0) and (0 1 1) surfaces of $FePO_4$ are calculated to be high in energy and their appearances are thermodynamically inhibited. Overall, more area of the (0 1 0) facet will be exposed in the Wulff shape of $FePO_4$.

Table 3-3 Surface energies of $FePO_4$ in five orientations that appear in the Wulff shape of $LiFePO_4$.

Orientation	(100)	(010)	(101)	(011)	(201)
γ (J/m^2)	0.92	**0.24**	0.53	1.00	0.77

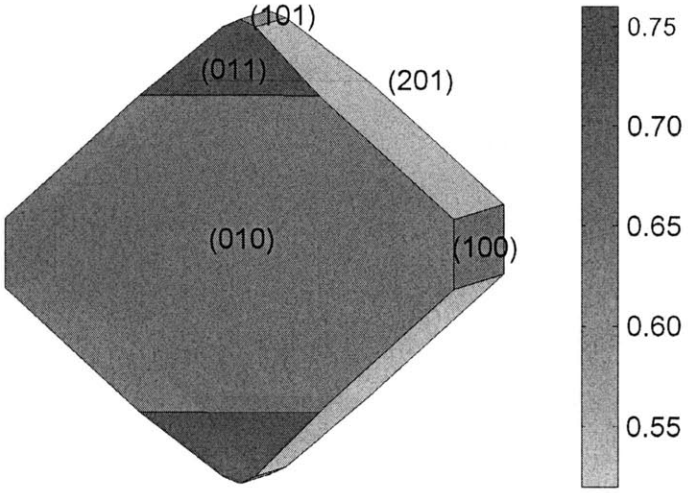

Figure 3-12 Wulff shape of $LiFePO_4$ using the calculated surface energies in nine directions. The grey scale bar on the right gives the energy scale of the surface in units of J/m^2.

B. $LiMnPO_4$

The Wulff shape for $LiMnPO_4$ based on the surface energies in Table 3-1 is shown in Figure 3-13. A grey scale scheme is used with the lighter surfaces indicating lower surface energy. Only six of the fifteen surfaces that we considered appear in the Wulff shape. The other surfaces are not stable against combinations of the six facets. The (301) surface is calculated to be low in energy but is not stable with respect to the formation of faceting by (201) and (100) facets. The (010), (011), and (201) surfaces dominate in the Wulff shape of $LiMnPO_4$. These three surfaces contribute about 87% of the total surface area in Figure 3-13. The Wulff shape is truncated by the (101) surface in the [001] direction and capped by the (100) facet.

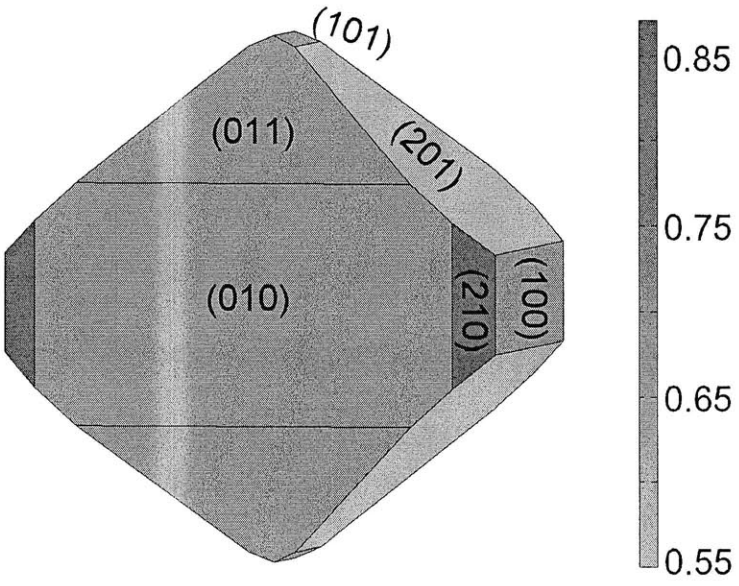

Figure 3-13 Wulff shape of $LiMnPO_4$ using the calculated surface energies in fifteen directions. The grey scale bar on the right gives the energy scale of the surface in units of J/m^2.

3.3.5 Surface Li potentials

It is interesting to compare the redox potentials to extract Li from various surfaces. The delithiation of a given surface of $LiMPO_4$ can be expressed by,

$$(LiMPO_4)_n \leftrightarrow mLi + (Li)_{n-m}(MPO_4)_n \tag{3-6i}$$

Here, an amount m of Li is extracted from the surface of a slab with n units of $LiMPO_4$. The average redox potential for this delithiation process on the surface can be calculated as,

$$V = -\frac{G[(LiMPO_4)_n] - G[(Li)_{n-m}(MPO_4)_n]}{m} + \mu^{\circ}(Li) \tag{3-6ii}$$

where G is the Gibbs free energy of the slab and $\mu^{\circ}(Li)$ is the anode reference chemical potential for Li. Typically, the Gibbs free energy can be replaced by the ground state energy.[71] In this study, we calculate the Li redox potentials only for the surfaces that appear in our Wulff shapes. In practice, all the Li atoms on the top (and also symmetrically equivalent Li atoms on the bottom) outermost layer of each slab are extracted: that is, $Li_{(1)}$ and $Li_{(2)}$ (see Figure 3-7) for the (1 0 1) surface, and $Li_{(1)}$ (see Figure 3-3, 3-4, 3-6 and 3-10) for the other four surfaces. Therefore, the calculated surface redox potentials should be interpreted as the average redox potentials to extract/insert Li from/into the outermost layer of a given surface. The results (see Table 3-1) show that the redox potentials for different surfaces of $LiFePO_4$ range from 2.95 to 3.84 V, compared with the calculated Li insertion/deinsertion redox potential of 3.55 V in the bulk. Among these five surfaces, the (0 1 0) direction has the lowest potential, indicating the energetic preference of extracting Li from this surface.

The surface potentials for $LiMnPO_4$ range from 3.20 V to 4.18 V, compared to the calculated Li insertion/extraction redox potential of 4.00 V in the bulk. The bulk redox potential is consistent with previous work[56] and is within a few percent of the experimental voltage (4.1 V) [72]. All surfaces, except for (100) and (011), have a redox potential lower than the bulk value. Similar to $LiFePO_4$, the (010) surface of $LiMnPO_4$ has the lowest surface redox potential of 3.20 V.

3.4 Discussions

3.4.1 Surface energies for $LiMPO_4$

The stoichiometric $LiFePO_4$ surfaces we have investigated cut through LiO_6 and FeO_6 tetrahedra, leaving under-coordinated Li and Fe exposed on the surfaces. The energy of a surface can be lowered by increasing the bonding strength between the under-coordinated cations and nearby O atoms. Typically, this bond strengthening is observed as a shortened bond length after surface relaxation on most surfaces we studied. The under-coordinated Li atoms are most likely to undergo large inplane displacements on the surface. The coordination of $Li_{(1)}$ (see Figure 3-3) on the (1 0 0) surface is reduced from three to two, and the 5-fold coordinated $Li_{(2)}$ (see Figure 3-6) on the (0 1 1) surface becomes 4-fold coordinated after the relaxation. Extra Li-O bond is formed on the (1 1 0) surface and increase the coordination of one Li ($Li_{(1)}$ in Figure 3-8) from three to four. In contrast, the under-coordinated Fe atoms usually lower their energies by inward displacements towards the bulk.

Our simple model developed to fit the surface energy in terms of coordination changes of Li and Fe shows that coordination loss is energetically more unfavorable for Fe atoms than it is for Li. Therefore, a low energy surface generally has fewer Fe-O bonds affected by the surface cut. This statement is verified by comparing the coordination change per area for different surfaces. For example, the low energy (0 1 0) surface has a Fe coordination number loss of about 4.0 bonds per nm^2, compared with a value of about 6.3 bonds per nm^2 for the high energy (0 0 1) surface. The surfaces that leave 3-fold coordinated Fe exposed (e.g. the (0 0 1) and (1 1 0) surfaces) are calculated

to be high energy surfaces. The coordination based energy expansion in equation (3-5) also allows us to deduce from the *ab-initio* computations that the energy to create under-coordinated Fe on the surface approximately scales with its degree of under-coordination. The displacements for Fe on the surface are generally small, so that the energy of a surface can not be effectively lowered by the local relaxations of the under-coordinated Fe atoms. Conversely, the under-coordinated Li can lower the energy of a surface by more freely relaxing. This is partially reflected in our fitting model where the under-coordinated Li atoms contribute quite differently from the Fe to the surface energies. Under-coordinated Li atoms on the surface are somehow beneficial to reduce the energy of the surface cut, and the 5-fold Li is found to be the lowest energy configuration on the surface. This may be a reflection of the general fact that the potential to extract Li from tetrahedral sites is higher than for octahedral sites in bulk materials, as can be observed by comparing Li-voltages for spinels and layered oxides with the same active redox couple.[73] Therefore, it is not surprising to see that under-coordinated Li has a negative energy contribution to the surface energy in our model. All else being equal, six-fold is not the preferred coordination for Li. The importance of our fitting model for the surfaces of $LiFePO_4$ also lies in its ability to predict the energetics of high-index surfaces, which are computationally challenging in DFT. As a test, the surface energy in the high-index [4 0 1] orientation is calculated using both our fitting model and *ab-initio* methods. For the unrelaxed (4 0 1) surface (with a base area of 131 $Å^2$), there are two 3-fold Fe ions, one 4-fold Fe ion, and two 5-fold Fe ions, together with one 3-fold Li ion and two 5-fold

Li ions. Applying the fitted parameters given in Table 3-2, we predict the surface energy in the [4 0 1] direction to be 1.29 J/m^2, which is in good agreement with the value of 1.15 J/m^2 calculated using the direct *ab-initio* approach, even though the latter value was not used in the fit.

We can see from Table 3-1 that surface energies of $LiMnPO_4$ are relatively low in the following six orientations: (100), (010), (011), (101), (201), and (301). The first five surfaces appear in the Wulff shape of $LiMnPO_4$, together with the (210) surface. The six lowest energy surfaces for $LiMnPO_4$ and $LiFePO_4$ are the same (though not in the same order). Moreover, the surface energies for $LiMnPO_4$ are very similar to those of $LiFePO_4$, even for the high energy surfaces. Therefore, we can conclude that for clean and stoichiometric surfaces of the olivine structure $LiMPO_4$ (M = Fe, Mn), the surface energies are largely controlled by the coordination loss on the surfaces, and the effect of chemistry difference between Fe and Mn on the surface energies is limited. For $LiFePO_4$, the coordination loss of Fe is found to be the most important contribution to the surface energy. We believe that this argument also applies for the surfaces of $LiMnPO_4$.

3.4.2 Wulff shape difference between $LiMnPO_4$ and $LiFePO_4$

Given that in most orientations the surface energy of $LiMnPO_4$ is very close to the value for $LiFePO_4$, it is not surprising that the Wulff shape for $LiMnPO_4$ looks quite similar to the one obtained for $LiFePO_4$. However, compared to the Wulff shape for $LiFePO_4$ (see Figure 3-12), the (210) surface of $LiMnPO_4$ now appears in the equilibrium

shape and replaces the edge shared by the (010) and (100) surfaces (see Figure 3-13). This surface is also suggested to be one of the high-index surfaces that might appear in the Wulff shape of $LiFePO_4$ when more high-index surfaces are included.[34] Note that the surface energy of (011) is calculated to be 0.67 J/m^2 for $LiMnPO_4$ compared to 0.76 J/m^2 for $LiFePO_4$. While surface energies in other directions of $LiMnPO_4$ do not deviate too much from the numbers for $LiFePO_4$, the surface energy decrease of about 0.09 J/m^2 in the [011] orientation exposes this surface more in the Wulff shape of $LiMnPO_4$.

A significant uncertainty in applying these surface energies to morphology of real $LiMPO_4$ (M = Fe or Mn) particles comes from our current assumption of stoichiometry on the surfaces. It is likely that the Wulff shape will vary somewhat with chemical environment. In particular, environments that cause partial oxidation of the surface could modify the Wulff shape of the crystal. A hint of this can be observed by comparing the surface energies of $FePO_4$ (Table 3-3) with those of $LiFePO_4$ (Table 3-1). For $FePO_4$ the ratio of the (0 1 0) surface energy to the surface energy of any of the facets perpendicular to it (e.g. (2 0 1) surface) is much smaller than for $LiFePO_4$, indicating a more extreme aspect ratio for the Wulff shape of $FePO_4$ with a larger contribution of the (0 1 0) facet to total surface area. Note that oxidation (Li removal) does not occur at the same potential for all surfaces, creating the possibility that under some chemical conditions several surfaces would be lithiated while others might be free of Li. In addition, given the importance of oxygen coordination of the exposed cations for the surface energy, the adsorption of O-containing species (e.g. OH^- and H_2O) is likely to affect the surface

energy in aqueous environments such as hydrothermal synthesis. In next chapter, we will show that loss of Li (in water during hydrothermal synthesis for example), absorption of oxygen and/or OH at the under-coordinated surface sites can indeed modify the surface energies, and result in changes to equilibrium particle morphology.

In summary, our results reveal the importance of controlling not only the size of $LiMPO_4$ but also the morphology. Given the highly anisotropic nature of this material, maximizing the exposure of some surfaces over others may be very beneficial for optimal rate capability.

3.4.3 Surface potentials and implications of (de)lithiation mechanism for nano-$LiMPO_4$

Finally, we believe that our calculations of surface redox potentials can provide insights into the possible Li insertion/deinsertion mechanism, particularly for materials with small particle size, where surface effects on the (de)lithiation thermodynamics are expected to be significant. The Li redox potential for the $LiFePO_4$ (0 1 0) surface is 2.95 V, significantly lower than the calculated bulk value of 3.55 V. Spin density integrations for the delithiated (0 1 0) surface further confirm that the hole (Fe^{3+}) created when the 3-fold Li ($Li_{(1)}$ in Figure 3-4) is extracted from the surface locates at the 5-fold Fe ($Fe_{(2)}$ in Figure 3-4). On the (0 1 0) surface the 3-fold Li shares edges with both the PO_4 tetrahedron and the capped FeO_6 octrahedron ($Fe_{(2)}$ in Figure 3-4). The edge-sharing between the 3-fold Li and 5-fold Fe further increases the energy of the 3-fold Li, and

contributes to the decrease in the redox potential for the (0 1 0) surface. We performed similar redox potential calculations for the *insertion* of Li on the (0 1 0) surface of $FePO_4$ and fount it to be 2.95V. Hence, we expect that for a well-faceted $LiFePO_4$ particle, Li will be first extracted from the (0 1 0) surface upon charging and inserted last upon discharging. Furthermore, the same energetic considerations suggest that in the discharging process, any Li on the (0 1 0) surface would move deeper into the bulk where its potential (energy) is higher (lower). Such a mechanism may be beneficial for rapid discharge as the (0 1 0) direction is the only direction along which Li can propagate into the bulk.[2] Hence, any clearing of the surface upon charge and discharge should facilitate Li motion across the surface layer.

Interestingly, the redox potential is not below the bulk value for all $LiFePO_4$ surfaces. For three of the five surfaces in the Wulff shape, the stronger Li binding caused by the under-coordination does lead to a higher potential (Table 3-1) than the bulk, and hence the intuitive idea that ions at surfaces are less strongly bound may have to be abandoned. These surfaces will be lithiated for most of the charge/discharge cycle and may therefore form an obstacle to rapid Li insertion/extraction from the particle.

Among the six surfaces that appears in the Wulff shape of $LiMnPO_4$, the (010) surface has the lowest redox potential, about 0.8 V lower than the bulk value, indicating that it is energetically favorable to extract Li first from this surface. This result is consistent with what is found for $LiFePO_4$ though the difference from the bulk value is larger for $LiMnPO_4$. Therefore, one can expect that the Li extraction for $LiMnPO_4$ nano-

particles is also inhomogeneous: Li will be preferentially extracted first from the (010) surface. There are significant differences with $LiFePO_4$ for the other surfaces. While in $LiFePO_4$ the surfaces orthogonal to (010) almost all have a potential above the bulk extraction potential, in $LiMnPO_4$ all surfaces, except for (100) and (011), are below the bulk potential. Hence, while in $LiFePO_4$ plates with [010] orientation will have a lithiated edge when the core is delithiated, this is unlikely to be the case for $LiMnPO_4$. We have speculated that the surface regions are responsible for the electrochemical capacity that has been observed [32] above and below the bulk potential in nano-$LiFePO_4$. If this is the case, then $LiMnPO_4$ would behave differently from $LiFePO_4$ in the nano-regime. While the excess capacity of $LiFePO_4$ will be found below and above the bulk potential, in $LiMnPO_4$ it will be mainly distributed below the bulk potential. A careful comparison of the capacity outside the two-phase region for $LiFePO_4$ and $LiMnPO_4$ may therefore give some insight into whether it originates from the surfaces or from the elastic effects on the miscibility gap.[31]

The (010) surface is the most important surface as it directly gives access to the [010] channels along which Li diffuses through the olivine structure. For both $LiFePO_4$ and $LiMnPO_4$ the potential to delithiate the (010) surface is well below the bulk potential though the difference between bulk and surface is larger in $LiMnPO_4$ (0.8 V) than in $LiFePO_4$ (0.6 V). This indicates a significant barrier for Li to cross through the (010) surface layer (Figure 3-14).[74] Even though this barrier has to be crossed only once upon charge and discharge, the fact that it is several hundreds of meV larger than the Li

hopping barrier in the bulk[2] likely makes it the rate-limiting factor for all but the largest particle sizes. Moreover, this energy barrier in $LiMnPO_4$ is 0.2 eV higher than in $LiFePO_4$, which may explain why the kinetics of $LiMnPO_4$ is so much slower than for $LiFePO_4$. Assuming the same pre-factor for the activated surface crossing in both materials, the difference in activation energy (200 meV) accounts for a rate difference of $\exp(200\text{meV}/k_B\text{T}) \approx 2{,}000$ at room temperature. If the surface potential is the rate limiting factor, then it becomes likely that other surfaces such as (011) and (210) allow for faster access to the bulk since they have a lithiation potential much closer to the bulk value. However, if diffusion in the bulk is truly one-dimensional then these surfaces only give access to the part of the bulk material for which the [010] channels exit at these surfaces.

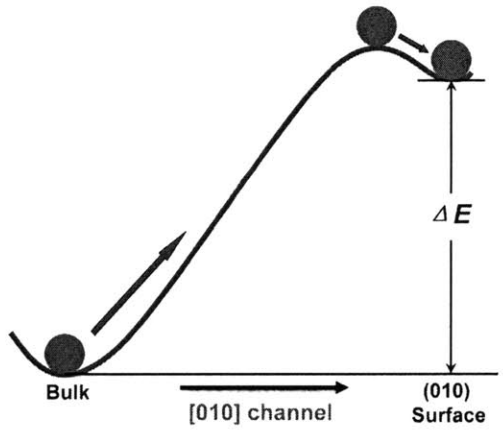

Figure 3-14 Schematic drawing of the energy landscape for the Li migration along the [010] diffusion channel. The energy difference (ΔE) between the bulk Li sites and the Li sites in the outmost (010) surface layer is about 0.8 eV for $LiMnPO_4$.

3.5 Conclusions

In summary, we have investigated several surface properties of olivine structured $LiFePO_4$ and $LiMnPO_4$. The calculated surface energies and surface Li redox potentials are found to be very anisotropic. The strong anisotropy in the calculated surface Li potentials suggests that lithiation/delithiation of well-faceted nano-$LiMPO_4$ particles may proceed in a non-trivial manner. Our results indicate the importance of considering surface effects when investigating the thermodynamics and kinetics of nano-scale electrode materials. The equilibrium particle morphology for $LiMPO_4$ under vacuum condition does not exhibit the desired plate shape to maximally expose the reaction active (010) surface. In the next chapter we continue to investigate the effect of external chemical conditions on the equilibrium particle shape for $LiMPO_4$.

Table 3-X Relaxations (displacements Δu, Δv, and Δw are in Å) of under-coordinated Li, Fe, and O atoms on the nine surfaces. Only displacements larger than 0.1 Å are provided. The directions of the *u*, *v*, and *w* axes are consistent with the axes shown in Figure 3-3 ~ 3-11: e.g. the *u*, *v*, and *w* axes for the (1 0 0) surface lie along the [0 1 0], [0 0 1], [1 0 0] directions, respectively, as shown in Figure 3-3. Atom labels also refer to Figure 3-3 ~ 3-11.

Surface	Label	Coord.	Δu	Δv	Δw
(100)	$Li_{(1)}$	2	1.47	0.17	0.61
	$Fe_{(1)}$	5	-0.14	0.08	-0.08
	$P_{(1)}$	4	-0.14	-0.13	0.09
	$O_{(1)}$	2	-0.03	-0.29	0.12
	$O_{(2)}$	3	-0.08	-0.13	0.01
	$O_{(3)}$	3	-0.21	-0.19	0.16
	$O_{(4)}$	3	-0.20	-0.13	-0.05
(010)	$Li_{(1)}$	3	-0.07	-0.35	-0.09
	$Fe_{(1)}$	5	0.23	0.06	-0.09
	$Fe_{(2)}$	5	-0.19	-0.12	-0.08
	$P_{(1)}$	4	0.18	-0.15	0.07
	$O_{(1)}$	3	0.04	-0.19	-0.07
	$O_{(2)}$	2	0.28	-0.40	-0.12
	$O_{(3)}$	3	0.32	-0.11	0.29
	$O_{(4)}$	3	0.17	-0.19	-0.09
(001)	$Li_{(1)}$	3	0.07	0.02	-0.37
	$Li_{(2)}$	5	-0.17	0.02	-0.14
	$Li_{(3)}$	5	0.24	-0.04	-0.11
	$Fe_{(1)}$	3	0.07	-0.03	-0.49
	$Fe_{(2)}$	5	0.00	-0.13	0.04
	$P_{(1)}$	4	0.05	-0.12	0.07
	$O_{(2)}$	3	0.07	0.00	-0.13
(201)	$Li_{(1)}$	3	0.14	-0.46	-0.14
	$Li_{(2)}$	5 (4)	-0.17	-0.15	-0.04
	$Li_{(3)}$	5 (4)	0.15	-0.13	-0.05
	$Fe_{(1)}$	4	0.01	-0.18	-0.21
	$Fe_{(2)}$	5	-0.02	-0.03	-0.15
	$O_{(3)}$	2	-0.04	-0.15	0.09
	$O_{(4)}$	3	0.03	-0.20	-0.01
(011)	$Li_{(1)}$	3	-0.37	-1.57	-0.12
	$Li_{(2)}$	4	-0.10	0.51	0.02
	$Li_{(3)}$	5	-0.05	-0.34	-0.10
	$Fe_{(1)}$	4	-0.02	-0.21	-0.46
	$Fe_{(2)}$	4	-0.05	0.31	-0.47
	$O_{(1)}$	1	-0.08	-0.25	0.00
	$O_{(2)}$	2	-0.14	0.09	0.01
	$O_{(4)}$	3	0.03	0.14	-0.05
	$O_{(5)}$	3	0.02	-0.14	-0.07
(301)	$Li_{(1)}$	4	-0.11	-0.05	0.00
	$Li_{(2)}$	4	0.11	-0.05	0.00
	$Li_{(3)}$	4 (5)	-0.19	-0.21	0.03
	$Li_{(4)}$	4 (5)	0.19	-0.20	0.02
	$Fe_{(1)}$	5	0.00	-0.17	-0.07
	$Fe_{(2)}$	4	0.00	-0.14	-0.12
	$Fe_{(3)}$	5	-0.01	0.25	0.10
	$Fe_{(4)}$	5	0.00	0.06	-0.11
	$P_{(1)}$	4	-0.01	-0.18	0.09
	$P_{(2)}$	4	0.00	0.16	0.04
	$O_{(1)}$	1	0.00	-0.41	-0.06
	$O_{(2)}$	3	0.01	-0.16	-0.02
	$O_{(3)}$	3	-0.03	-0.14	-0.02
	$O_{(7)}$	2	0.00	0.15	-0.08
	$O_{(8)}$	3	0.00	0.24	-0.10
	$O_{(9)}$	3(4)	0.02	0.15	-0.02
	$O_{(10)}$	3(4)	-0.02	0.15	-0.02
(101)	$Li_{(1)}$	3	-0.17	0.29	-0.32
	$Li_{(2)}$	3	-0.10	0.21	-0.42
	$Fe_{(2)}$	4	-0.02	0.00	-0.32
	$O_{(2)}$	2	0.04	0.16	-0.04
	$O_{(4)}$	3	-0.04	0.14	-0.06
	$O_{(6)}$	3	0.04	-0.11	-0.04
(110)	$Li_{(1)}$	4	0.16	2.95	-0.19
	$Fe_{(1)}$	3	-0.50	-0.83	-0.48
	$Fe_{(2)}$	5	0.26	0.32	-0.03
	$P_{(2)}$	4	0.15	-0.07	0.07
	$O_{(1)}$	2	-0.05	0.38	-0.04
	$O_{(2)}$	3	0.06	-0.02	-0.16
	$O_{(3)}$	3	0.05	-0.04	0.15
	$O_{(5)}$	3	0.17	-0.02	0.10
(111)	$Li_{(1)}$	3	-0.16	0.49	-0.49
	$Li_{(2)}$	4	-0.10	0.00	-0.34
	$Li_{(3)}$	5	-0.22	-0.15	-0.36
	$Fe_{(1)}$	3	-0.02	0.01	-0.45
	$Fe_{(2)}$	4	-0.02	0.10	-0.73
	$P_{(2)}$	4	0.18	-0.15	-0.12
	$O_{(1)}$	2	0.21	-0.10	-0.17
	$O_{(2)}$	3	-0.16	0.24	-0.14
	$O_{(3)}$	2	-0.39	-0.38	-0.22
	$O_{(4)}$	2	0.04	0.22	-0.31
	$O_{(5)}$	3	0.05	-0.10	-0.21
	$O_{(6)}$	3	-0.17	0.01	-0.33
	$O_{(7)}$	3	-0.10	0.08	-0.16
	$O_{(8)}$	3	0.00	-0.04	-0.25

References:

[1] T. Maxisch and G. Ceder, Physical Review B **73**, 174112 (2006).

[2] D. Morgan, A. Van der Ven, and G. Ceder, Electrochemical and Solid State Letters 7, A30 (2004).

[3] M. S. Islam, D. J. Driscoll, C. A. J. Fisher, and P. R. Slater, Chem. Mater. **17**, 5085 (2005).

[4] R. Amin, P. Balaya, and J. Maier, Electrochemical and Solid-State Letters **10**, A13 (2006).

[5] S. Y. Chung, J. T. Bloking, and Y. M. Chiang, Nature Materials **1**, 123 (2001).

[6] H. Huang, S. C. Yin, and L. F. Nazar, Electrochemical and Solid State Letters **4**, A170 (2001).

[7] J. Barker, M. Y. Saidi, and J. L. Swoyer, Electrochem. Solid-State Lett. **6**, A53 (2003).

[8] P. S. Herle, B. Ellis, N. Coombs, and L. F. Nazar, Nat. Mater. **3**, 147 (2004).

[9] A. Yamada, S. C. Chung, and K. Hinokuma, Journal of The Electrochemical Society **148**, A224 (2001).

[10] C. Delacourt, P. Poizot, S. Levasseur, and C. Masquelier, Electrochemical and Solid-State Letters **9**, A352 (2006).

[11] B. Kang and G. Ceder, Nature **458**, 190 (2009).

[12] D. H. Kim and J. Kim, Electrochemical and Solid State Letters **9**, A439 (2006).

[13] T. R. Kim, D. H. Kim, H. W. Ryu, J. H. Moon, J. H. Lee, S. Boo, and J. Kim, J. Phys. Chem. Solids **68**, 1203 (2007).

[14] S. Y. Lim, C. S. Yoon, and J. P. Cho, Chem. Mater. **20**, 4560 (2008).

[15] A. V. Murugan, T. Muraliganth, P. J. Ferreira, and A. Manthiram, Inorganic Chemistry **48**, 946 (2009).

[16] D. Y. Wang, et al., J. Power Sources **189**, 624 (2009).

[17] S. F. Yang, P. Y. Zavalij, and M. S. Whittingham, Electrochem. Commun. **3**, 505 (2001).

[18] J. Chen and M. S. Whittingham, Electrochemistry Communications **8**, 855 (2006).

[19] S. Franger, F. Le Cras, C. Bourbon, and H. Rouault, Electrochemical and Solid State Letters **5**, A231 (2002).

[20] S. Tajimi, Y. Ikeda, K. Uematsu, K. Toda, and M. Sato, Solid State Ionics **175**, 287 (2004).

[21] G. Meligrana, C. Gerbaldi, A. Tuel, S. Bodoardo, and N. Penazzi, J. Power Sources **160**, 516 (2006).

[22] K. Dokko, S. Koizumi, K. Sharaishi, and K. Kanamura, J. Power Sources **165**, 656 (2007).

[23] K. Dokko, S. Koizumi, and K. Kanamura, Chemistry Letters **35**, 338 (2006).

[24] G. Chen, X. Song, and T. J. Richardson, Electrochem. Solid-State Lett. **9**, A295 (2006).

[25] C. Delacourt, P. Poizot, M. Morcrette, J. M. Tarascon, and C. Masquelier, Chem. Mater. **16**, 93 (2004).

[26] M. Yonemura, A. Yamada, Y. Takei, N. Sonoyama, and R. Kanno, J. Electrochem. Soc. **151**, A1352 (2004).

[27] N. H. Kwon, T. Drezen, I. Exnar, I. Teerlinck, M. Isono, and M. Graetzel, Electrochemical and Solid State Letters **9**, A277 (2006).
[28] H. S. Fang, L. P. Li, and G. S. Li, Chemistry Letters **36**, 436 (2007).
[29] A. Yamada and S. C. Chung, J. Electrochem. Soc. **148**, A960 (2001).
[30] C. Delacourt, L. Laffont, R. Bouchet, C. Wurm, J. B. Leriche, M. Morcrette, J. M. Tarascon, and C. Masquelier, J. Electrochem. Soc. **152**, A913 (2005).
[31] N. Meethong, H. Y. S. Huang, S. A. Speakman, W. C. Carter, and Y. M. Chiang, Advanced Functional Materials **17**, 1115 (2007).
[32] N. Meethong, H. Y. S. Huang, W. C. Carter, and Y. M. Chiang, Electrochemical and Solid State Letters **10**, A134 (2007).
[33] M. Wagemaker, F. M. Mulder, and A. Van der Ven, Adv. Mater. **21**, 1 (2009).
[34] L. Wang, F. Zhou, Y. S. Meng, and G. Ceder, Phys. Rev. B **76**, 165435 (2007).
[35] F. Zhou, T. Maxisch, and G. Ceder, Phys. Rev. Lett. **97**, 155704 (2006).
[36] L. Laffont, C. Delacourt, P. Gibot, M. Y. Wu, P. Kooyman, C. Masquelier, and J. M. Tarascon, Chem. Mater. **18**, 5520 (2006).
[37] V. Srinivasan and J. Newman, J. Electrochem. Soc. **151**, A1517 (2004).
[38] G. Wulff, Z. Kristallogr. Mineral. **34**, 449 (1901).
[39] J. W. Gibbs, *The collected works of J. Willard Gibbs* (Longmans, Green and Co., New York, 1928).
[40] D. Bertsimas and J. N. Tsitsiklis, *Introduction to linear optimization* (Athena Scientific, Belmont, MA, 1997).
[41] http://www.qhull.org.
[42] P. Hartman and P. Bennema, Journal of Crystal Growth **49**, 145 (1980).
[43] G. Friedel, Bull. Soc. Fr. Mineral. **30**, 326 (1907).
[44] J. D. H. Donnay and D. Harkei, Am. Mineral. **22**, 446 (1937).
[45] M. Ramamoorthy, D. Vanderbilt, and R. D. King-Smith, Phys. Rev. B **49**, 16721 (1994).
[46] A. Christensen and E. A. Carter, Phys. Rev. B **58**, 8050 (1998).
[47] I. Batyrev, A. Alavi, and M. W. Finnis, Faraday Discussions **114**, 33 (1999).
[48] X. G. Wang, A. Chaka, and M. Scheffler, Phys. Rev. Lett. **84**, 3650 (2000).
[49] A. Marmier and S. C. Parker, Phys. Rev. B **69**, 115409 (2004).
[50] K. Reuter and M. Scheffler, Phys. Rev. B **65**, 035406 (2001).
[51] X. G. Wang, W. Weiss, S. K. Shaikhutdinov, M. Ritter, M. Petersen, F. Wagner, R. Schlogl, and M. Scheffler, Phys. Rev. Lett. **81**, 1038 (1998).
[52] G. Kresse, S. Surnev, M. G. Ramsey, and F. P. Netzer, Surf. Sci. **492**, 329 (2001).
[53] P. Raybaud, J. Hafner, G. Kresse, S. Kasztelan, and H. Toulhoat, J. Catal. **189**, 129 (2000).
[54] V. I. Anisimov, J. Zaanen, and O. K. Andersen, Phys. Rev. B **44**, 943 (1991).
[55] V. I. Anisimov, F. Aryasetiawan, and A. I. Liechtenstein, J. Phys.: Condens. Matter **9**, 767 (1997).
[56] F. Zhou, M. Cococcioni, C. A. Marianetti, D. Morgan, and G. Ceder, Phys. Rev. B **70**, 235121 (2004).
[57] A. I. Liechtenstein, V. I. Anisimov, and J. Zaanen, Phys. Rev. B **52**, R5467 (1995).
[58] G. Rousse, Chem. Mater. **15**, 4082 (2003).

[59] X. A. Huang, J. F. Ma, P. W. Wu, Y. M. Hu, J. H. Dai, Z. B. Zhu, H. Y. Chen, and H. F. Wang, Mater. Lett. **59**, 578 (2005).
[60] P. W. Tasker, J. Phys. C: Solid State Phys. **12**, 4977 (1979).
[61] D. C. Sayle, D. H. Gay, A. L. Rohl, C. R. A. Catlow, J. H. Harding, M. A. Perrin, and P. Nortier, J. Mater. Chem. **6**, 653 (1996).
[62] P. M. Oliver, G. W. Watson, E. T. Kelsey, and S. C. Parker, J. Mater. Chem. **7**, 563 (1997).
[63] E. Heifets, R. I. Eglitis, E. A. Kotomin, J. Maier, and G. Borstel, Surf. Sci. **513**, 211 (2002).
[64] S. Hamad, S. Cristol, and C. R. A. Callow, Journal of Physical Chemistry B **106**, 11002 (2002).
[65] A. Hung, J. Muscat, I. Yarovsky, and S. P. Russo, Surf. Sci. **520**, 111 (2002).
[66] A. Eichler and G. Kresse, Phys. Rev. B **69**, 045402 (2004).
[67] R. A. Evarestov, E. A. Kotomin, D. Fuks, J. Felsteiner, and J. Maier, Applied Surface Science **238**, 457 (2004).
[68] A. Soon, M. Todorova, B. Delley, and C. Stampfl, Phys. Rev. B **75** (2007).
[69] A. B. Mukhopadhyay, J. F. Sanz, and C. B. Musgrave, Phys. Rev. B **73** (2006).
[70] G. Strang, *Applied Mathematics and Scientific Computing* (Wellesley-Cambridge Press, Wellesley, MA, 2006).
[71] M. K. Aydinol, A. F. Kohan, and G. Ceder, J. Power Sources **68**, 664 (1997).
[72] G. H. Li, H. Azuma, and M. Tohda, Electrochemical and Solid State Letters **5**, A135 (2002).
[73] S. K. Mishra and G. Ceder, Phys. Rev. B **59**, 6120 (1999).
[74] L. Wang, F. Zhou, and G. Ceder, Electrochemical and Solid State Letters **11**, A94 (2008).

Chapter 4

Ab initio Processing Product of $LiFePO_4$ Particle Morphology under Aqueous Solutions

In this chapter, we present an *ab initio* approach that can be used to study surface adsorption from aqueous solutions and the equilibrium particle morphology as function of the aqueous environment. The approach involves defining reference energies for aqueous species which, when used with *ab initio* energies for the solid state, provide the correct dissolution thermodynamics. We demonstrate for $LiFePO_4$ that *ab initio* calculations can be used effectively to investigate the crystal shape dependency on practical parameters, such as electric potential E and solution pH.

4.1 Introduction of crystal morphology control

The particle morphology control for advanced functional materials has enormous applications in various fields, e.g. catalysis, electronics, and batteries.[1-6] Shape control is critical because many inorganic crystals exhibit anisotropic performances in their interesting properties. Morphology of inorganic crystal phases is known to rely on many factors, such as, growth rates of facets [7, 8], strain effects [9-11], and temperature dependent surface energies [12-14]. While particle shape can be tailored effectively in experiments through careful determination of synthesis conditions [15], much of the previous theoretical studies of crystal morphology focus on surface energies of crystal phases [16-19]. With the calculated surface energies, one can predict the equilibrium particle shape through the

well-known Wulff construction,[20] which minimize the total surface energy subject to the constraint of constant volume. For example, using first-principle calculations, Yang et al. managed to find a morphology control agent so that anatase TiO_2 particle can lower its surface energy in the [001] direction and therefore expose the reactive (001) surface to a large extent.[21] The successful shape optimization for anatase TiO_2 crystal demonstrates the power of *ab initio* calculations in modern material design. However, the extension of this success to other inorganic crystals remains challenging. Crystal growth is strongly governed by the balance between kinetic growth and thermodynamic growth.[22] Only in the equilibrium growth region with a sufficient supply of thermal energy (kT) and a low flux of monomers, do crystals grow in their thermodynamically stable form. Hence, to take advantage of the surface energies predicted from *ab initio* calculations, one has to ensure that crystals of interest are synthesized under conditions where thermodynamic growth dominates. This makes material synthesis in aqueous environment particularly attractive in that one can carefully control the solution temperature. Aqueous growth of materials also offers other significant control parameters to influence the particle morphology. Chemical species in aqueous solution can bind to crystal facets and affect the relative surface energies and hence the concentration of these species can be used to tailor crystal shape.

Some challenges still exist for the *ab initio* modeling of surfaces in aqueous solution. One needs a systematic construction of surface free energies for crystals under different aqueous environment. Since the surfaces are open systems, their free energies contain the chemical potentials for chemical species absorbed from the solution. This requires that one can approximately describe *ab initio* calculated energies in the solid state with the

energetics of ions in solution. In this paper, we present a formalism in which the energy of aqueous species and gas phase specie can be used in conjunction with *ab-initio* data for solid state phases in the optimization of crystal morphology. We apply this to predict the equilibrium crystal shape of $LiFePO_4$ as a function of parameters characterizing practical solutions, such as electric potential E and solution pH. $LiFePO_4$ has appeared as an important cathode material in Li-ion battery field. In the past few years, much research efforts are devoted to the synthesis of olivine-structure $LiMPO_4$ (M = Fe, Mn, Co, Ni) under aqueous environment.[23-29] One benefit of synthesizing this family of compounds via solution approaches is the relatively effective control of particle morphology. According to previous computational and experimental studies,[30-32] lithium diffusion inside the olivine structure $LiMPO_4$ is believed to be one dimensional along the [010] direction of the orthorhombic lattice (space group P*nma*). Hence, maximal exposure of that facet is expected to lead to improved kinetics. The first-principles work presented in this paper is helpful in finding a synthesis condition that favors the production of platelet shape $LiFePO_4$ with large area of active (010) surface, and providing some insights about the morphology control of $LiMPO_4$ for future research efforts.

4.2 *Ab initio* morphology control under aqueous environment

To model the equilibrium crystal shape under aqueous solution, we consider the appearance of four types of chemical species on the present case of $LiFePO_4$ surfaces. In Chapter 3, we have introduced that surface grand potential is used to evaluate the thermodynamic equilibrium for crystal facets exposed under an open system. Surface

grand potential defined in equation (3-4ix) of Chapter 3 is used later to evaluate the energy of $LiFePO_4$ surfaces with different adsorbate coverage.

4.2.1 Chemical potentials for surface adsorbates

A) Relations between chemical potentials for surface adsorbates

The evaluation of the surface grand potential requires proper chemical potentials for adsorbates from aqueous solution and their proper reference to *ab initio* solid state calculations. There are four types of chemical groups considered in this work: hydrogen (H), water molecule (H_2O), hydroxyl group (OH), and oxygen (O), representing different levels of oxidizing/reducing condition for aqueous solution. In the remaining context of this chapter all the thermodynamic data reported are for ***room temperature*** of 298K, though we use "T" in equations to keep the formalism as general as possible.

We ***calculated*** the total energy for H_2O molecule and subtracted the experimental heat of evaporation at room temperature to obtain the chemical potential of liquid water (referred as μ_{H2O} below). To be consistent with entropy approximations we made earlier in the derivation of surface grand potential, the entropy of liquid water is neglected as well. The activity of water a_{H2O}, exactly equal to the ratio of the vapor pressure of the solution to that of the pure solvent, is practically taken as equal to one. Therefore, the chemical potential of H_2O is fixed at μ_{H2O}.

For H, the following reaction is used to relate the H chemical potential to the oxygen chemical potential of the solution.

H_2O (aqueous) → 2 H (aqueous)+ O (aqueous) (4-1i)

and the following relation holds at equilibrium,

$$\mu_H = \frac{1}{2}\mu_{H2O} - \frac{1}{2}\mu_O \quad (4\text{-}1ii)$$

Due to this equilibrium, the hydrogen chemical potential simply varies opposite to the oxygen chemical potential.

For OH, its chemical potential is the addition of μ_H and μ_O:

$$\mu_{OH} = \mu_H + \mu_O = \frac{1}{2}\mu_{H2O} + \frac{1}{2}\mu_O \quad (4\text{-}1iii)$$

The above relations between chemical potentials of different adsorbates show that the oxygen chemical potential is the ***only*** controlling variable to characterize the solution condition. The chemical potentials for adsorbates H and OH linearly depend on the oxygen chemical potential, and μ_{H2O} is set by the activity of H_2O which is assumed to be constant. Table 4-1 provides the six values of oxygen chemical potential used later in the results section, and the corresponding chemical potentials for the other three types of surface adsorbates.

Table 4-1 Numerical values of chemical potentials (in eV per formula unit of adsorbate) for four types of surface adsorbates at six levels of oxygen chemical potentials.

μ_O	-9.38	-7.38	-5.83	-4.28	-4.18	-4.06
μ_{H2O}	-14.60	-14.60	-14.60	-14.60	-14.60	-14.60
μ_H	-2.57	-3.57	-4.35	-5.12	-5.17	-5.23
μ_{OH}	-11.96	-10.96	-10.18	-9.41	-9.36	-9.30

B) Converting aqueous solution conditions to an equivalent oxygen chemical potential

To describe the chemical condition of an aqueous system, we use the electric potential E and the pH of the solution. These two parameters are used by electrochemistry and corrosion scientists in *Pourbaix* diagrams, which are essentially phase diagrams in this parameter space.[33] We relate E and pH to the oxygen chemical potential through the water oxidation reaction,

$$H_2O\ (aqueous) \rightarrow 2\ H^+ + \tfrac{1}{2}\ O_2\ (gaseous) + 2\ e^- \qquad (4\text{-}2i)$$

The reaction Gibbs free energy of (4-2i) can be evaluated as,

$$\Delta G = \mu_O + 2 * \mu_{H+} - 2\ E * F - \mu_{H2O} \qquad (4\text{-}2ii)$$

The electric potential E is referenced to the standard hydrogen electrode and F is the Faraday constant. The chemical potential of proton (μ_{H+}) can be expressed as,

$$\mu_{H+} = \mu^o_{H+} + R * T * ln(a_{H+}) \approx \tfrac{1}{2}\ \mu^o_{H2} + R * T * ln10 * pH \qquad (4\text{-}2iii)$$

where R is the gas constant. μ^o_{H+} and μ^o_{H2} are the chemical potentials respectively for H^+ and gaseous H_2 of standard hydrogen electrode, which is saturated with gaseous hydrogen at 1 atm but is immersed in the solution with unitary activity for H^+ at room

temperature. The equality "$2\mu^{o}_{H+} = \mu^{o}_{H2}$" is valid by convention for standard hydrogen electrode. The assumption that the activities are virtually the same as the concentration, as least in the case of dilute solutions, is used in (4-2iii) for proton. To obtain an accurate chemical potential μ^{o}_{H2} at the standard state, the experimental reaction Gibbs free energy at room temperature is preserved,

$$\Delta G^{exp}_{H2O} = \mu^{o}_{H2} + \mu^{o}_{O} - \mu^{o}_{H2O} = \mu^{o}_{H2} + \mu^{o}_{O} - \mu_{H2O} \quad (4\text{-}2iv)$$

Here we use the chemical potential of water in the liquid state as described in Section 2.2A. μ^{o}_{O} is the chemical potential of gaseous O_2 at 1 atm and room temperature. Using experimental data for water oxidation reaction is critical for our approximation of aqueous solution with E and pH. Plugging equation (4-2iii) and (4-2iv) into equation (4-2ii) and letting Gibbs free energy of reaction (4-2i) equal to zero, one can obtain the relationship between oxygen chemical potential and aqueous solution parameters, E and pH.

$$\mu_{O} = \mu^{o}_{O} + 2 * (In10 * RT * pH + E * F) - \Delta G^{exp}_{H2O} \quad (4\text{-}2v)$$

We assume that the reaction entropy of the water oxidation reaction (4-2i) at the standard state is contributed only by the gaseous O_2. Thus in practice the experimental reaction enthalpy for reaction (4-2i) is used and μ^{o}_{O} is obtained by ***fitting*** the calculated formation energies of non-transition metal oxides to the corresponding experimental enthalpies at room temperature. The calibrated value of -4.28 eV per formula unit of O accounts for the large error that we reported previously for the overbinding of O_2 molecule in generalized gradient approximations to density functional theory, and the inaccurate description of charge transfer from O_2 molecule to O^{2-} anion at the solid state.[34] Figure 4-1 shows the linear relationship between pH and E by numerically evaluating equation (4-

2v) at four values of oxygen chemical potential. Therefore, an aqueous system with certain *pH* and *E* values can be represented by an equivalent oxygen chemical potential. An increase in oxygen chemical potential indicates a more alkaline and/or more oxidizing solution.

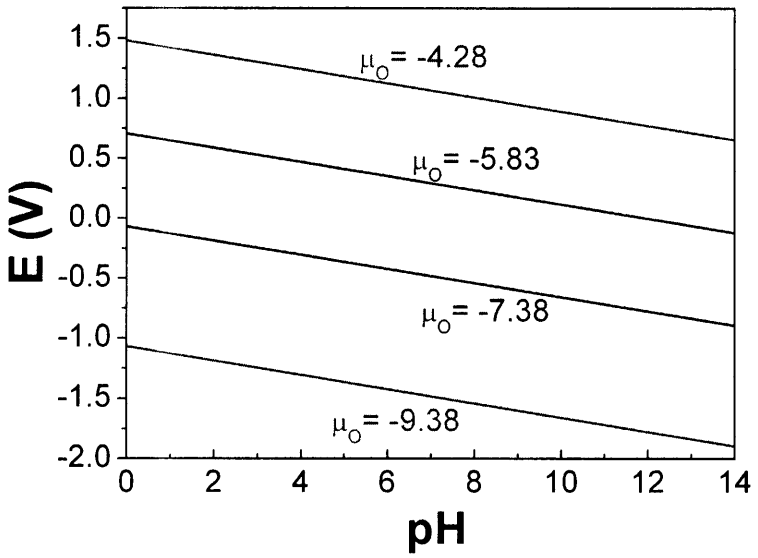

Figure 4-1 Simplified Pourbaix diagram showing the relationship between equivalent oxygen chemical potential (in unit of eV per formula unit of O) and two dependent aqueous solution parameters, electric potential *E* (in unit of V) and solution *pH*. Four levels of constant oxygen chemical potential are shown.

4.2.2 Optimization of particle shape

At given oxygen chemical potential, we first determine the chemical potentials for the four types of surface adsorbates (O, OH, H_2O, and H) mentioned in the previous section, and then evaluate the grand potential for the surface covered by each type of adsorbate. For every crystal facet, the surface adsorption with lowest value in surface grand potential is used as the surface energy in the construction of Wulff shape. By varying oxygen chemical potential, we can simulate the appearance of different surface adsorbates on crystal surfaces, and investigate the change of equilibrium particle shape because of the changing external chemical environment. Using equation (8) in the previous section, we can replace the oxygen chemical potential with practical parameters for aqueous solution, and show the change of surface coverage and Wulff shape as a function of pH and E.

4.2.3 *Ab initio* calculations for case study of $LiFePO_4$

We perform density functional theory calculations on fifteen surfaces of $LiFePO_4$. All total energies in this work are calculated using the Generalized Gradient Approximation (GGA) to the Density Functional Theory (DFT). The projected augmented wave (PAW) [35] method is used, as implemented in the Vienna Ab initio Simulation Package (*VASP*) [36]. We choose an energy cutoff of 400 eV and k-point meshes similar to our investigation of stoichiometric $LiFePO_4$ surfaces.[37] The GGA+U approach [38, 39] is used to accurately calculate the reaction enthalpies for oxidation/reduction of $LiFePO_4$ surfaces. We employ the "fully localized" double counting scheme as presented by Liechtenstein et al.[40]. Similar to previous work, we choose a J value of 1 eV and a U value of 5.3 eV.[41]

Besides studying appearance of different adsorbates on $LiFePO_4$ surfaces, we also consider the possibility of Li dissolving from $LiFePO_4$ surfaces into aqueous solution. This is possible because metallic Li is extremely unstable in water with its dissolution into aqueous Li^+ occurring at an electric potential as low as -3.0 V.[33] Previously we have found that the voltage to remove Li from stoichiometric $LiFePO_4$ surface is in in the range of 2.9 V to 3.8 V depending on the orientation of the surface facet.[37]

A) Li dissolving from $LiFePO_4$ surfaces

The dissolution of Li from $LiFePO_4$ surfaces into aqueous Li^+ can be summarized by the following reaction,

$$LiFePO_4\ (solid) \rightarrow Li_{1-x}FePO_4\ (solid) + x\ Li^+\ (aqueous) + x\ e^- \qquad (4\text{-}3i)$$

where the "*solid*" label inside the parenthesis can represent both bulk phases and surfaces of a $LiFePO_4$ crystal. The Gibbs free energy for equation (4-3i) can be calculated using the formation energies of the relevant solid and aqueous phases,

$$\Delta G = \Delta H_{Li1-xFePO4} + x\ \Delta H_{Li+} - \Delta H_{LiFePO4} + x * RT * ln(a_{Li+}) - x\ E * F - T\Delta S \qquad (4\text{-}3ii)$$

where the activity for aqueous Li^+, a_{Li+}, can be approximated as the ratio of its concentration over the value at the standard state. A solution at the standard state is a hypothetical solution with Li^+ concentration of 1 mol/L at room temperature. If "T" in equation (4-3ii) refers to room temperature, then ΔS represents only the reaction entropy for the dissolution reaction (4-3i) at the standard state. Otherwise, it also contains any entropy deviation from the standard state for the solid phases. This "$T\Delta S$" term is assumed to be small and is neglected in later calculations. Evaluation of formation energy for phases in reaction (4-3ii) is trivial in density functional theory calculations except for

aqueous Li^+. In this work, the following reference reaction is used to obtain an "effective" *ab initio* formation energy for aqueous Li^+:

$$\tfrac{1}{2}\, Li_2O\ (solid) + H^+ \rightarrow Li^+\ (aqueous) + \tfrac{1}{2}\, H_2O\ (aqueous) \qquad (4\text{-}3iii)$$

The idea is to fix the enthalpy difference between a chosen solid reference state Li_2O and the aqueous specie Li^+, and use a formation energy value for aqueous Li^+ which reproduces this reaction enthalpy exactly. Since the experimental dissolution enthalpy for $Li_2O \rightarrow Li^+$ is preserved, the accuracy of the *ab initio* solid-solid energy difference ensures that other solids (e.g. bulk $LiFePO_4$) dissolve at approximately the correct electric potential. This scheme utilizes the power of *ab initio* calculations in accurately describing the formation energy of solids while coupling it to the experimental information on aqueous species and gases, which are less accurately accounted for in density functional theory calculations. Figure 4-2 graphically illustrates the idea behind this approach. The experimental formation enthalpies for solid Li_2O and aqueous phase Li^+ in reaction (4-3iii) are taken from Ref. 49.[42]

Once we obtain the "effective" *ab initio* formation energy of aqueous Li^+, we can use equation (4-3ii) to find the critical electric potential E^{crit}, above which the reaction Gibbs free energy for the Li dissolution reaction becomes negative.

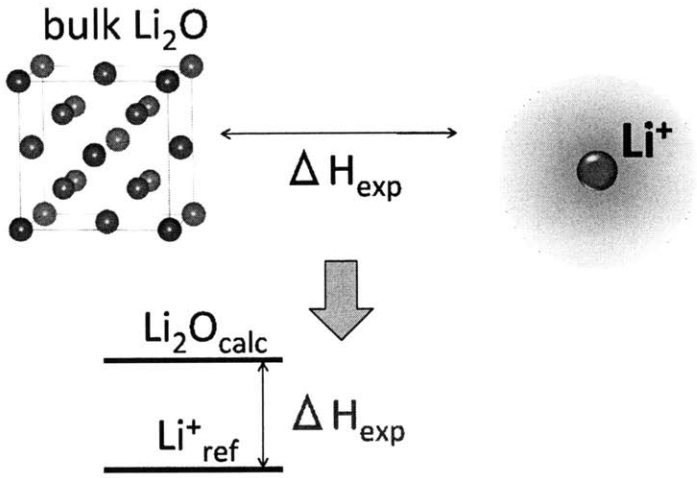

Figure 4-2 Schematic illustration of how "effective" *ab initio* energies for aqueous species such as Li^+ are obtained using an experimental reaction enthalpy.

B) Surface adsorption for important $LiFePO_4$ surfaces

Because of the large scale of the calculations involved, we only study one monolayer adsorption of chemical species on $LiFePO_4$ surfaces, and we do not intend to investigate any particular surface structure patterns formed due to the variation in adsorbate concentrations. We start with the clean surfaces generated in our previous studies of stoichiometric surfaces of $LiFePO_4$. The under-coordinated clean surfaces are further decorated with surface adsorbates according to the following guidelines for each type of surface adsorbate:

1) H

When attempting the possible H sites on clean surfaces, we use bond lengths of 1.0 Å, 1.9 Å, and 2.0 Å, as initial guess for surface O-H, Fe-H, and Li-H bonds, respectively. The bond lengths used above are largely guided by the available bond lengths in H_2O

water molecule (1.01 Å) [43], FeH (1.90 Å) [44] and LiH (2.04 Å) [45] metal hydrides. The total energy of the surface with one monolayer H coverage is reported. Figure 4-3 provides the relaxed surface structure of the proton adsorbed (010) surface. The average bond lengths for O-H, Fe-H, and Li-H bonds in the relaxed surface structure are 0.99 Å, 1.74 Å, and 1.93 Å, respectively.

2) H_2O

All H_2O molecules are attached to under-coordinated surface Fe and Li sites through the bonding between surface cations and O anions in H_2O molecules. After structure relaxations, the angle for H-O-H bond is about 109 degrees, close to the experimental value of 104.6 degrees for single H_2O molecule [43]. Note that absorption of H_2O can also occur in the dissociated form, namely, a combination of hydroxyl radical and proton, as reported in previous studies of hydroxylation reactions for some transition metal oxides.[46] In our case, the result for the (010) surface suggests that absorption of H_2O is energetically more favorable than the dissociated case. Therefore, we only study the adsorption of molecular H_2O in this paper. Figure 4-4 shows the relaxed surface structure of the water molecule capped (010) surface. The Fe-O bond between the surface Fe cation and the oxygen anion in H_2O molecule has an average length of 2.08 Å, shorter than the average length of 2.18 Å for the Fe-O bond in bulk $LiFePO_4$.

3) OH and O

Both hydroxyl groups and external oxygen atoms are attached to the surface under-coordinated Fe and Li sites through the O atoms. For the former adsorbate, the length for

H-O bond after structure relaxations is always close to 1 Å. Figure 4-5 and Figure 4-6 show the relaxed surface structures of the OH and O capped (010) surfaces, respectively. The Fe-O bond between a surface Fe cation and an adsorbed oxygen anion has an average bond length of 1.81 Å and 1.91 Å, respectively for OH and O adsorbates. This is shorter than the value of 2.08 Å for molecular H_2O absorption.

Table 4-2 provides the number of adsorbates used in our simulation slabs for fifteen $LiFePO_4$ surfaces, as well as the area of the surface unit cell. For H_2O adsorption on some surfaces, there are two values provided respectively for number of H_2O molecules on Li stoichiometric and Li-deficient surfaces.

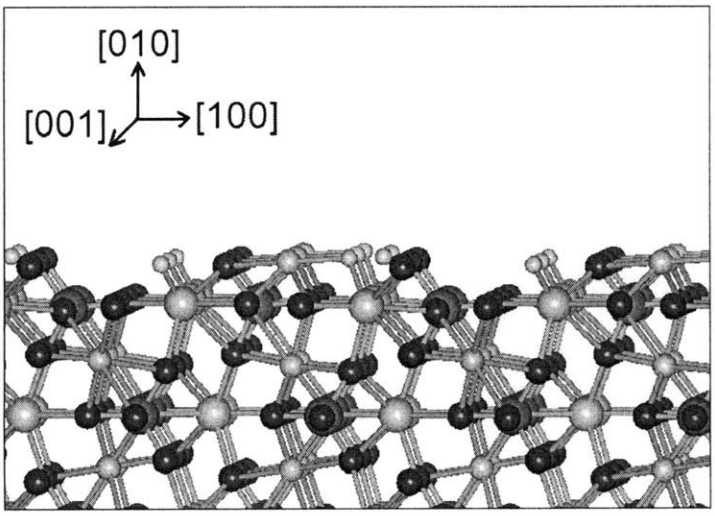

Figure 4-3 Relaxed surface structure of a proton capped (010) surface. Li, Fe, P, and oxygen atoms are shown in green, yellow, purple, and red, respectively. The small pink atoms are surface H adsorbates.

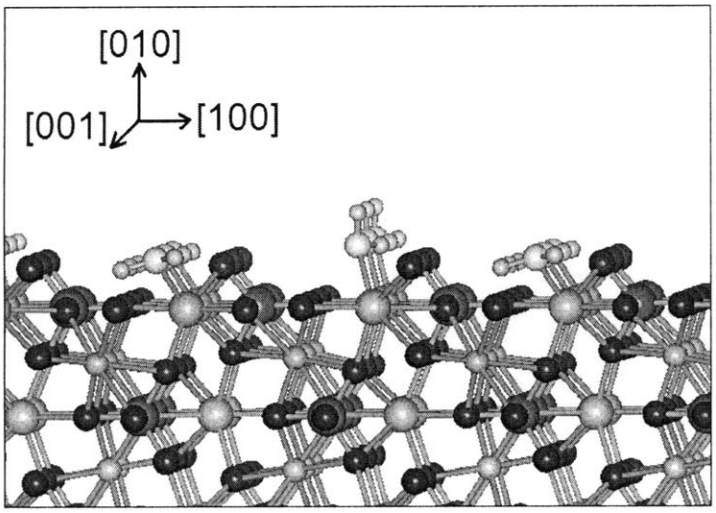

Figure 4-4 Relaxed surface structure of a water capped (010) surface. Colors for Li, Fe, P, O, and surface H atoms are the same as in Figure 4-3. Oxygen atoms in the surface H_2O adsorbate are shown in grey.

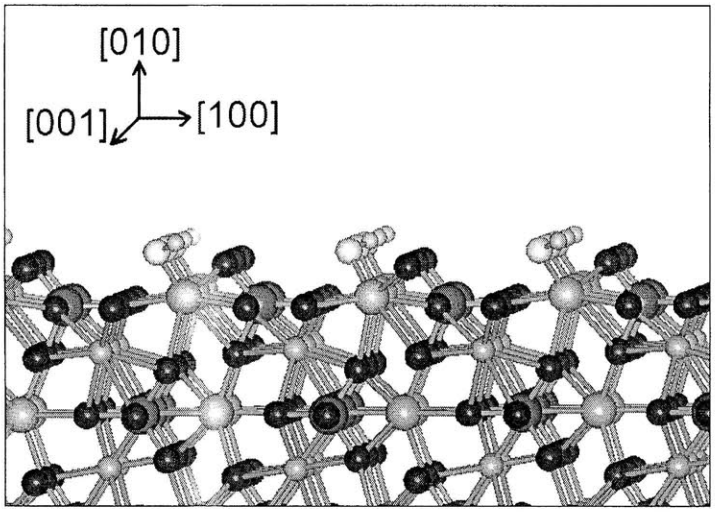

Figure 4-5 Relaxed surface structure of a hydroxyl capped (010) surface. Colors for Li, Fe, P, O, and surface adsorbate are the same as in Figure 4-4.

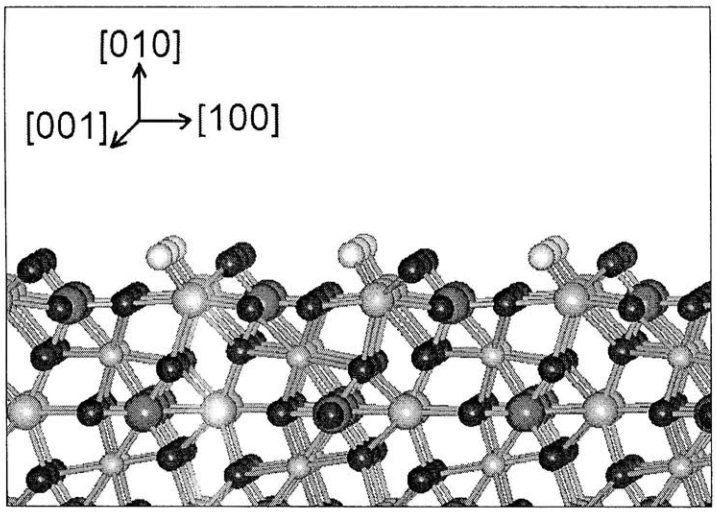

Figure 4-6 Relaxed surface structure of an oxygen capped (010) surface. Colors for Li, Fe, P, O, and surface adsorbate are the same as in Figure 4-4.

Table 4-2 Number of surface adsorbates put on fifteen $LiFePO_4$ simulation slabs and the base area S (in unit of $Å^2$) for each simulation slab

	H	H_2O	OH	O	S
(100)	8	2	2	2	28.77
(010)	6	4/4	4	4	49.63
(001)	8	6	6	8	63.18
(011)	6	8	8	8	80.35
(101)	4	6/4	4	4	69.42
(110)	8	6	6	6	57.37
(111)	8	4/4	4	4	85.35
(021)	12	10	10	10	117.66
(012)	14	8/8	8	8	135.77
(201)	10	10	10	10	85.46
(102)	16	10/8	8	8	129.59
(210)	6	4/4	4	4	75.99
(120)	12	8/8	8	8	103.34
(301)	16	10	10	10	106.97
(401)	12	12	12	14	131.29

4.3 Results for application to $LiFePO_4$

4.3.1 Change of favorable surface adsorbate and surface grand potentials

With increasing oxidation conditions of the solution one expect a change in adsorbates on $LiFePO_4$ surfaces. By evaluating the surface grand potentials as function of oxygen chemical potential, we can find the critical oxidation condition at which the surface adsorption changes. TABLE 4-3 provides such critical oxygen chemical potentials μ_O calculated for fifteen $LiFePO_4$ surfaces. Most surfaces are hydrogenated at very low oxygen chemical potential, and are oxidized to OH and further to O coverage as the oxygen chemical potential increases. The (110) and (201) surfaces skip the hydroxide step and are directly oxidized from H_2O to oxygen covered surfaces. Notice that H_2O coverage is stable over a wide range of oxygen chemical potential. Within the stability region of H_2O surface adsorption, Li from some $LiFePO_4$ surfaces dissolves above certain electric potential. Using equation (10), we can calculate the critical electric potentials for the Li dissolution from bulk $LiFePO_4$ and important surfaces. Six of the fifteen $LiFePO_4$ surfaces have Li dissolution potential lower than the bulk value: (010), (101), (111), (102), (210), and (120), indicating that some surfaces can be delithiated while still keeping the bulk $LiFePO_4$ particle lithiated. Table 4-4 provides the critical Li dissolution electric potentials for the six H_2O-capped surfaces calculated at three levels of Li^+ chemical activity, 0.1, 1, and 3. A high value of Li^+ activity increases the electric potentials at which Li dissolves. This is an indication that concentration of aqueous ions in solution can be used to change the surface chemistry and energetics.

Table 4-5 summarizes the surface grand potentials evaluated for fifteen $LiFePO_4$ surfaces at six levels of oxygen chemical potential. Only surface grand potential for the

most favorable adsorbate coverage is listed. These surface grand potentials are effective surface energies for surfaces in an open environment and can be used to generate the equilibrium particle shape at given oxygen chemical potential. At μ_O of -5.83 eV per O, two surface grand potentials are provided for those surfaces that have surface Li dissolution potential lower than the bulk value. The former (latter) value is the surface grand potential before (after) the surface Li dissolving reaction. One can see from Figure 4-7 that the constant oxygen chemical potential line is downward sloping in the E-*pH* plot and the surface dissolution potential is invariant of *pH*. Above the critical electric potential, the surface grand potential changes because of the surface Li dissolution reaction.

One can also present the change in surface adsorbates as function of the electric potential *E* and *pH*. Figure 4-8 to 4-10 show the change of surface adsorption on four important $LiFePO_4$ surfaces. Figure 4-8 shows the calculated diagram at an electric potential of -1.5 V, representing a reducing aqueous condition. All four surfaces show similar transition behavior in favorable adsorption: surfaces are covered with hydrogen at acidic condition and change to H_2O coverage at higher *pH* value. At this electric potential, the H_2O capped (001) surface can be easily reduced to a proton capped surface at a *pH* value of 11.7, compared to the value of 2.9, 2.9, and 0.4, respectively for the (010), (201), and (001) surface. Figure 4-9 shows the diagram for a more neutral environment with an electric potential of 0 V. The H_2O coverage is favorable over the complete *pH* range for all four surfaces. At a higher electric potential of 1 V, the diagram in Figure 4-10 shows that surfaces are gradually oxidized as the OH and O adsorptions start to dominate. The H_2O covered (010) surface is oxidized into OH coverage at *pH* value of 13.1. As a

comparison, the (201) surface is oxidized directly into an oxygenated surface at *pH* about 7.2, and the hydroxyl coverage for this surface is unstable over all the *pH* range. For (001) surface, the H_2O coverage is stable against the hydroxyl coverage at strong acidic condition, and the oxygenated surface dominates above *pH* 9.7. For the (100) surface, the hydroxyl coverage replace the H_2O one at a low *pH* of 3.5, and is stable over the remaining *pH* range. Figure 4-10 suggests that $LiFePO_4$ facets exhibit very anisotropic behavior against the oxidation by external surface adsorbates. We will discuss more in next section.

Table 4-3 Calculated critical oxygen chemical potential μ_O (in unit of eV per formula O) for the change of favorable adsorbates on fifteen $LiFePO_4$ surfaces.

	$H \rightarrow H_2O$	$H_2O \rightarrow OH$	$OH \rightarrow O$
(100)	-10.16	-4.76	-3.08
(010)	-9.92	-3.62	-2.69
(001)	-8.90	-4.97	-4.05
(011)	-10.22	-3.87	-3.56
(101)	-11.90	-3.90	-1.94
(110)	-8.43	-3.90	
(111)	-8.72	-5.32	-2.05
(021)	-10.18	-4.33	-3.09
(012)	-8.91	-4.59	-2.46
(201)	-9.97	-4.32	
(102)	-8.81	-4.92	-2.33
(210)	-9.83	-4.92	-2.77
(120)	-9.73	-4.47	-2.32
(301)	-9.39	-4.46	-3.54
(401)	-9.86	-4.23	-4.11

Table 4-4 Calculated critical electric potentials for the dissolution of Li into aqueous solution from bulk $LiFePO_4$ and six surfaces that have surface Li potentials lower than the bulk value. Results at three levels of Li^+ activity are provided.

$[Li^+]$	Bulk	(010)	(101)	(111)	(102)	(210)	(120)
0.1	0.60	0.17	0.61	-0.06	0.12	-0.09	-0.02
1.0	0.66	0.23	0.67	0.0	0.18	-0.03	0.04
3.0	0.69	0.26	0.70	0.02	0.21	0.00	0.07

Table 4-5 Surface grand potentials (in unit of J/m^2) evaluated at six levels of oxygen chemical potential (in unit of eV per formula O) for fifteen $LiFePO_4$ surfaces

μ_O	-9.38	-7.38	-5.83	-4.28	-4.18	-4.06
(100)	0.40	0.40	0.40	0.27	0.24	0.21
(010)	0.17	0.17	0.17/0.03	0.03	0.03	0.03
(001)	0.19	0.43	0.43	0.17	0.13	0.09
(011)	0.27	0.27	0.27	0.27	0.27	0.27
(101)	0.28	0.28	0.28/0.28	0.29	0.29	0.29
(110)	0.09	0.62	0.62	0.62	0.62	0.62
(111)	0.37	0.62	0.62/0.50	0.30	0.28	0.26
(021)	0.35	0.35	0.35	0.33	0.30	0.26
(012)	0.25	0.44	0.44	0.38	0.37	0.33
(201)	0.27	0.27	0.27	0.24	0.14	0.03
(102)	0.35	0.63	0.63/0.45	0.29	0.27	0.24
(210)	0.56	0.56	0.56/0.42	0.28	0.26	0.24
(120)	0.40	0.40	0.40/0.21	0.15	0.12	0.08
(301)	0.30	0.30	0.30	0.23	0.20	0.15
(401)	0.35	0.35	0.35	0.35	0.33	0.26

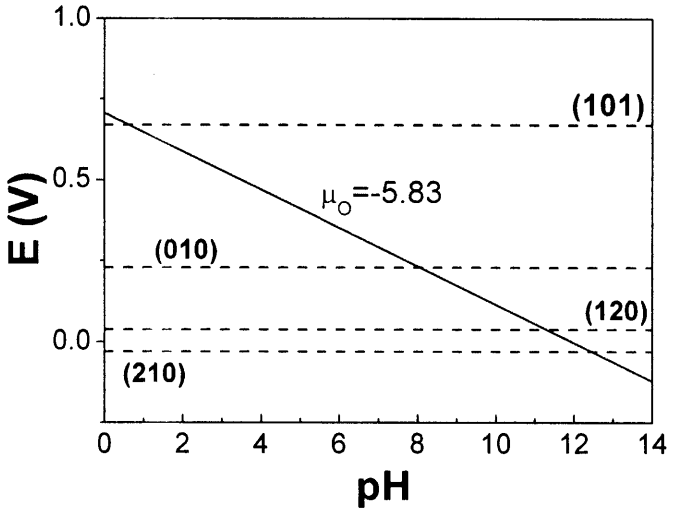

Figure 4-7 Intersection between constant oxygen chemical potential line and Li dissolution lines for $LiFePO_4$ surfaces. The solid line is for oxygen chemical potential of -5.83 eV per formula unit O. From high to low electric potential, the four dash lines refer to the critical electric potential for Li dissolving from surface (101), (010), (120), and (210), respectively.

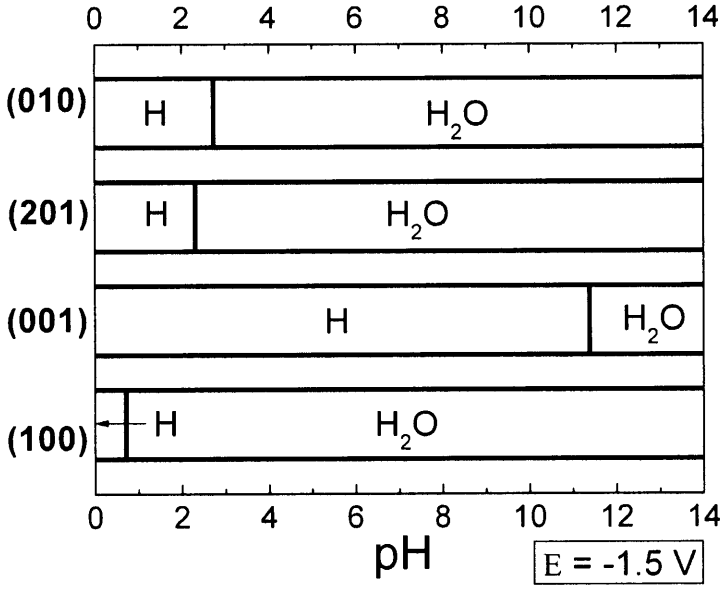

Figure 4-8 Favorable surface adsorption as a function of *pH* at E = -1.5 V for a few important surfaces. The label in each rectangle indicates the favorable surface adsorbate for a given surface at the *pH* range.

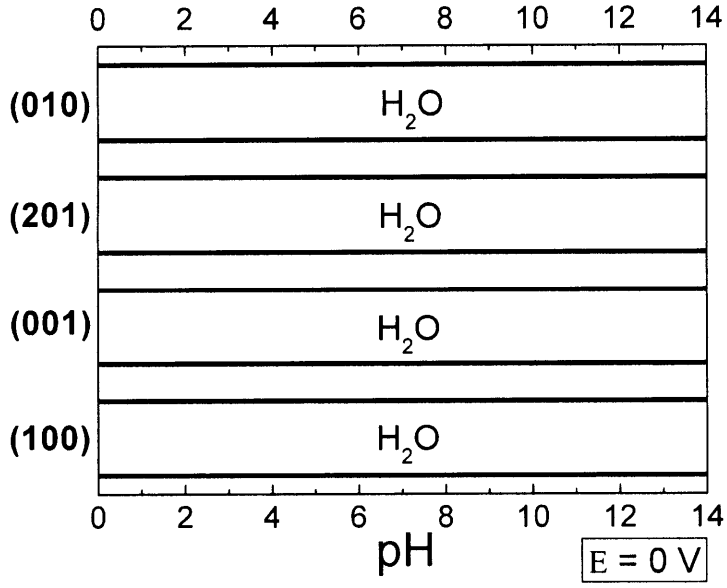

Figure 4-9 Favorable surface adsorption as a function of *pH* at E = 0 V for a few important surfaces.

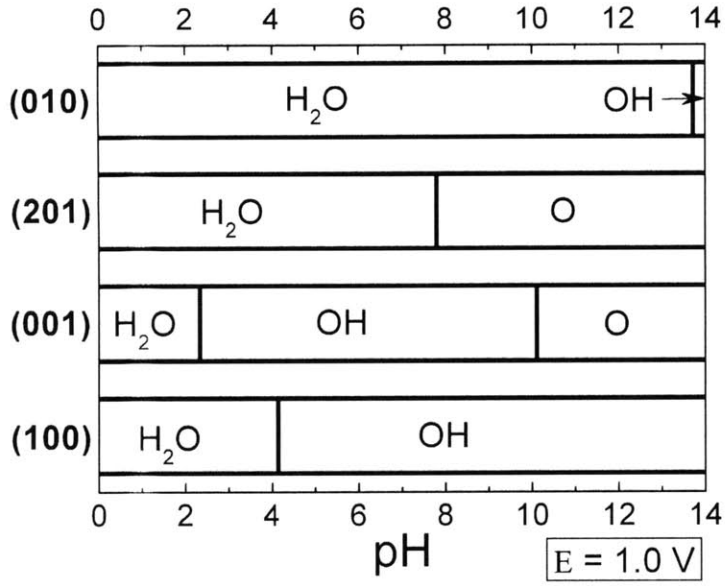

Figure 4-10 Favorable surface adsorption as a function of *pH* at $E = 1.0$ V for a few important surfaces.

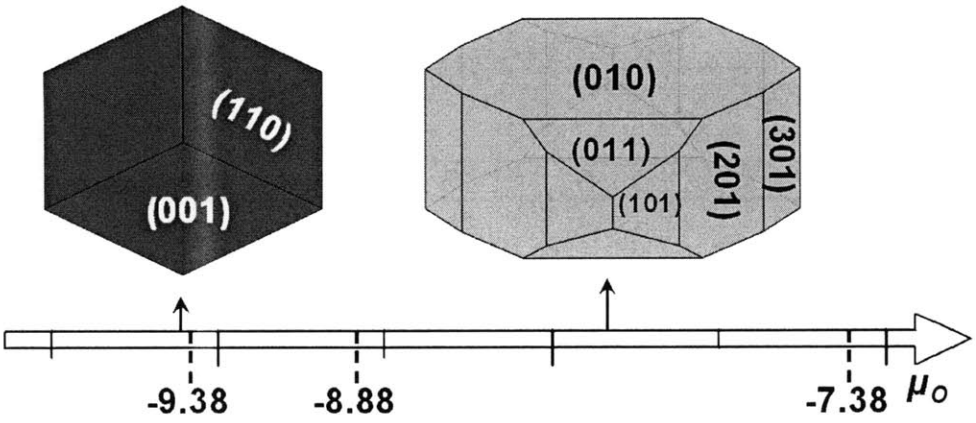

Figure 4-11 Change of Wulff shapes at oxygen chemical potential lower than -7.38 eV per formula unit O. A green facet indicates surface coverage by H and blue indicates H_2O adsorption.

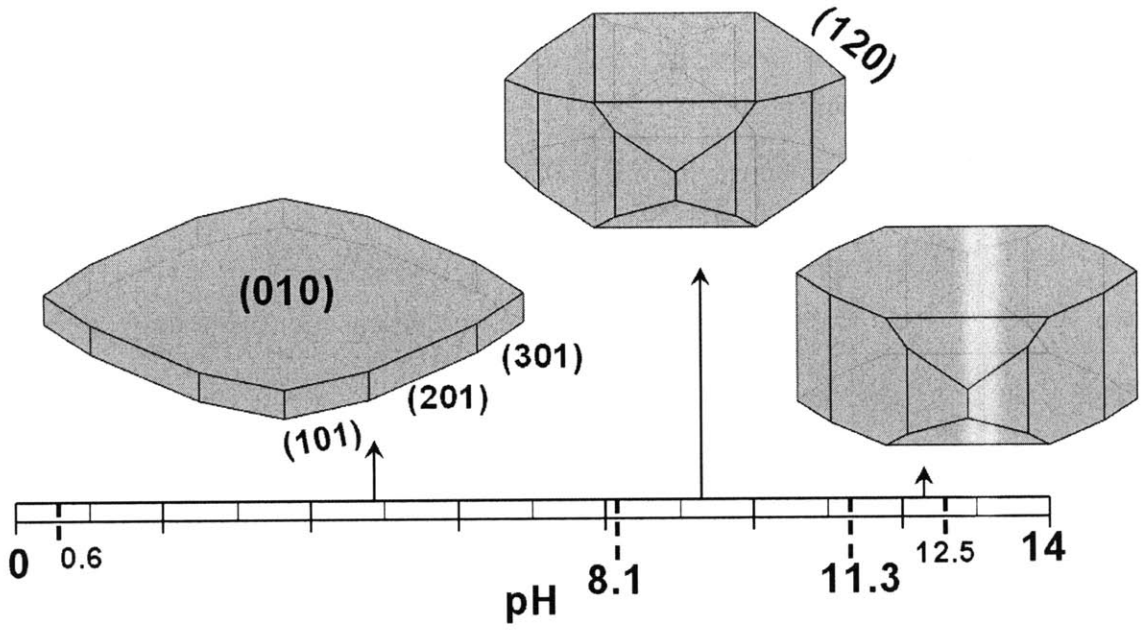

Figure 4-12 Change of Wulff shape as solution *pH* increases while preserving oxygen chemical potential at -5.83 eV per formula unit O. Blue facets refer to surfaces covered by H_2O molecule. Please refer to Figure 4-11 for the Miller indices of some facets if no label is provided.

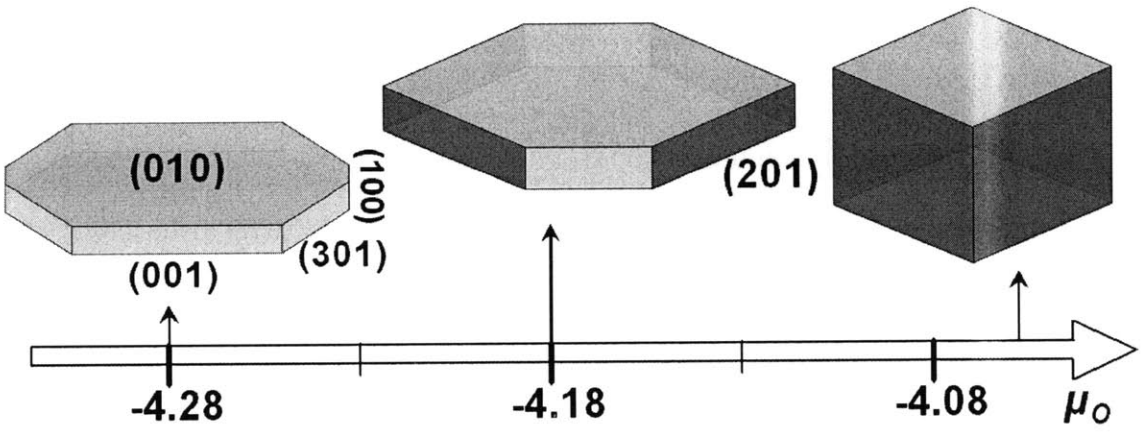

Figure 4-13 Change of Wulff shape at oxygen chemical potential higher than -4.28 eV per formula unit O. Blue facets indicate surfaces covered by H_2O molecule, grey ones are covered by OH, and red ones are covered by O molecule.

4.3.3 Change of Wulff shape

With the surface grand potentials listed in Table 4-5, we can construct the equilibrium particle shape at different oxygen chemical potentials. In Pourbaix diagram, water is electrochemically stable within a region bounded by two lines, one for the water oxidation reaction ($2H_2O \rightarrow 4H^+ + O_2 \uparrow + 4e^-$), and the other for the water reduction reaction ($2H^+ + 2e^- \rightarrow H_2 \uparrow$).[33] The former reaction occurs when the oxygen chemical potential in the solution is above -4.28 eV per O and the latter is thermodynamically favorable for an oxygen chemical potential below -7.24 eV per O. These two critical oxygen chemical potentials segment the Pourbaix diagram into three regions: a reducing, neutral, and oxidizing solution condition, respectively. In this section, we discuss the change of equilibrium particle shape in each region.

Figure 4-11 shows the Wulff shape at oxygen chemical potential lower than -7.38 eV per O. This corresponds to a very reducing aqueous solution condition. At μ_O of -9.38 eV per O, only (001) and (110) surfaces appear in the diamond-like crystal shape (viewed from the [001] direction), and both surfaces are covered by H. Above an oxygen chemical potential of -8.88 eV per formula unit O, the two hydrogenated (001) and (110) surfaces disappear completely and the Wulff shape changes to a thick plate with all the facets capped by molecular H_2O. This equilibrium particle shape is very stable until μ_O of -7.38 eV per formula unit O.

As aqueous solution becomes neutral with the oxygen chemical potential lying between -7.38 and -4.28 eV per formula O, Li ions on some H_2O-capped $LiFePO_4$ surfaces start to dissolve into aqueous solution. The induced changes in surface grand

potentials will modify equilibrium particle shape. Figure 4-7 shows that a constant oxygen chemical potential line (μ_O = -5.83 eV per O) intersects the Li dissolution lines at different *pH* because of variations in surface Li dissolution potentials. The Li^+ activity of one is used in the plot. In Figure 4-12, we present the corresponding change of Wulff shape as a function of *pH* while fixing oxygen chemical potential at -5.83 eV per O. The major change of equilibrium particle shape occurs around the *pH* value of 8.1, below which the Li dissolution from the (010) surface introduces significant decrease of surface grand potential for this facet and gives rise to a thin plate shape. This plate-type crystal has a thickness to width ratio smaller than 1/10 and therefore $LiFePO_4$ particle synthesized at this condition is expected to have improved kinetic performance compared to those particles with a thick plate morphology. Above a *pH* value of 8.1, thickness of the Wulff shape increases and much of the (010) top surface is replaced by the (120) facet. The equilibrium particle shape further changes above the *pH* of 11.3, when the Li dissolution from (120) surface is thermodynamically prohibited. We do not find the dissolution reactions from (101), (102), (111), and (210) surfaces affect the Wulff shape.

Figure 4-13 show the change of Wulff shape at the oxygen chemical potential range of -4.28 to -4.06 eV per formula unit O. The equilibrium morphology changes from a plate to a rectangular block as solution becomes more oxidizing. The increasing exposure of the (201) facet in the Wulff shape is a result of the rapid decrease of surface grand potential along the side (201) surface.

4.4 Discussions and future work

In this work we establish an *ab initio* approach that can be used to study surface adsorption from aqueous solutions and the equilibrium particle morphology as function of the aqueous environment. The approach involves defining reference energies for aqueous species which, when used with *ab initio* energies for the solid state, provide the correct dissolution thermodynamics for a few representative reactions. We demonstrate for $LiFePO_4$ that *ab initio* calculations can be used effectively to investigate the crystal shape dependency on practical parameters, such as electric potential E and solution pH.

We find that at very reducing environment, $LiFePO_4$ facets are covered by hydrogen and a diamond equilibrium shape is favored. When solution condition becomes very oxidizing, the equilibrium particle shape grows in thickness along the [010] direction. Only at relatively neutral aqueous condition, can one expect a plate-type equilibrium particle shape, which is favorable for Li access to the material. Figure 4-12 in this work suggests that the thin plate shape is thermodynamically favored at neutral or slightly acidic condition. This agrees with experimental observations. Dokko et al. found in their hydrothermal synthesis that plate-like $LiFePO_4$ crystals were obtained from weak acidic solutions with $4 < pH < 6.5$ at Li concentration of 2 mol/L.[47] They also found that particles synthesized at pH of 7.4 became thick in the [010] direction, and reported that as the Li concentration in solution increases, plate shape $LiFePO_4$ particles were obtained at more acidic condition. In our model, we can partly explain the dependence of target pH range on Li concentration by the corresponding increase in Li dissolution potential for the (010) surface as the activity of Li^+ increases (refer to the third column in Table 4-4). Notice that in typical hydrothermal synthesis one can not directly control the electric potential E of the solution by the external supply of electric current. However, the

appearances of oxidizing/reducing agents in the aqueous synthesis can modify the oxidizing/reducing ability of the solution and thus change its effective electric potential E.

The strong dependency of Wulff shape on external chemical conditions for $LiFePO_4$ can be related to the anisotropic oxidation/reduction behavior of its surfaces. One can compare the critical oxygen chemical potentials in Table 4-5 for the change of favorable adsorption on different surfaces. At very reducing condition, the (110) and (001) surfaces can be easily reduced to favor H coverage, leading to a diamond shape. On the other hand, the (201) surface has the lowest oxygen chemical potential to be oxidized by external O adsorbate. Thereafter, Wulff shape elongated along the [010] direction is favored as the external environment becomes oxidizing. A surface can also be oxidized via the surface Li dissolution reaction, which leaves some Fe^{3+} in the top surface layer. In other words, the adsorption of chemical species O or OH and the surface Li dissolution are the two competing reactions for a given surface as the solution becomes more oxidizing. Among those important surfaces on the Wulff shape at neutral potential (see Figure 4-12), the (010) surface has a low Li dissolution potential and is oxidized first through the Li dissolution reaction. A further oxidation of this Li-deficient (010) surface by the OH group requires transferring of electrons from the Fe beneath the top surface layer and occurs only at more oxidizing condition than the other surfaces. A similar oxidation process occurs on the (101) surface. In contrast, the (201) surface is oxidized by reacting with O adsorbate because of its high surface Li potential. For the objective of reducing Li diffusion length along the [010] direction, it is critical to oxidize the (010) surface through the surface Li dissolution rather than reacting with oxidizing surface adsorbate.

Another interesting result suggested by our modeling work is the potential inhibitive effect for the oxygen anions at very oxidizing environment. From Figure 13, one can observe that the equilibrium $LiFePO_4$ particle shape becomes elongated along the [010] direction, or equivalently, the crystal growth for side facets is limited. This is not surprising since it is known that the crystal growth rate along one facet direction is positively correlated with the surface energy in that direction.[48, 49] Therefore, as the (201) facet has a decreasing surface grand potential because of the increasing oxygen chemical potential in the environment, the growth rate along the side surface can be considerably slower than the rate in the [010] direction, giving rise to an elongated block particle shape. Interestingly, Fang et al.[50] reported that rectangular block shape $LiMnPO_4$ particles are obtained experimentally because of the potential inhibitive effect from carbonate anion deliberately introduced in the solution. A thick diamond shape of $LiFePO_4$ particles can also be found at Recham et al.'s experimental work.[50] Although it can be rather arbitrary to assign the inhibiting effect from anion adsorbates exclusively to the thermodynamic argument, the Wulff shape predicted in this work does suggest that a platelet shape is no longer favored when oxidizing adsorbates are introduced to the particle surfaces.

For the present case study of $LiFePO_4$ we assume that crystalline $LiFePO_4$ seeds have successfully nucleated under aqueous solution. We have not discussed the possibility that the precipitation of $LiFePO_4$ is not favored against the combination of other solid phases and/or aqueous ions at certain aqueous conditions. For example, previous experimental works found that impurities such as Li_3PO_4, $Fe_5H_2(PO_4)_4*4H_2O$, Fe_2O_3, and $Fe(OH)_2$ may form at very acidic or basic solution conditions.[27, 47] Therefore, within certain *pH* ranges on Figure 4-8 to 4-10, the discussion of favorable surface adsorption can be

meaningless if even bulk $LiFePO_4$ is unstable and dissolve into aqueous ions. A complete discussion of this subject may require the construction of Pourbaix diagram for bulk $LiFePO_4$ with the consideration of all possible binary, ternary, quaternary solid phases, and relevant aqueous ions. Such diagram for bulk $LiFePO_4$ can be combined with current morphology study to accelerate the *ab initio* design of this material under aqueous solution.

Another interesting topic is the search of other novel surfactant using *ab initio* calculations. In current work, only four types of chemical species are considered on $LiFePO_4$ surfaces. We have shown that a careful selection of solution oxidation condition and *pH* can produce thin-plate shape morphology by dissolving Li from H_2O-capped (010) surface. Other surfactants may exhibit more anisotropic adsorption energy when reacting with $LiFePO_4$ surfaces. However, one has to modify the thermodynamic scheme presented in this work to map chemical potential of adsorbate and solution conditions.

4.5 Conclusions

We have established an *ab initio* approach to study surface adsorption and dissolution in aqueous solutions. We demonstrate for $LiFePO_4$ that *ab initio* calculations can be used effectively to investigate the crystal shape dependency on practical solution parameters, such as electric potential *E* and solution *pH*. Due to the one dimensional Li diffusion along the [010] direction of the orthorhombic lattice, maximal exposure of that facet is expected to lead to improved kinetics. Our first-principles work is helpful in finding a synthesis condition that favors the production of platelet shape $LiFePO_4$ with large area of active (010) surface.

References:

[1] I. Lee, F. Delbecq, R. Morales, M. A. Albiter, and F. Zaera, Nat. Mater. **8**, 132 (2009).

[2] N. Tian, Z. Y. Zhou, S. G. Sun, Y. Ding, and Z. L. Wang, Science **316**, 732 (2007).

[3] M. Graetzel, Nature **414**, 338 (2001).

[4] Y. Xiong and Y. Xia, Adv. Mater. **19**, 3385 (2007).

[5] D. V. Bavykin, J. M. Friedrich, and F. C. Walsh, Adv. Mater. **18**, 2807 (2006).

[6] P. Liu, S. H. Lee, C. E. Tracy, Y. Yan, and J. A. Turner, Adv. Mater. **14**, 27 (2001).

[7] X. Peng, Adv. Mater. **15**, 459 (2003).

[8] J. W. Mullin, *Crystallization* (Butterworth-Heinemann, 2001).

[9] G. Medeiros-Ribeiro, A. M. Bratkovski, T. I. Kamins, D. A. A. Ohlberg, and R. S. Williams, Science **279**, 353 (1998).

[10] O. E. Shklyaev, M. J. Beck, M. Asta, M. J. Miksis, and P. W. Voorhees, Phys. Rev. Lett. **94**, 176102 (2005).

[11] N. Moll, M. Scheffler, and E. Pehlke, Phys. Rev. B **58**, 4566 (1998).

[12] I. G. Shebzukhova, L. P. Arefeva, and K. B. Khokonov, The Physics of Metals and Metallography **105**, 338 (2008).

[13] S. Mukherjee, E. Pehlke, and J. Tersoff, Phys. Rev. B **49**, 1919 (1994).

[14] A. S. Barnard, X. M. Lin, and L. A. Curtiss, Journal of Physical Chemistry B **109**, 24465 (2005).

[15] C. M. Lieber and Z. L. Wang, Mater. Res. Bull. **32**, 99 (2007).

[16] A. Marmier and S. C. Parker, Phys. Rev. B **69**, 115409 (2004).

[17] A. S. Barnard and P. Zapol, Phys. Rev. B **70**, 235403 (2004).

[18] A. Soon, L. Wong, B. Delley, and C. Stampfl, Phys. Rev. B **77**, 125423 (2008).

[19] M. Lazzeri, A. Vittadini, and A. Selloni, Phys. Rev. B **63**, 155409 (2001).

[20] G. Wulff, Z. Kristallogr. Mineral. **34**, 449 (1901).

[21] H. G. Yang, C. H. Sun, S. Z. Qiao, J. Zou, G. Liu, S. C. Smith, H. M. Cheng, and G. Q. Lu, Nature **453**, 638 (2008).

[22] S. M. Lee, S. N. Cho, and J. Cheon, Adv. Mater. **15**, 441 (2003).

[23] S. F. Yang, P. Y. Zavalij, and M. S. Whittingham, Electrochem. Commun. **3**, 505 (2001).

[24] S. Franger, F. Le Cras, C. Bourbon, and H. Rouault, Electrochemical and Solid State Letters **5**, A231 (2002).

[25] J. Lee and A. S. Teja, Mater. Lett. **60**, 2105 (2006).

[26] K. Dokko, S. Koizumi, and K. Kanamura, Chemistry Letters **35**, 338 (2006).

[27] C. Delacourt, P. Poizot, S. Levasseur, and C. Masquelier, Electrochemical and Solid State Letters **9**, A352 (2006).

[28] J. J. Chen and M. S. Whittingham, Electrochem. Commun. **8**, 855 (2006).

[29] N. Recham, M. Armand, L. Laffont, and J. M. Tarascon, Electrochemical and Solid State Letters **12**, A39 (2009).

[30] D. Morgan, A. Van der Ven, and G. Ceder, Electrochemical and Solid State Letters **7**, A30 (2004).

[31] M. S. Islam, D. J. Driscoll, C. A. J. Fisher, and P. R. Slater, Chem. Mater. **17**, 5085 (2005).
[32] K. Amine, J. Liu, and I. Belharouak, Electrochem. Commun. **7**, 669 (2005).
[33] M. Pourbaix, *Atlas of Electrochemical Equilibria in Aqueous Solutions* (National Association of Corrosion Engineers, Houston, TX, 1974).
[34] L. Wang, T. Maxisch, and G. Ceder, Phys. Rev. B **73**, 195107 (2006).
[35] P. E. Blochl, Phys. Rev. B **50**, 17953 (1994).
[36] G. Kresse and J. Furthm/uller, Phys. Rev. B **54**, 11169 (1996).
[37] L. Wang, F. Zhou, Y. S. Meng, and G. Ceder, Phys. Rev. B **76**, 165435 (2007).
[38] V. I. Anisimov, J. Zaanen, and O. K. Andersen, Phys. Rev. B **44**, 943 (1991).
[39] V. I. Anisimov, F. Aryasetiawan, and A. I. Liechtenstein, J. Phys.: Condens. Matter **9**, 767 (1997).
[40] A. I. Liechtenstein, V. I. Anisimov, and J. Zaanen, Phys. Rev. B **52**, R5467 (1995).
[41] F. Zhou, M. Cococcioni, C. A. Marianetti, D. Morgan, and G. Ceder, Phys. Rev. B **70**, 235121 (2004).
[42] M. W. Chase, *NIST-JANAF Thermochemical Tables* (American Institute of Physics, Melville, NY, 1998).
[43] A. K. Soper and C. J. Benmore, Phys. Rev. Lett. **101**, 065502 (2008).
[44] V. E. Antonov, K. Cornell, V. K. Fedotov, A. I. Kolesnikov, E. G. Ponyatovsky, V. I. Shiryaev, and H. Wipf, J. Alloys Compd. **264**, 214 (1998).
[45] E. Staritzky and D. I. Walker, Anal. Chem. **28**, 1055 (1956).
[46] A. S. Barnard, P. Zapol, and L. A. Curtiss, Surf. Sci. **582**, 173 (2005).
[47] K. Dokko, S. Koizumi, H. Nakano, and K. Kanamura, J. Mater. Chem. **17**, 4803 (2007).
[48] R. W. Balluffi, S. M. Allen, and W. C. Carter, *Kinetics of Materials* (Wiley-Interscience, 2005).
[49] H. Imai, Y. Oaki, and A. Kotachi, Bull. Chem. Soc. Jpn. **79**, 1834 (2006).
[50] H. S. Fang, L. P. Li, and Y. Yang, Chem. Commun., 1118 (2008).